Theoretical Diagnostics Analysis in Support of KALIF Experiments

J.J. MacFarlane, P. Wang, D.L. Henderson

January 1992

UWFDM-873

FUSION TECHNOLOGY INSTITUTE

UNIVERSITY OF WISCONSIN

MADISON WISCONSIN

Theoretical Diagnostics Analysis in Support of KALIF Experiments

J.J. MacFarlane, P. Wang, D.L. Henderson

Fusion Technology Institute
University of Wisconsin
1500 Engineering Drive
Madison, WI 53706

http://fti.neep.wisc.edu

January 1992

UWFDM-873

Theoretical Diagnostics Analysis in Support of KALIF Experiments

J. J. MacFarlane, P. Wang, D. L. Henderson

Fusion Power Associates
402 Gammon Place
Suite 280
Madison, WI 53719

Fusion Technology Institute
University of Wisconsin-Madison
1500 Johnson Drive
Madison, WI 53706

January 1992

FPA-92-1

UWFDM-873

Contents

1. Introduction

The purpose of this report is to provide a detailed description of work performed during the 1991 calendar year in the areas of spectral diagnostics analysis and radiation-hydrodynamics modeling for light ion beam-heated plasmas. This work has been supported by Kernforschungszentrum Karlsruhe (KfK) as part of a multiyear effort to develop theoretical models and computational tools which can be used to study high energy density plasmas created by KALIF (the Karlsruhe Light Ion Facility). To date, we have developed and tested a collisional-radiative equilibrium (CRE) code in which multilevel atomic rate equations can be solved self-consistently with the radiation field and ion beam properties. In addition, a suite of atomic physics codes have been put together to generate a high quality atomic physics data base which is used by the CRE code. The major features of the CRE and atomic physics codes are listed in Tables 1.1 and 1.2, respectively. We have also recently begun the task of coupling the CRE code with the KfK version of MEDUSA (KATACO).

The statement of work for the 1991 calendar year is listed in Table 1.3. Each of these tasks will be described in detail below. The goals of tasks 1 and 2 were to improve and test the escape probability radiative transfer model in the CRE code. This model, which uses angle- and frequency-averaged escape probability integrals, provides computationally efficient solutions with moderate accuracy. During the past year we have also developed and tested a multiangle, multifrequency radiative transfer model, which has been included in the CRE code. This model provides more accurate solutions, but at a cost of requiring somewhat more computer time. The user now has the option of using either of the two models. The development and testing of the radiative transfer models are described in Section 2.

Table 1.1. Major Features of Collisional-Radiative Equilibrium Code.

- Multilevel, steady-state atomic rate equations are solved self-consistently with the radiation field and ion beam properties.
- Every state of a given ion is coupled to all other states (ground and excited) of that ion, and all states of the next higher ionization stage.
- Emission spectra include contributions from bound-bound (lines), bound-free (recombinations), and free-free transitions (Bremsstrahlung).
- Line shapes include effects of natural, Doppler, and Stark broadening.
- Radiation transport is modeled using either:

  (i) an angle- and frequency-averaged escape probability method, or

  (ii) a multiangle, multifrequency model based on the second-order form of the transfer equation.

Table 1.2. Major Features of Atomic Physics Models.

- Atomic physics data (energies, oscillator strengths, rate coefficients) are computed using a combination of Hartree-Fock, Dirac-Fock, distorted wave, and semiclassical impact parameter models.
- Ion-impact ionization cross-sections are computed using a plane-wave Born approximation model with Hartree-Fock wavefunctions.
- Multiconfiguration Hartree-Fock and Dirac-Fock calculations provide accurate transition energies and oscillator strengths for lines of interest.

Table 1.3. Tasks for 1991

1. Complete work to model effects of temperature and density gradients. Compare with previously published solutions and ONEDANT calculations.
2. Add model to compute escape probability coupling coefficients based on analytic integration over angles in planar geometry. This will likely involve evaluation of escape probability integrals using the third exponential integral.
3. Perform radiative transfer and atomic physics calculations in support of beam-plasma interaction experiments on KALIF. Use temperature and density profiles from hydrodynamics calculations when available.
4. Begin coupling the non-LTE radiative transfer code to MEDUSA. Obtain a copy of MEDUSA and relevant documentation. Improve the computational efficiency of the radiative transport code. Build an interface subroutine for the two codes and begin test calculations.
5. Document results in final report to KfK.

In regards to task 3, we have performed several types of calculations. First, we have investigated the possibility of using K_α line radiation as a temperature diagnostic for aluminum targets. In this study, which has also been supported in part by Sandia National Laboratories, we have compared our calculated spectra with the spectrum obtained in a recent PBFA II experiment (Bailey et al. 1990). This work is described in Section 3.

In Section 4, we present results from a study showing how the ratio of M-shell to L-shell line emission from gold targets can be used to diagnose ion beam energies. Preliminary calculations have also been performed to determine the plasma conditions at which opacity effects begin to reduce the emission from M-shell lines. In Section 5 we describe calculations performed for moderate density plasmas composed of hydrogen,

titanium, and carbon. The purpose of this work is to support diode plasma experiments being performed at KfK by H. Laqua and H. Bluhm.

In Section 6 we describe our initial efforts to couple our CRE non-LTE radiation transport model with MEDUSA. This work has focused on getting a version of MEDUSA to run locally at Wisconsin, improving the computational efficiency (including vectorization) of the CRE code, and laying the groundwork for interfacing the two codes. Finally, we present an overall summary of this year's work in Section 7.

2. Radiative Transfer Model Development

2.1. A Kernel Approach to Radiative Transfer with Zone-to-Zone Coupling

In the escape probability radiative transfer model we have implemented recently (MacFarlane, Wang, and Moses 1990; MacFarlane, Wang, and Henderson 1991), zone-to-zone coupling coefficients are determined using frequency-averaged escape probabilities which are evaluated along a ray defined by a "mean diffusivity angle." Here, we describe a method in which the zone-to-zone coupling coefficients can be obtained in planar geometries from kernel functions.

To obtain the atomic population densities from the atomic rate equations, one needs to determine the photoexcitation (or photoionization) rate at each point in space. For example, the rate equation for a 2-level atom can be written as:

$$\begin{aligned} \frac{dn_u(\vec{r})}{dt} &= n_\ell(\vec{r})[C_{\ell u}(\vec{r}) + B_{\ell u} \int \phi_\nu J_\nu(\vec{r}) d\nu] \\ &- n_u(\vec{r})[C_{u\ell}(\vec{r}) + A_{u\ell} + B_{u\ell} \int \phi_\nu J_\nu(\vec{r}) d\nu] \end{aligned} \tag{2.1}$$

where $A_{u\ell}$ is the Einstein spontaneous emission transition probability, $C_{\ell u}$ is the collisional excitation rate, $C_{u\ell}$ is the collisional deexcitation rate, $B_{\ell u}$ and $B_{u\ell}$ are the Einstein photoexcitation and stimulated emission coefficients, ϕ_ν is the normalized line profile ($\int \phi_\nu d\nu = 1$), and J_ν is the mean intensity of the radiation field.

From the formal solution of the radiative transfer equation in planar geometry, the mean intensity can be written as (Mihalas 1978):

$$J_\nu(\tau_\nu) = \frac{1}{2} \int_0^{T_\nu} S_\nu(t_\nu) E_1(\mid t_\nu - \tau_\nu \mid) \, dt_\nu \, , \tag{2.2}$$

where τ_ν is the optical depth at frequency ν measured along a ray perpendicular to the slab, T_ν is the optical depth for the entire slab, and $E_1(x)$ is the first exponential integral.

The source function for a 2-level atom is:

$$S = \frac{\eta_\nu}{\kappa_\nu} = n_u A_{u\ell}/(n_\ell B_{\ell u} - n_u B_{u\ell}) \, . \tag{2.3}$$

Note that the source function in this case is independent of frequency.

We now make the assumption that the level populations are constant within each zone of our computational grid. Then the total number of photoexcitations per unit time per unit volume in zone a due to photons emitted in zone e is:

$$(n_\ell^a B_{\ell u} - n_u^a B_{u\ell}) \, \bar{J}^{ea} = n_u^a A_{u\ell} \, \frac{\bar{J}^{ea}}{S^a} \, , \tag{2.4}$$

where

$$\bar{J}^{ea} = \frac{1}{\Delta\tau_a} \int_{\tau_a}^{\tau_{a+1}} d\tau \, \frac{1}{2} \int_0^\infty d\nu \phi_\nu^a \int_{\tau_e}^{\tau_{e+1}} S(t_\nu) E_1(\mid t_\nu - \tau_\nu \mid) \, dt_\nu \, . \tag{2.5}$$

The quantities τ_a and τ_{a+1} define the zone boundaries of zone a (the absorbing zone), τ_e and τ_{e+1} define the boundaries of zone e (the emitting zone), and $\Delta\tau_a \equiv \tau_{a+1} - \tau_a$. Here the τ's represent the mean optical depths, which are related to the line center optical depth, τ_c, by $\tau = \tau_c/\phi_0$, with $\phi_0 \equiv$ value of the profile at line center. The first integral – i.e., the integral over the absorbing zone – occurs because we are computing the total number of photoexcitations over the entire volume of zone a (as opposed to simply evaluating the rate at a single point within zone a).

Rearranging Eq. (2.5) we get:

$$\bar{J}^{ea} = \frac{S^e}{2\Delta\tau_a} \int_{-\infty}^{\infty} dx \phi_x^a \phi_x^e \int_{\tau_a}^{\tau_{a+1}} d\tau \int_{\tau_e}^{\tau_{e+1}} dt E_1(\mid t - \tau \mid \phi_x) \, , \tag{2.6}$$

where

$$\begin{aligned} x &\equiv \frac{\nu - \nu_0}{\Delta\nu_D} \, , \\ \phi_x &= \phi_\nu \cdot \Delta\nu_D \, , \end{aligned}$$

$\Delta\nu_D$ is the Doppler width, and $t = t_\nu/\phi_x$. The superscripts e and a again refer to the emitting and absorbing zones. The argument for E_1 is the frequency-dependent optical depth between the point of emission and absorption. To simplify matters, we assume the line profile is spatially uniform, so that $\phi_x^a = \phi_x^e = \phi_x$.

We now make use of the following relations for exponential integrals (see, e.g., Abramowitz and Stegun 1972):

$$\frac{dE_2(y)}{dy} = -E_1(y) \tag{2.7}$$

and

$$\frac{dE_3(y)}{dy} = -E_2(y)\,, \tag{2.8}$$

where $E_2(y)$ and $E_3(y)$ are the second and thrid exponential integrals, respectively.

Then the integrals over optical depth in Eq. (2.6) become:

$$\int_{\tau_a}^{\tau_{a+1}} d\tau \int_{\tau_e}^{\tau_{e+1}} dt E_1(\mid t-\tau \mid \phi_x) = \begin{cases} \frac{1}{\phi_x^2}\{E_3(\mid \tau_e - \tau_{a+1} \mid \phi_x) \\ \quad +E_3(\mid \tau_{e+1} - \tau_a \mid \phi_x) \\ -E_3(\mid \tau_{e+1} - \tau_{a+1} \mid \phi_x) \\ \quad +E_3(\mid \tau_e - \tau_a \mid \phi_x)\} & \text{for } e \neq a \\ \frac{2}{\phi_x^2}\left\{\Delta\tau_a\phi_x + E_3(\Delta\tau_a\phi_x) - \frac{1}{2}\right\} & \text{for } e \neq a\,. \end{cases} \tag{2.9}$$

For the case when $e = a$, substitution of Eq. (2.9) into Eq. (2.6) yields:

$$\bar{J}^{ea} = S^e\left\{1 + \frac{K_3(\Delta\tau_a)}{\Delta\tau_a}\right\} \tag{2.10}$$

where

$$K_3(\tau) \equiv \int_{-\infty}^{\infty} dx \left[E_3(\tau\phi_x) - \frac{1}{2}\right]\,. \tag{2.11}$$

The quantity $K_3(\tau)$ is the third kernel function. It is related to the first and second kernel functions by (Avrett and Hummer 1965)

$$\frac{dK_3(\tau)}{d\tau} = -K_2(\tau) \quad \text{and}$$

$$\frac{dK_2(\tau)}{d\tau} = -2K_1(\tau)\,. \tag{2.12}$$

The first and second kernel functions are defined as

$$\begin{aligned} K_1(\tau) &\equiv \frac{1}{2}\int_{-\infty}^{\infty} dx\phi_x^2 E_1(\tau\phi_x) \quad \text{and} \\ K_2(\tau) &\equiv \int_{-\infty}^{\infty} dx\phi_x E_2(\tau\phi_x)\,. \end{aligned} \tag{2.13}$$

The constant of one-half is used in the integrand of Eq. (2.11) so that $K_3(0) = 0$. Note that the kernel functions depend on the assumed line profile (e.g., Doppler, Lorentz, or Voigt). For the case when $e \neq a$,

$$\begin{aligned} \bar{J}^{ea} &= \frac{S^e}{2\Delta\tau_a}\{K_3(\mid \tau_a - \tau_{e+1} \mid) + K_3(\mid \tau_{a+1} - \tau_e \mid) \\ &- K_3(\mid \tau_{a+1} - \tau_{e+1} \mid) - K_3(\mid \tau_a - \tau_e \mid)\}\,. \end{aligned} \tag{2.14}$$

The zone-to-zone coupling coefficients Q^{ea} of our escape probability model can now be written in terms of kernel functions. The photoexcitation rate is given by:

$$\begin{aligned} (n_\ell^a B_{\ell u} - n_u^a B_{u\ell}) \sum_{e=1}^{N_D} \bar{J}^{ea} &= \frac{n_u^a A_{u\ell}}{S^a} \sum_{e=1}^{N_D} \bar{J}^{ea} \\ &= A_{u\ell} \sum_{e=1}^{N_D} n_u^e Q^{ea}, \end{aligned} \tag{2.15}$$

where N_D is the total number of spatial zones. Thus,

$$Q^{ea} = \frac{1}{S^a n_u^e} \frac{n_u^a}{} \bar{J}^{ea}\,, \tag{2.16}$$

where n_u^a and n_u^e are the number densities of atoms in the upper state in zones a and e, respectively, and the $\bar{J}^{ea}$ are given Eqs. (2.10) and (2.14).

2.2. A Multiangle, Multifrequency Radiative Transfer Method

Inaccuracies in the escape probability model of Apruzese et al. (1980) arise from several points: (1) frequency-averaged escape probabilities are used, which can lead to inaccurate solutions when photons emitted by one transition are absorbed by a different transition; (2) radiation is transported along a single "average" angle; (3) the line profiles are assumed to be uniform from the point a photon is emitted to the point it is absorbed; and (4) the populations (and therefore source functions, opacities, etc.) are assumed to be uniform within each zone. It is therefore of interest to have an accurate model which can be used to benchmark the escape probability model.

During the past year we have developed a multiangle, multifrequency radiative transfer model. The major features of this model are as follows:

1. the second-order differential form of the radiative transfer equation is solved for a grid of angle and frequency points;

2. the model has been developed and tested for both planar and spherical geometries;

3. in converging to a self-consistent solution of the multilevel atomic rate equations and radiation field, one has the option of using the full Λ-operator (complete zone-to-zone coupling) or the diagonal Λ-operator (MacFarlane 1992);

4. matrix elements of the exact Λ-operator are computed using a computationally efficient method recently proposed by Rybicki and Hummer (1991).

The second-order form of the transfer equation can be written as (Mihalas 1978):

$$\mu^2(\partial^2 u_{\mu\nu}/\partial\tau_\nu^2) = u_{\mu\nu} - S_\nu \,, \tag{2.17}$$

where

$$u(z,\mu,\nu) = \frac{1}{2}\left[I(z,\mu,\nu) + I(z,-\mu,\nu)\right]$$

is the average of the specific intensity, I, in the positive and negative μ directions, μ is the cosine of the angle between the direction the photon propagates and the normal to the slab, τ_ν is the optical depth at frequency ν, and S_ν is the source function.

Discretizing Eq. (2.17) onto the optical depth grid $\tau_d\,(d = 1, \cdots, N_D)$ leads to the tridiagonal system of equations (Rybicki and Hummer 1991):

$$-A_d u_{d-1} + B_d u_d - C_d u_{d+1} = S_d\,, \tag{2.18}$$

where second-order differencing provides for $2 \le d \le N_D$:

$$A_d = \frac{2}{\Delta\tau_{d-1}(\Delta\tau_{d-1} + \Delta\tau_d)}\,,$$

$$B_d = 1 + \frac{2}{\Delta\tau_d \Delta\tau_{d-1}}\,,$$

$$C_d = \frac{2}{\Delta\tau_d(\Delta\tau_{d-1} + \Delta\tau_d)}\,,$$

where $\Delta\tau_d = \tau_{d+1} - \tau_d$. The values of A_d, B_d, and C_d for $d = 1$ and N_D depend on boundary conditions.

A key point to note is that this approach is second-order accurate. The solution of u_d depends on the value of the source function at d and $d \pm 1$. By comparison, the escape probability model is numerically less accurate because the source function is assumed to be uniform within each zone.

The photoexcitation and photoionization rates used in the statistical equilibrium equations are obtained by integrating over angle and frequency. Expressions for these

rates are given in MacFarlane (1992). In planar geometry the angle grid is defined by Gaussian integration abcissas and weights (see, e.g., Abramowitz and Stegun 1972). In spherical geometry the transfer equation is solved along rays which are tangent to the radius of each zone of the spatial grid (see Fig. 2.1). This approach is often used to solve spherical radiative transfer problems (Mihalas, Kunasz, and Hummer 1975; Mihalas 1978).

The frequency grid for lines is set up so that there are equally-spaced points in each line core and logarithmically-spaced points in the line wings. Typically the core region has a frequency interval of several Doppler widths. About 5 frequency points are used for the core and 10-15 are used for the wings. These parameters can be adjusted by the user. For bound-free transitions we choose frequencies such that y-values ($y \equiv \nu_1/\nu$; $\nu_1 \equiv$ frequency of absorption edge) are evenly spaced.

2.3. Comparison of Results From Escape Probability, Kernel, and Multiangle, Multifrequency Models

We have performed a series of 2-level atom calculations to assess the reliability of the angle- and frequency-averaged escape probability model in our non-LTE radiative transfer code. The escape probability results are compared with those from the kernal model described in Section 2.1 and the multiangle, multifrequency radiative transfer model. In most cases, results are compared with previously published results. Thus, this series of calculations also serves to test the accuracy of our new multifrequency model. In the examples presented below, we assumed Doppler line profiles unless otherwise stated.

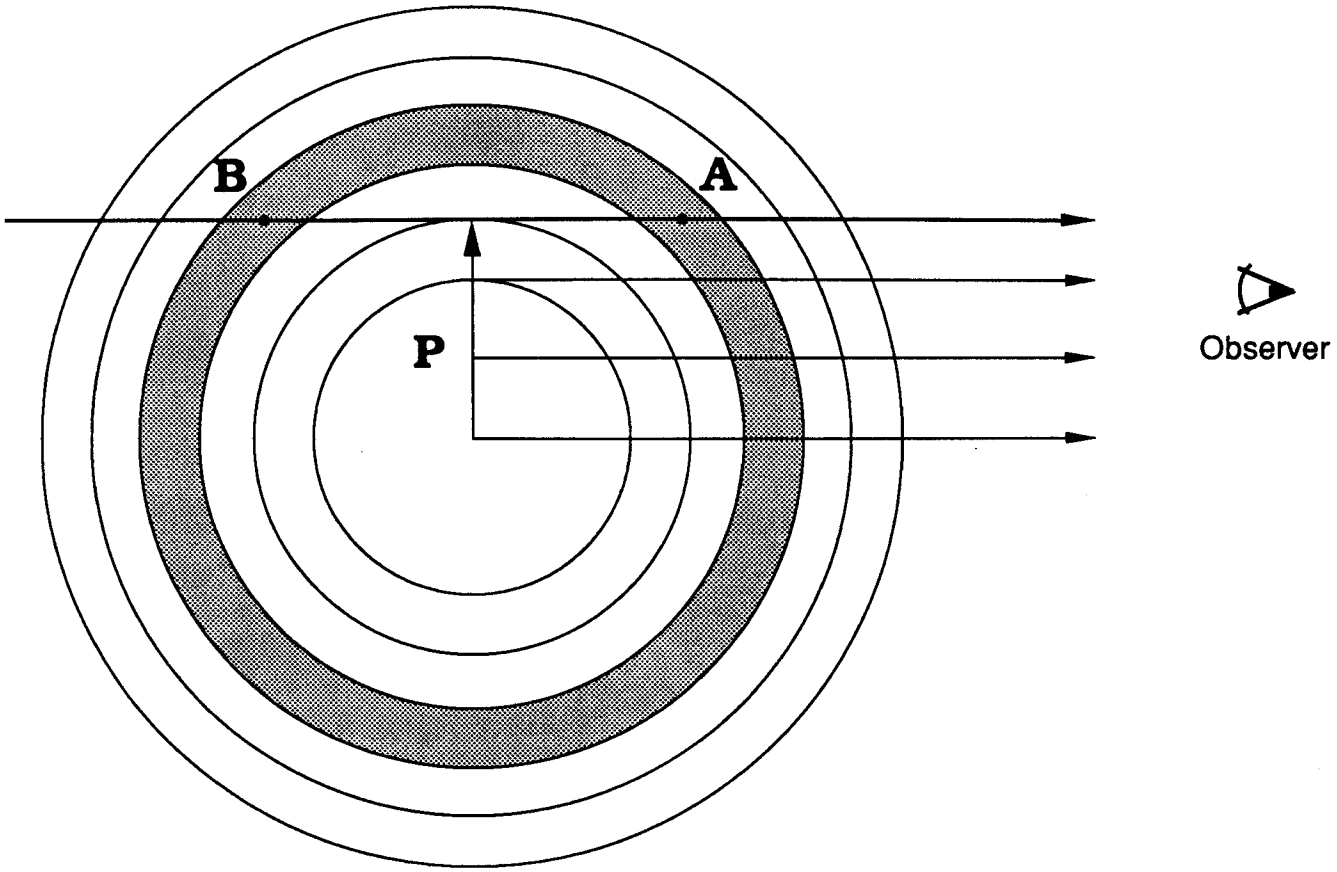

Figure 2.1. Illustration of spatial grid used to solve radiative transfer equation in spherical geometry. The impact parameters are tangent to the spherical shells. The radiation field is determined at points defined by the intersection of the rays and the spherical shells.

2.3.1. Definitions

The figure of merit we have chosen to examine is the spatial distribution of the line source function, which is simply a measure of the population distributions. For a 2-level atom this can be written as:

$$S = B_\nu \left[\exp(h\nu/kT) - 1\right]/\left[(g_u\, n_\ell/g_\ell n_u) - 1\right], \tag{2.19}$$

where B_ν is the Planck function at the transition frequency ν, T is the electron temperature, n_u and n_ℓ are the population densities of the upper and lower levels, g_u and g_ℓ are the statistical weights, and h and k are the Planck and Boltzmann constants. At very large optical depths $S \rightarrow B_\nu$ and a Boltzmann distribution is attained:

$$n_u = n_\ell \,(g_u/g_\ell)\, \exp(-h_\nu/kT)\,. \tag{2.20}$$

The degree of scattering in a plasma – that is, the amount of scattering a photon undergoes before it is destroyed by either the background continuum or a collisional deexcitation – can be expressed in terms of the quenching coefficient:

$$P_Q = C_{u\ell}/\left[C_{u\ell} + A_{u\ell}\,(1 - e^{-\alpha})^{-1}\right], \tag{2.21}$$

where $C_{u\ell}$ is the collisional deexcitation rate, $A_{u\ell}$ is the spontaneous emission rate, and $\alpha = h\nu/kT$. For large values of P_Q (say, $\sim 10^{-1}$ to 1) collisional quenching of line photons is relatively efficient, whereas for small values of $P_Q(\sim 10^{-6}$ to $10^{-4})$ photons can be scattered many times before being destroyed. For present-day ion beam-heated laboratory plasmas with temperatures $\sim 10^0 - 10^1$ eV, P_Q is fairly large ($\sim 10^{-2} - 1$). However, as temperatures in future experiments increase, P_Q decreases and scattering becomes more efficient.

Some of the calculations below are for spherically symmetric plasmas. For calculations which have a hollow core surrounded by a plasma shell, we prescribe the ratio of

the outer radius to the inner radius:

$$R = r_{outer}/r_{inner}\,.$$

Clearly, as $R \to 1$ the plasma geometry becomes similar to that of a planar slab, and as $R \to \infty$ the shell becomes a sphere.

2.3.2. Dependence on Spatial Grid and Angle-Integration Model

Figure 2.2 compares the escape probability integral as a function of line center optical depth (measured perpendicular to the slab surface) computed using the Apruzese model and the kernel models. In the Apruzese model, this integral is given by:

$$I(\tau_c) = \bar{\mu} \int_0^{\tau_c} P_e(t)dt\,,$$

where

$$P_e(t) = \int_0^{\infty} \phi_\nu e^{-t(\phi_\nu/\phi_0)} d\nu$$

and $\bar{\mu}$ is the mean diffusivity angle. Apruzese (1981) found that using $\bar{\mu} = 0.51$ reproduces exact results for 2-level atoms reasonably well. In the kernel method

$$I(\tau_c) = -\pi^{-\frac{1}{2}} K_e(\pi^{\frac{1}{2}}\tau_c)\,.$$

The factor of $\pi^{\frac{1}{2}}$ is simply a normalization constant for Doppler line profiles.

Figure 2.2 shows that the escape probability integrals calculated using the kernel method is somewhat lower than the Apruzese model. In Fig. 2.3 the relative difference between the 2 curves is plotted. For $\tau_c < 10^{-1}$ and $\tau_c > 10^1$, the differences are less than 5%. However, for τ_c near 1 the differences are in the 10-15% range.

Let us now apply these methods to the case of a 2-level atom with a quenching parameter of 10^{-4} and a total line center optical depth of 2.82×10^3 for the slab. Figure 2.4

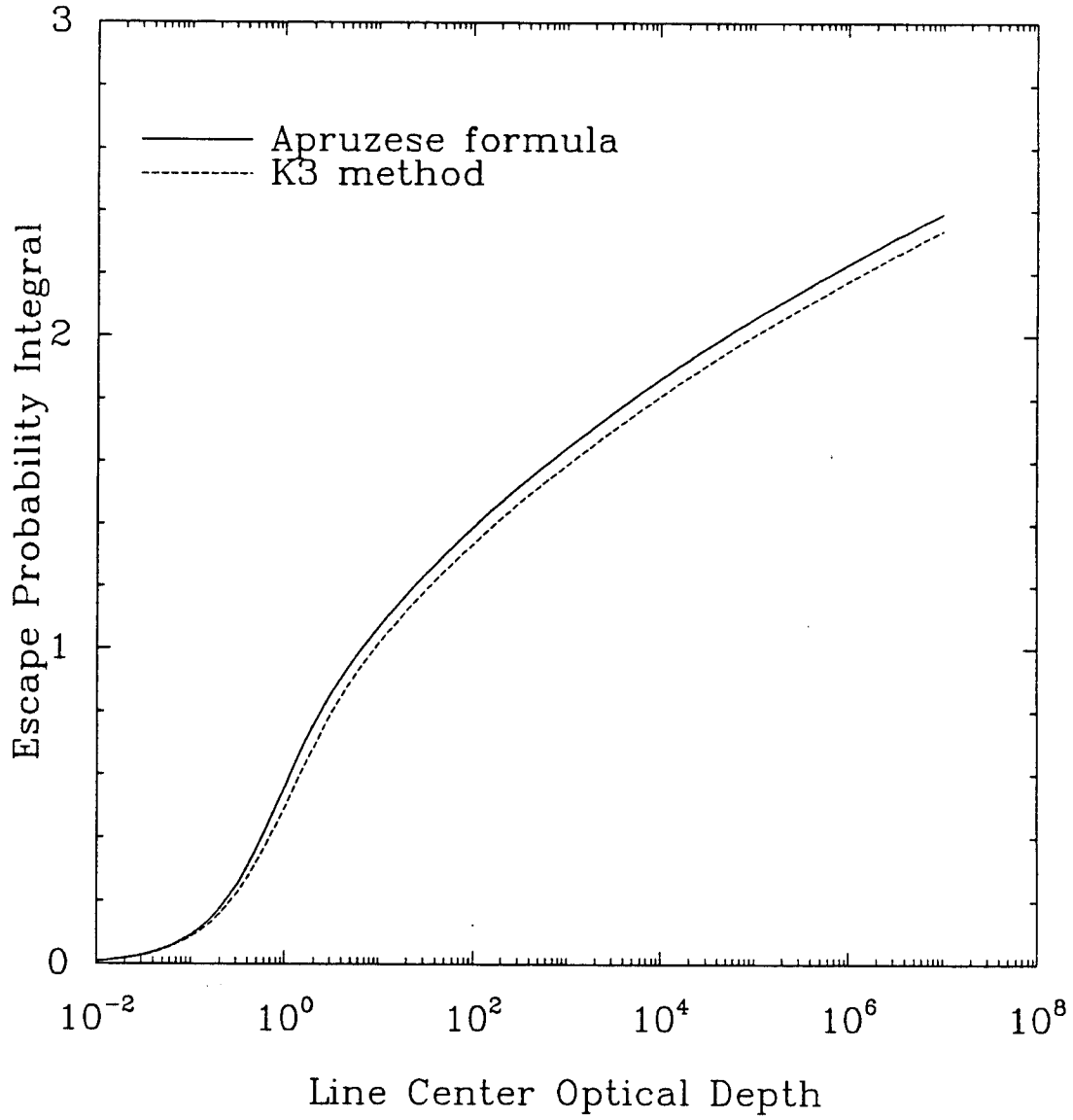

Figure 2.2. Comparison of escape probability integrals calculated using Apruzese model and the kernel method.

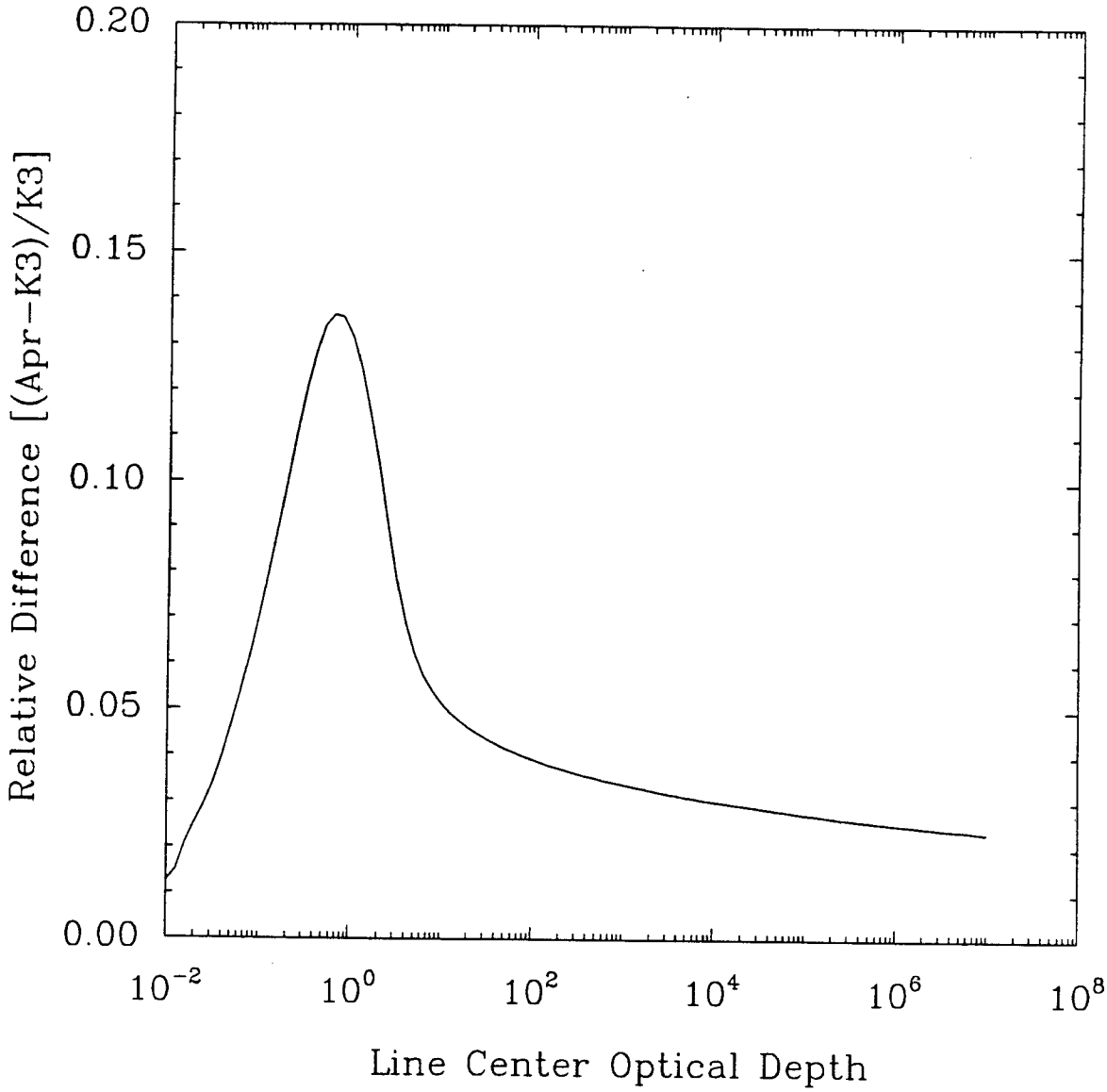

Figure 2.3. Relative difference between escape probability integrals calculated using the Apruzese model and the kernel method.

shows the dependence of the source function (in units of the Planck function) as a function of optical depth. The bottom curve represents the exact solution, which was determined using the differential multifrequency model described above. For both the kernel and Apruzese models we varied the number of mesh points per half-slab from 10 to 75. Note that for a given number of mesh points the 2 models produce very similar results, with differences typically being a few percent. It is interesting to note that the differences between the 2 models are small compared to the absolute error (that is, relative to the "exact" curve).

This of course raises the question: What is most responsible for the absolute errors in this model? It is clear based on the above comparisons that currently the errors introduced by the angle-averaging approximation are small compared to those that arise from using a reasonable number of mesh points. The answer to this question can be found by examining the results computed using the differential radiative transfer model described above. Figure 2.5 shows results computed using this model for the same set of parameters as those in Fig. 2.4. Using only 10 mesh points per half-slab the errors are fairly modest. In fact they are somewhat less than those found in the escape probability model with 75 points per half-slab. Using only 25 points per half-slab in the differential model, we find errors of $\lesssim 3\%$.

Thus, we find the *main* source of error in the escape probability transport model stems from the fact that the level populations are assumed to be constant within each spatial zone. That is, it is the numerical accuracy of the transport solution.

2.3.3. Plasmas with Temperature, Density, and Line Profile Gradients

Next, we study the effects of temperature, density, and line profile gradients in non-LTE laboratory plasmas, and assess the reliability of the escape probability model.

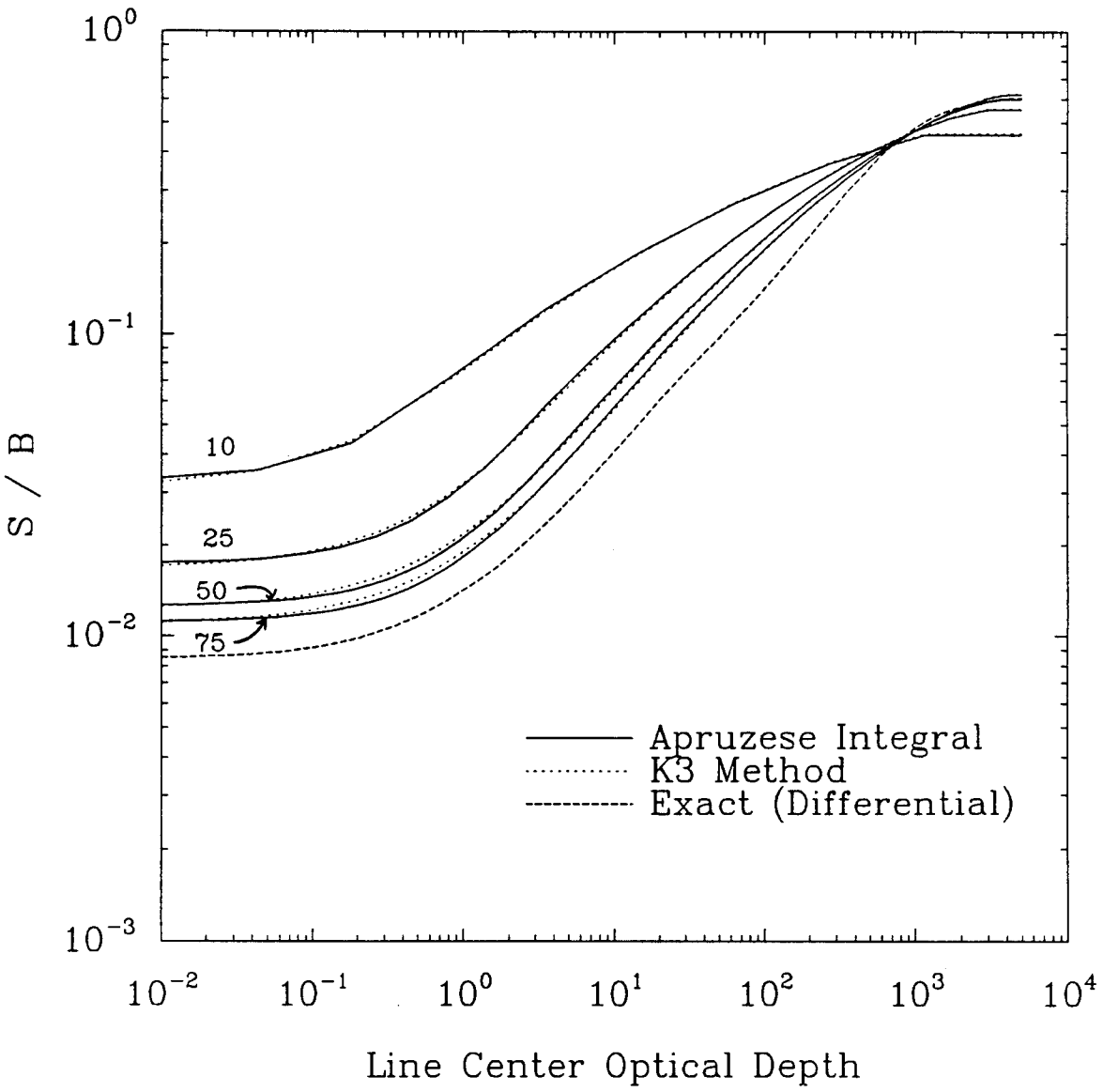

Figure 2.4. Source function distribution for a 2-level atom with $\tau = 2.82 \times 10^3$ and $P_Q = 10^{-4}$. Curve labels indicate the number of mesh points per half-slab. The bottom curve represents the exact solution.

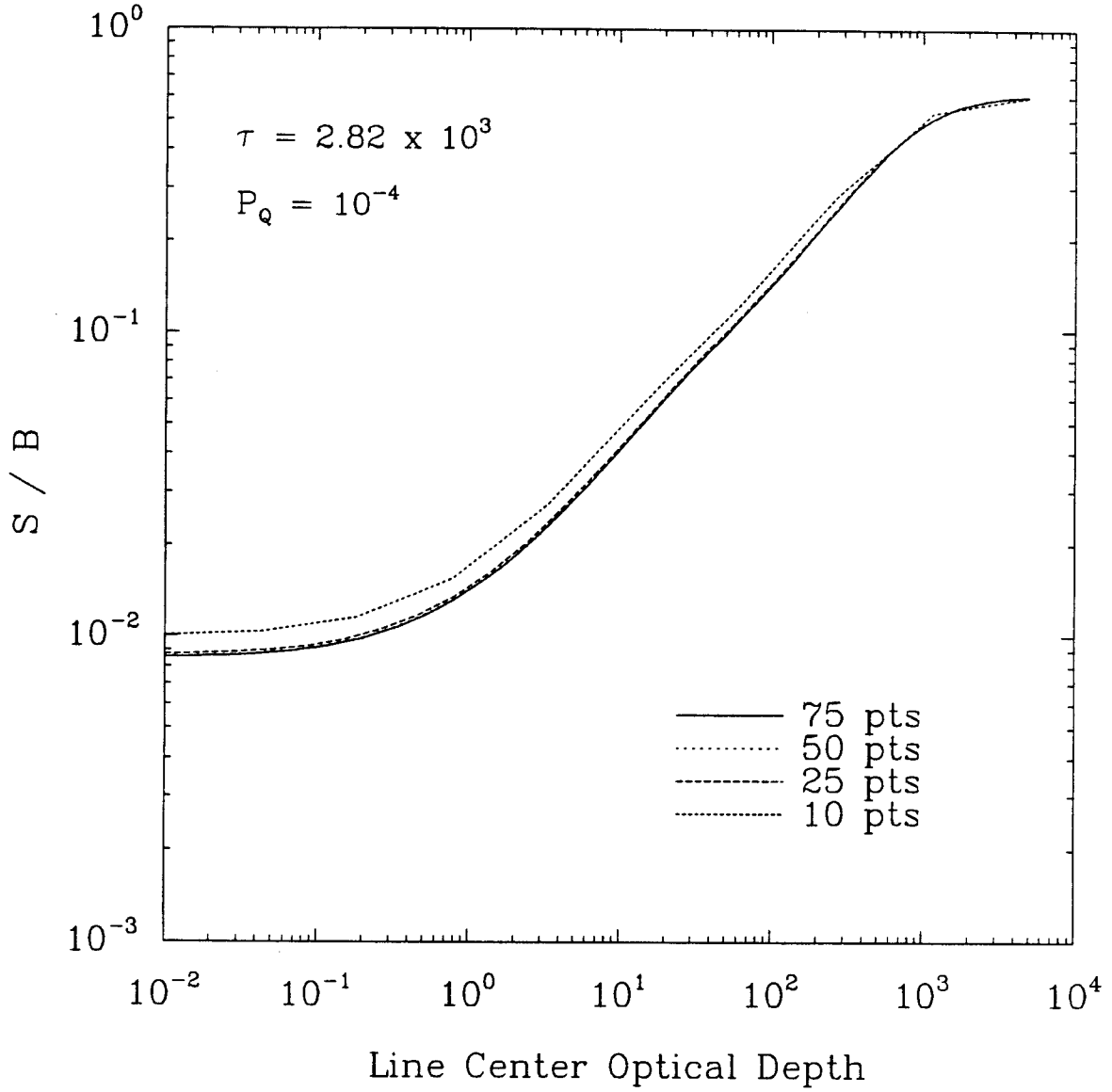

Figure 2.5. Source function distribution computed using the second-order differential transfer method. Curve labels indicate the number of mesh points per half-slab.

A series of calculations with a background continuum has also been performed to study the effects of continuum-induced photoexcitations on line radiation transport. Before examining calculations with gradients, we first examine several cases of homogeneous plasmas to show the differences between models in the absence of gradients.

Escape probability results are presented for two cases — one in which 40 spatial zones were used, the other with 80 zones — because of the dependence on zone size (typically differences were about 10%). For the multifrequency radiation transport model, very little difference was observed between 40 zone and 80 zone cases. The exception to this is Case 4, in which both the temperature and density decrease rapidly near the inner boundary of the plasma shell. In this case multifrequency model results are presented for the 80 zone case. It is of course expected that as one uses a larger and larger number of zones, the solution eventually converges. We find this "asymptotic" solution is reached with fewer zones for the multifrequency transport model than for the escape probability model. The reason for this is that the numerical treatment in the multifrequency method is second order accurate, whereas the escape probability model is less accurate because the source function is assumed to be uniform within each spatial zone.

A few other points are worth briefly mentioning. First, the escape probability and multifrequency radiative transfer models are part of the same non-LTE collisional-radiative equilibrium code. Thus, the comparisons made are with the same spatial computational grid, same plasma conditions, and so forth. Second, the data points for previously published results were obtained by measuring with a ruler. Thus, there may be a small degree of error in placing these points. The exception to this is Case 1, where the published results were explicitly tabulated by Kunasz and Hummer (1974). Third, a Doppler line profile is assumed unless noted otherwise.

CASE 1: Homogeneous Spherical Plasmas

Figure 2.6 shows the source function distributions for the case of a spherical plasma with a spatially uniform temperature, density, and line profile. For the top set of curves, the total line center optical depth (measured radially outward from the center) is $\tau_0 = 10^4/\pi^{1/2} = 5.64 \times 10^3$ and the quenching parameter is $P_Q = 10^{-2}$. For the bottom set of curves $\tau_0 = 5.64 \times 10^2$ and $P_Q = 10^{-4}$.

The results from the escape probability model are represented by two sets of dashed curves: one from calculations using 40 zones (short dashes), the other from calculations using 80 zones (long dashes). The multifrequency results are represented by the solid curve, while the solid boxes represent the previously published results. Note that the results from the multifrequency model are in good agreement with the published results. The errors in the escape probability model range up to about 10% for the 80 zone case and about 20% for the 40 zone case.

CASE 2: Homogeneous Spherical Plasma Shells

In the second case, we examine the source function distributions for spherical plasma shells with two extremes in curvature: $R = 1$ and $R = 300$. Results are shown in Fig. 2.7. In each case, $\tau_0 = 5.64 \times 10^2$ and $P_Q = 10^{-4}$. The conclusions are very similar to those of Case 1. The multifrequency results agree well with the published results, while errors of $\sim$10% to 20% are seen for the escape probability model.

CASE 3: Spherical Plasma Shells with Density Gradients

Next, we consider a hollow plasma shell in which the density varies as r^{-2}. The temperature and line profile are assumed to be spatially uniform. Again, we consider the case in which $P_Q = 10^{-4}$ and $\tau_0 = 5.64 \times 10^2$. Conditions were selected such that the

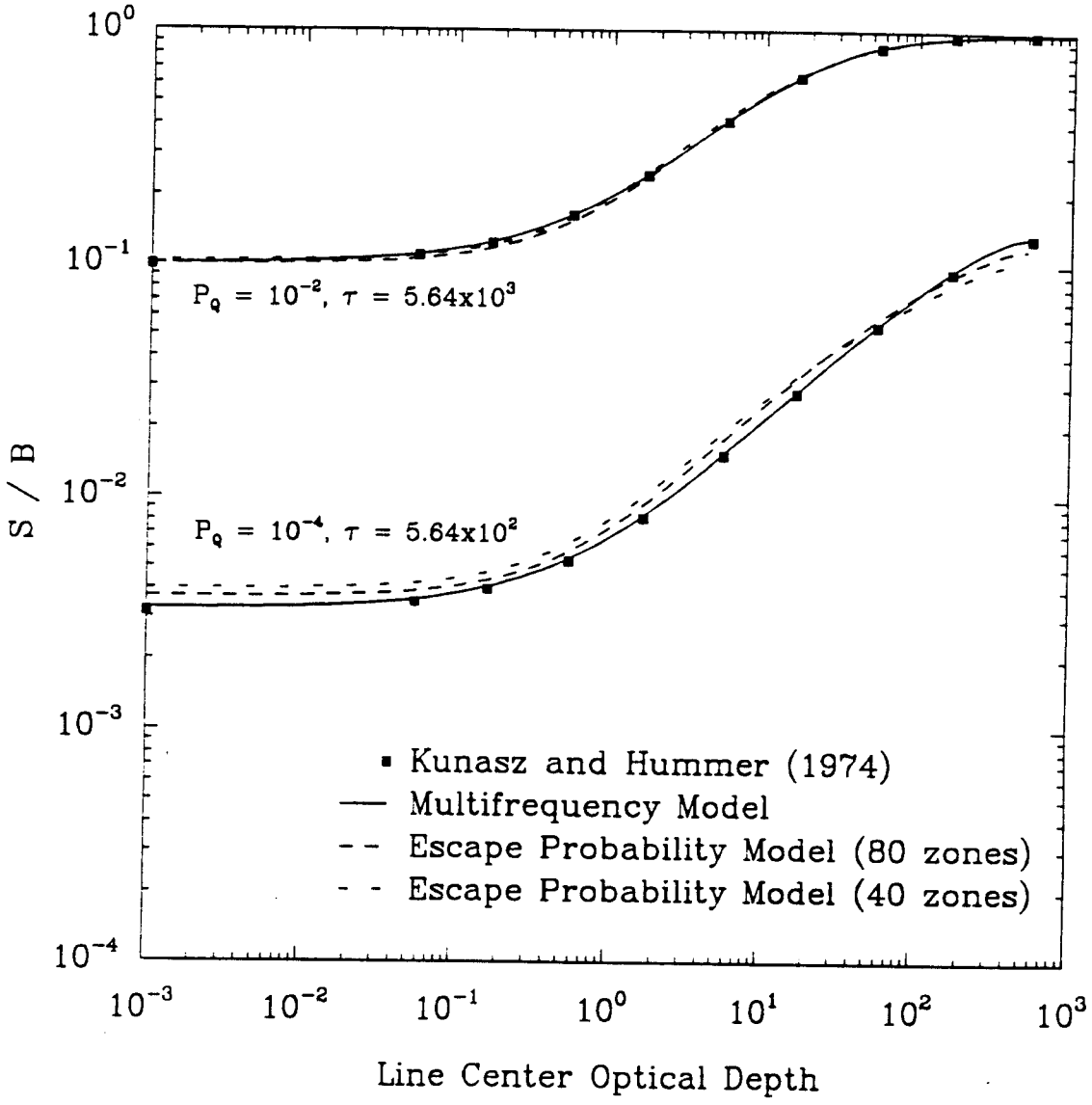

Figure 2.6. Two-level atom source function distribution for a homogeneous spherical plasma.

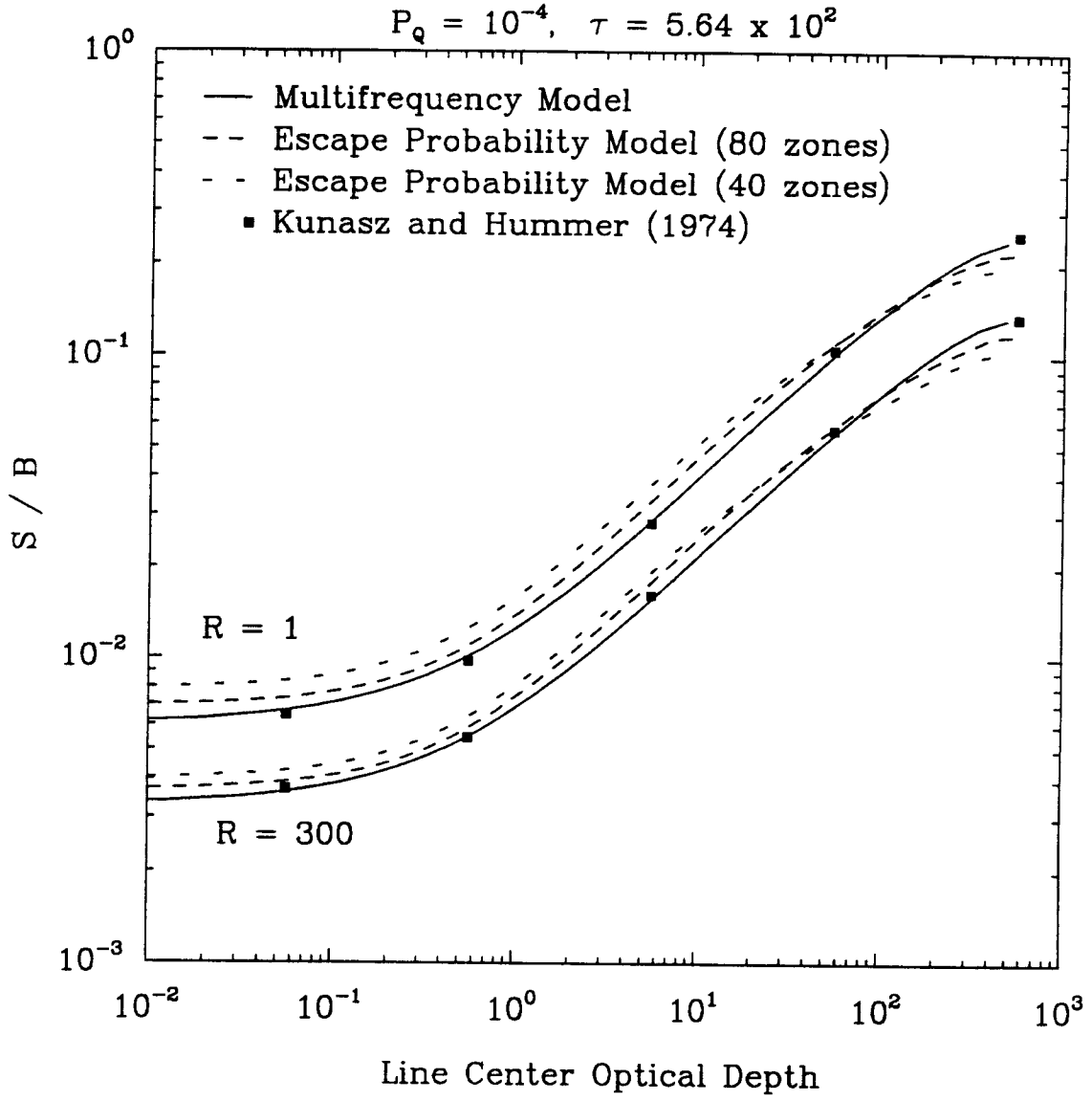

Figure 2.7. Two-level atom source function distribution for homogeneous spherical plasma shells.

upper level populations are small relative to the lower level populations. Thus, both the density and absorption coefficient decreased as $1/r^2$.

Results for this case are presented in Fig. 2.8. Again we see that the multifrequency results agree well with published results, while the escape probability results differ by up to about 10% for the 80 zone case and about 25% for the 40 zone case. Note that the r^{-2} density gradient results in a substantially lower value for the source function (and therefore a lower population for the upper level) near the surface. Without a density gradient (see Fig. 2.7, $R = 300$), $S(\text{surface}) = 3.2 \times 10^{-3}$, whereas for the gradient case $S(\text{surface})$ is a little less than 3×10^{-4}. These results show the escape probability model is reasonably accurate in tracking the effects of density gradients.

CASE 4: Spherical Shells with Temperature and Density Gradients

Figure 2.9 shows results from a case in which the plasma contains both temperature and density gradients. However, *the line widths for the Doppler profiles are held constant*. As in the previous case, the density and absorption coefficient are assumed to decrease as $1/r^2$. The temperature gradient is set up by the following relation with the Planck function:

$$B_\nu \equiv B_0[\exp(h\nu/kT) - 1]^{-1} = (R_{inner}/r)^2 \,,$$

where B_0 is a constant defined by the radius and temperature of the first zone.

Note that the value of the source function near the surface is several orders of magnitude lower than that of Cases 2 and 3. Nevertheless, the escape probability model still provides reasonably accurate values throughout the plasma. We also see again that the multifrequency model solution agrees well with the previously published result, although there is a small discrepancy of a few percent near the surface.

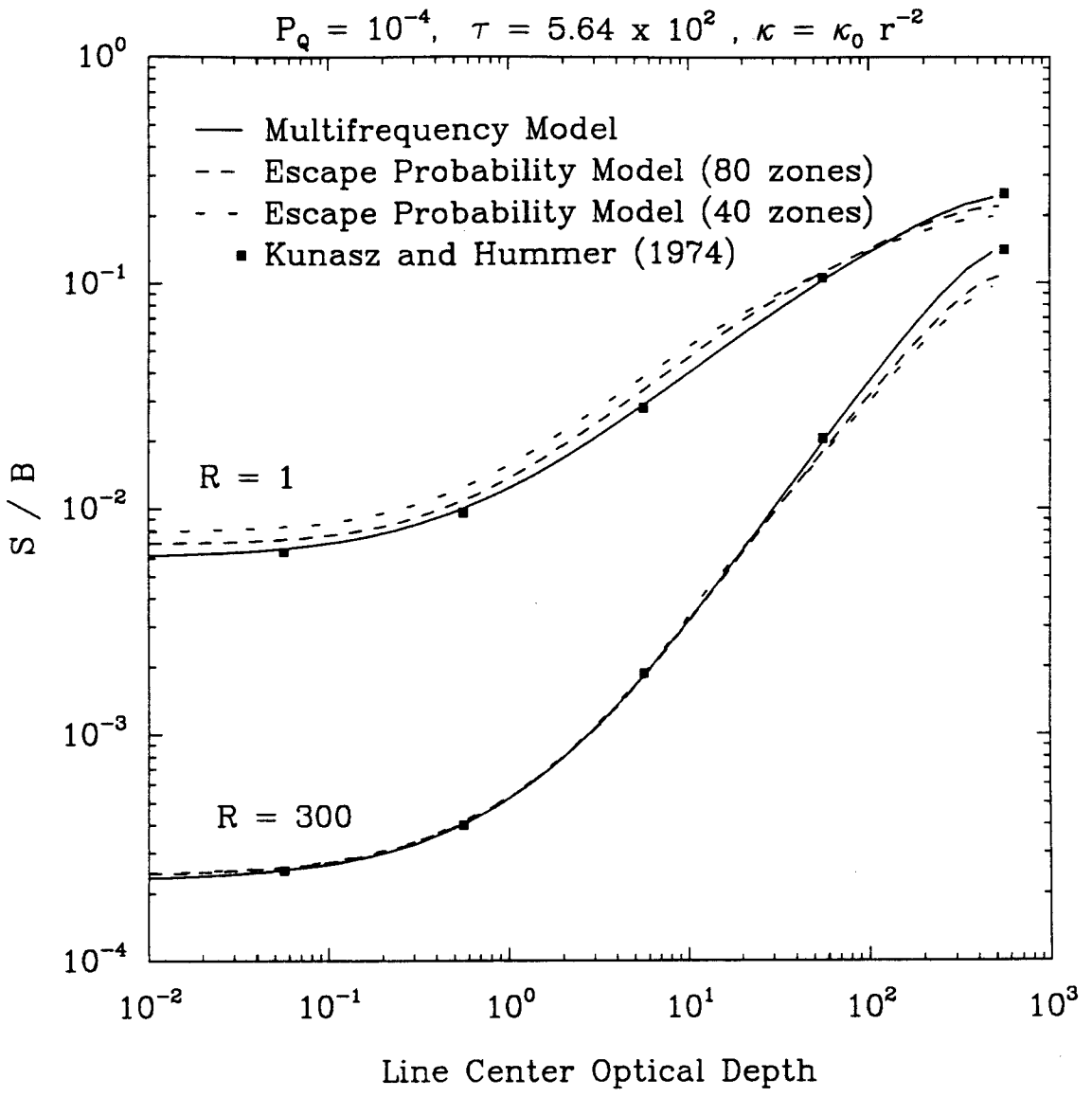

Figure 2.8. Source function distribution for spherical plasma shells with r^{-2} density gradients.

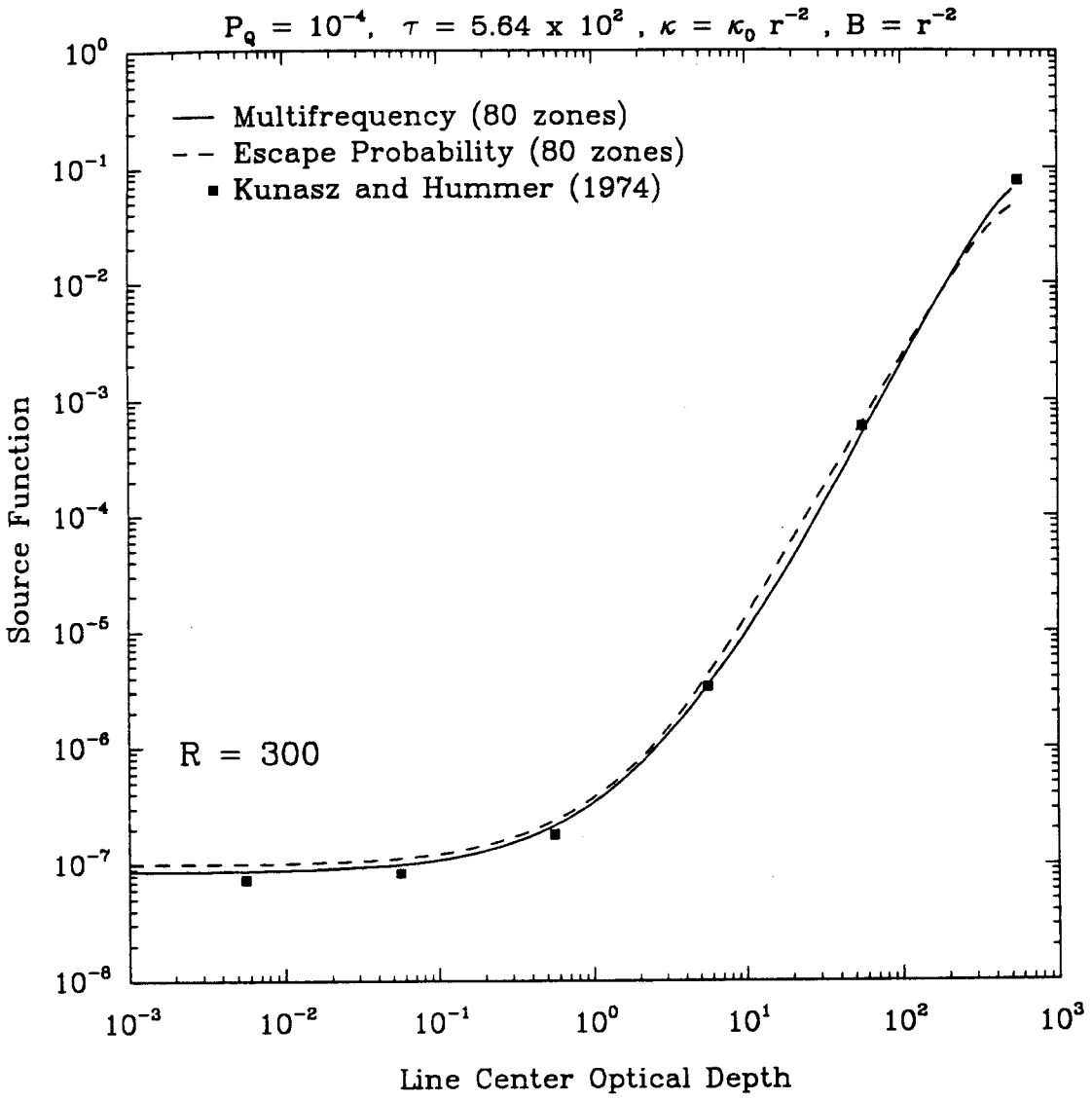

Figure 2.9. Source function distribution for spherical plasma shells with temperature and density gradients.

CASE 5: Planar Plasmas with a Background Continuum

We next consider the case of line transport with a background continuum. In this case the continuum opacity, χ_C, is related to the line opacity, χ_L, by:

$$\chi_C = \beta \chi_L \,,$$

where β is a constant. There are no temperature, density, or line profile gradients in these calculations. The plasmas are planar slabs.

Results are shown in Figs. 2.10 and 2.11. In each case a Voigt line profile with a broadening parameter of $\alpha = 0.01$ is assumed. The plasma is "semi-infinite;" that is, the slab optical depth is infinite. Figure 2.10 shows results for calculations with a quenching parameter of $P_Q = 10^{-6}$. For these conditions the escape probability and multifrequency models could be compared with published results. Figure 2.11 shows results for calculations with a quenching parameter of $P_Q = 10^{-2}$, a value more representative of ion beam-heated laboratory plasmas, but for which no published solutions are available.

In each figure there are several curves. First there are two calculations in with there is no background continuum ($\beta = 0$). These are shown so that the effects of adding a background continuum could be seen. Comparing these curves (the solid and dashed lines without symbols), we see differences between the escape probability and multifrequency results of less than 10% in Fig. 2.11, but about 50% in Fig. 2.10.

When a background continuum is included in the multifrequency transport calculations (solid curves with symbols), we see that the source function increases by an order of magnitude for the case with $\beta = 10^{-6}$ and $P_Q = 10^{-6}$ (open squares; Fig. 2.10), by almost a factor of 2 for the case with $\beta = 10^{-2}$ and $P_Q = 10^{-2}$ (open squares; Fig. 2.11), and by about 20% for the case with $\beta = 10^{-3}$ and $P_Q = 10^{-2}$ (open triangles; Fig. 2.11).

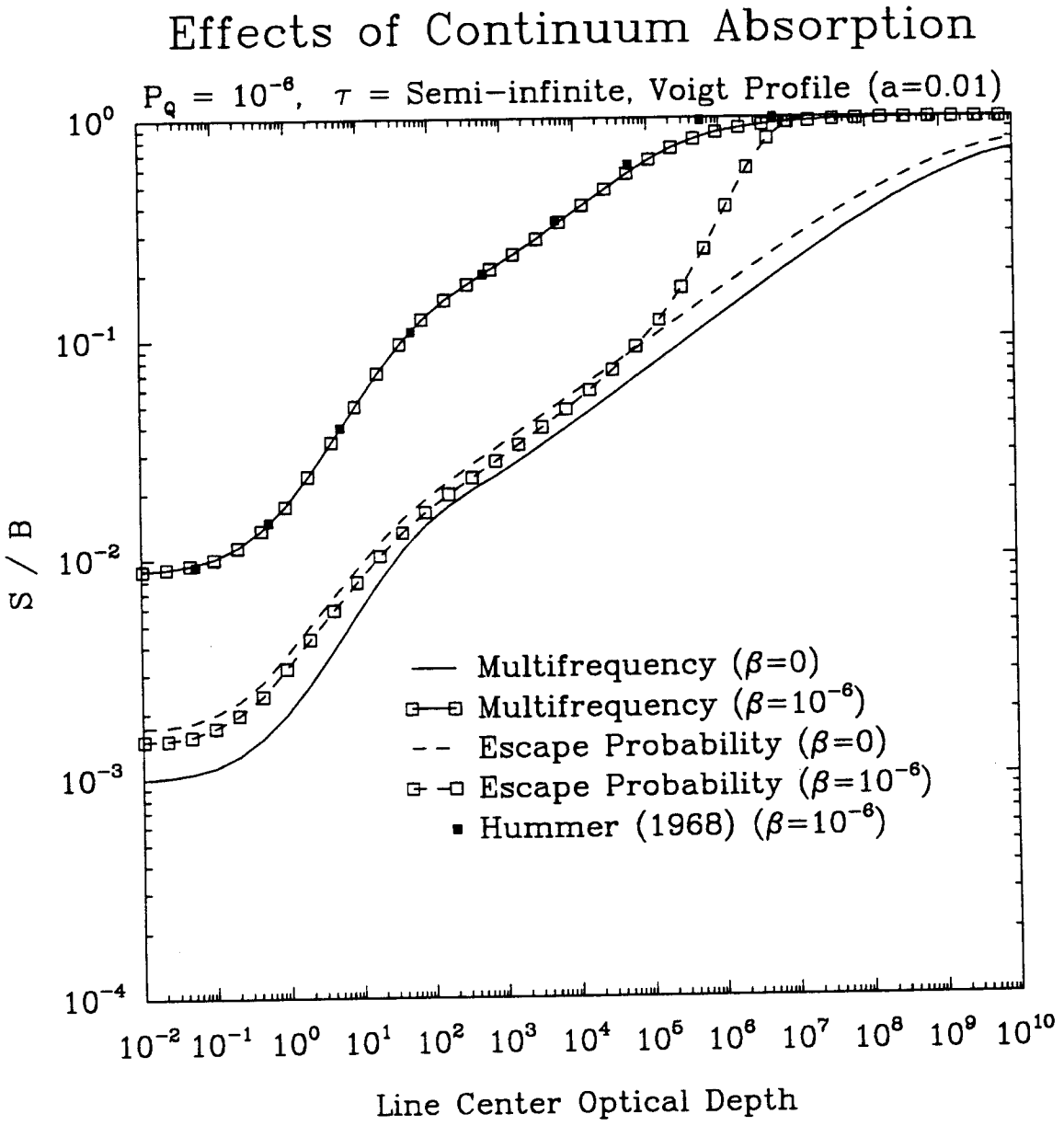

Figure 2.10. Two-level atom source function distribution for planar plasmas with a background continuum of $\chi_C/\chi_L = 10^{-6}$.

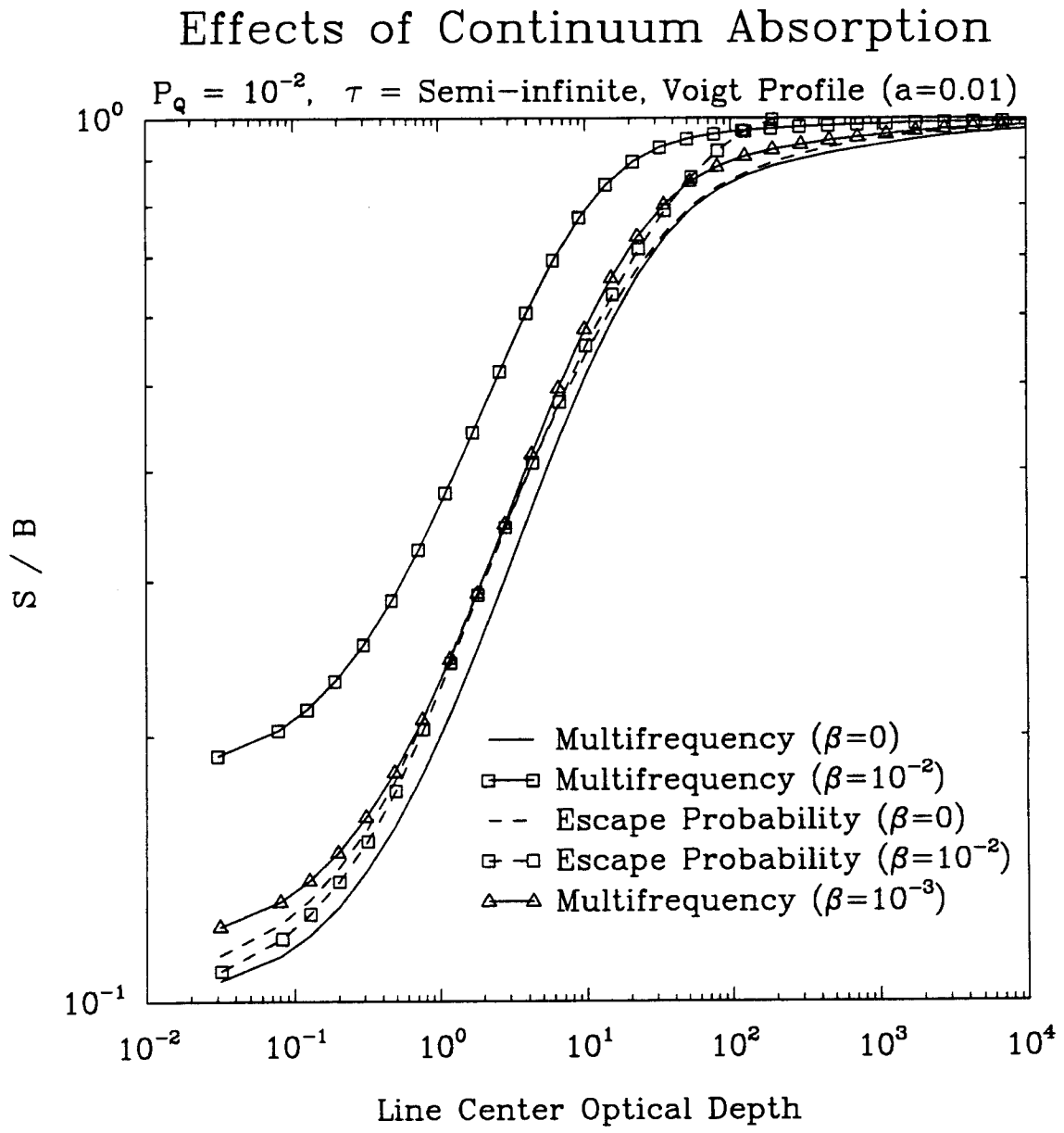

Figure 2.11. Two-level atom source function distribution for planar plasmas with a background continuum of $\chi_C/\chi_L = 10^{-2}$.

Also note that the multifrequency calculations are in good agreement with the published results of Hummer (1968) (solid boxes in Fig. 2.10).

The reason for the enhancement in the upper level populations when a background continuum is included is *not* continuum *absorption*. Rather, it is caused by photoexcitations induced by continuum radiation *emission*. The escape probability model does not provide accurate solutions to this class of problems (compare the dashed and solid curves with the open boxes). This is because the escape probability model attempts to account for absorption of line radiation by the continuum, but does NOT account for photoexcitations caused by continuum radiation emission. Because of this, the continuum acts to reduce the source function (relative to the $\beta = 0$ calculations; dashed lines without symbols) at low optical depths, while increasing the source function at large optical depths (where τ_c exceeds unity).

CASE 6: Planar Plasmas with Line Profile Gradients

We next consider the case of plasmas with spatial gradients for the line profile, but *without* gradients for the temperature and density. This is of course a physically inconsistent scenario because the line profile is influenced by the plasma conditions. However, this test case was chosen because of the availability of published calculations. It also allows one to more easily examine isolated physical effects.

A series of calculations was performed for a planar semi-infinite slab with the following parameters: $P_Q = 10^{-4}$, $\beta^* = 10^{-6}$ ($^*\Rightarrow \chi_C/\chi_L$ is based on the *line center* opacity; this definition differs by a factor of $\pi^{1/2}$ from that used in Case 5), and a Voigt parameter $a = 10^{-3}$. Results are shown in Fig. 2.12. The gradient in the Voigt line profile was set up using the following expressions for the Doppler width:

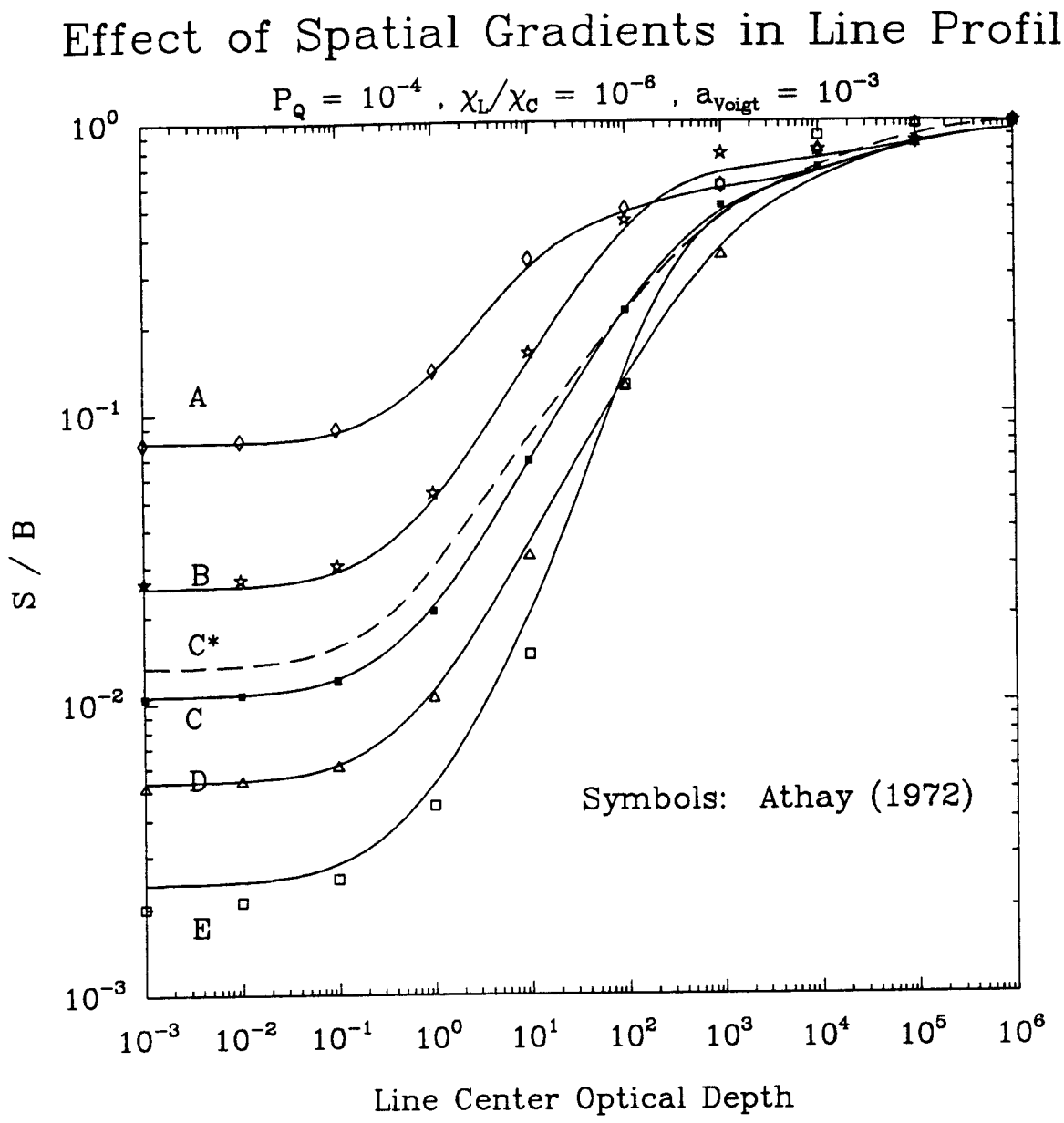

Figure 2.12. Source function distribution for planar plasmas with line profile gradients.

$$\Delta\nu_D = \Delta\nu_{D,surf}\,[1 + 2\exp(-(\gamma\beta^*\tau_0)^{1/2})] \quad \text{for curves A and B,}$$

$$\Delta\nu_D = \Delta\nu_{D,surf} \quad \text{for curve C, and}$$

$$\Delta\nu_D = \Delta\nu_{D,surf}\,[1 + 2\exp(-(\gamma\beta^*\tau_0)^{1/2})] \quad \text{for curves D and E,}$$

where $\Delta\nu_{D,surf}$ is the Doppler width at the surface, τ_0 is the line center optical depth, and γ is a constant. For curves B and D $\gamma = 10^3$, while for curves A and E $\gamma = 10^5$. Note that for all cases except case C the Doppler width changes by a factor of 3. (This is equivalent to a temperature change of a factor of 9.) The solid curves represent the results of calculations using the multifrequency radiation transport model, while the dashed curve (labelled C*) represents the escape probability results. The open symbols are taken from the results of Athay (1972).

First, it is seen that the multifrequency results are in fairly good agreement with those of Athay, but with differences ranging up to about 10% to 20%. This degree of discrepancy is larger than in the previous cases. This is not particularly worrisome, however, because the details of Athay's calculations are not provided in his book. In fact, it is not entirely clear that the expression we have used for curves D and E is the same one used as Athay, since he does not explicitly state the expression he used.

The frequency-averaged escape probability model assumes the line profile is the same at the point of emission, the point of absorption, and all points in between. Because of this, the results are insensitive to gradients in the line profile. Thus, while the escape probability results are within about 20% of the multifrequency results with no gradients, errors of up to a factor of 5 to 10 are seen for cases A and E. Thus, line profile gradients present a potentially large source of error in the escape probability model.

The physical reason the source function increases when the Doppler width increases toward the surface (cases A and B) is that photon escape is inhibited by the broader line profiles at the surface. Since most of the photons that escape originate in the line wings – where the optical depths are lowest – a broader profile near the surface acts to prevent photons emitted from the plasma interior from escaping. Just the opposite is true when the line widths (and temperature) decrease toward the surface (cases D and E). Narrower lines near the surface are less able to absorb "wing" photons emitted from the plasma interior, resulting in a decrease in the upper level populations near the surface.

2.4. Conclusions From Benchmark Calculations

The series of calculations described above serves two purposes. First, the accuracy of the angle- and frequency-averaged escape probability model has been assessed for problems involving temperature, density, and line profile gradients. Second, it tests the reliability of the multiangle, multifrequency radiative transfer model we have recently developed. Based on comparisons with the results of previously published calculations, the new multifrequency model appears to be working reliably.

The escape probability model provides reasonably accurate answers for problems with both temperature and density gradients so long as the line width remains relatively constant. However, the model does not take into account the effects of gradients in line profiles and the effects of continuum-induced photoexcitations. We have seen in the above 2-level atom calculations that such effects can change the source function (that is, the level populations) by as much as a factor of a few to an order of magnitude.

There are of course trade-offs in accuracy versus computational speed for the escape probability and multifrequency radiation transport models. The multifrequency

model has superior accuracy, while the escape probability model is faster. One approach that could be used is to use the escape probability model in hydrodynamics calculations to get time-dependent plasma conditions and use the multifrequency model as a "post-processor" to perform detailed calculations for comparisons with experimental measurements.

3. Temperature Diagnostic Using Aluminum K_α Satellite Line Emission

We have continued our work to examine the possibilities of using K_α satellite line emission as a temperature diagnostic for Al plasmas created by intense proton beams. K_α lines are produced as $2p$ electrons drop down to fill $1s$ vacancies created by the beam. As the plasma is heated to the point where M-shell ($n = 3$) electrons are stripped and the $2p$ shell becomes partially filled, small but detectable shifts in the wavelengths of the K_α lines occur. Successively higher ionization stages exhibit K_α lines with increased blue-shifts, which results from a reduction in the electron screening as vacancies appear in the $2p$ shell. The line radiation from the K_α satellites thus provides information on the ionization distribution in the target plasma.

Preliminary results of this work has been reported elsewhere (MacFarlane, Wang, and Henderson 1991; MacFarlane and Wang 1992). In our earlier work, we computed the emission from isothermal, isochoric plasmas in which the beam conditions were also assumed to be uniform. In this work we focus on line identification, relative line fluxes, and opacity effects. We have made advances in the following areas:

- Our code was modified to read in the output from KfK hydrodynamics simulations. This allows for time-dependent predictions of the K_α spectrum. A post-processor is used to compute the time-integrated spectrum.

- Proton impact ionization cross sections were computed using a more accurate numerical model. The CRE code can now compute the K_α spectrum for plasmas with nonuniform beam conditions.

- We have investigated the contribution of excited states to the K_α spectrum.

- A much better understanding of the K_α spectrum obtained in the PBFA-II experiment reported by Bailey et al. (1990) has been achieved.

- We have investigated the sensitivity of K_α line fluxes to the beam energy, and the influence of opacity effects on line profiles.

Each of these topics is discussed in detail in this section.

3.1. Atomic Physics Calculations

Proton impact ionization cross sections have been computed for Al using a plane wave Born approximation model with Hartree-Fock wave functions. Figure 3.1 compares the calculated K-shell cross sections for Al I, Al VI, and Al IX with experimental data as a function of the incident proton energy. The experimental data (Khan 1965, Rutledge 1973) is for neutral Al, and therefore should be compared with the solid curve. The calculated values are somewhat greater than those reported last year (MacFarlane, Wang, and Henderson 1991) because an improved numerical integration model is now used. We now find that the differences between the calculated and experimental cross sections are comparable to the differences between the 2 sets of experimental data ($\sim$ a few tens of percent). At relatively low energies ($\lesssim 0.5$ MeV) the calculated cross sections are seen to consistently overestimate the experimental data. At lower energies the PWBA model is less accurate because the incident proton velocity becomes less than the "orbital velocity" of the K-shell electrons.

As the ionization state of the Al plasma increases, the cross section decreases. This is shown in Figs. 3.1 and 3.2. Figure 3.2 shows that this dependence on ionization stage is roughly linear, with the Al I cross section being approximately 1.7 times greater than

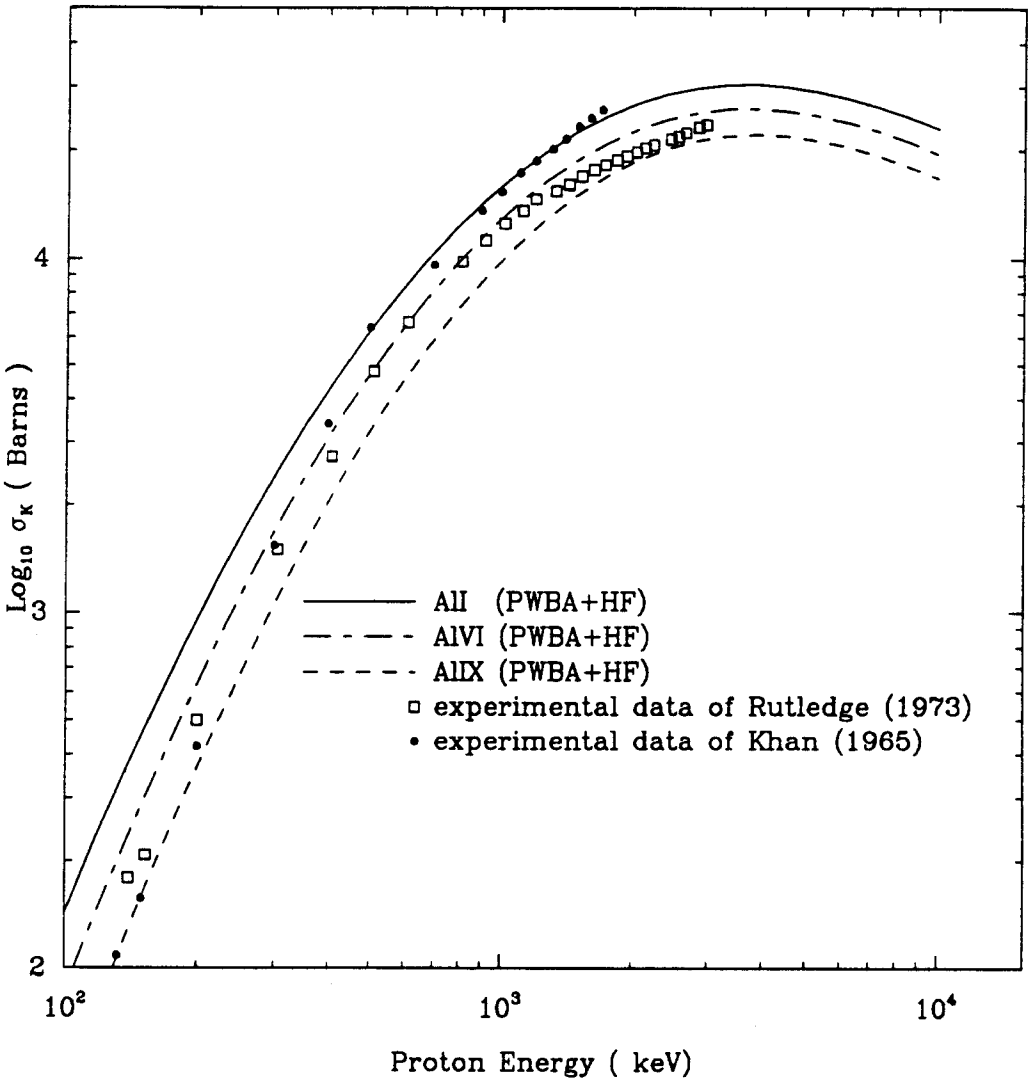

Figure 3.1. Proton impact ionization cross sections calculated for Al I, Al VI, and Al IX. Experimental data for Al I are represented by symbols.

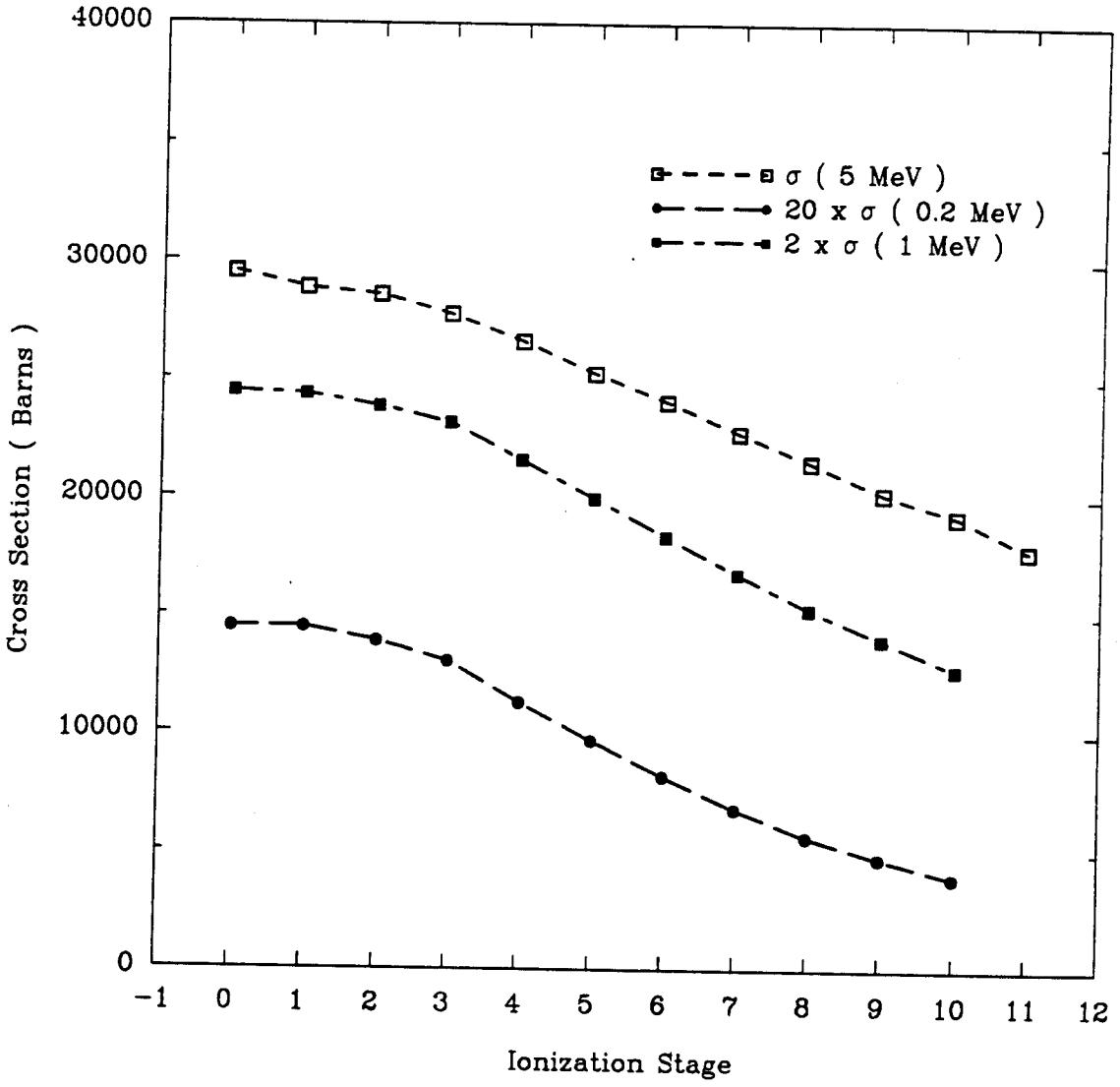

Figure 3.2. Dependence of Al K-shell ionization cross section on ionization stage. The incident proton energies are 0.2, 1, and 5 MeV. Note the 0.2 and 1 MeV results have been scaled for clarity.

that of Al XII for 5 MeV protons. The dependence on ionization stage is qualitatively similar at lower proton energies, but with a stronger quantitative dependence.

We have also examined whether the excited states of an ion can emit observable K_α lines in the spectral region of the next higher ionization stage. This possibility was originally suggested by R. Mancini of the University of Florida and J. Bailey of Sandia based on the following argument. Consider 2 states: the ground state of Al V and an excited state of Al IV where the excited electron is in the $n = 3$ state (or greater). The configuration of these states is as follows (the asterisk signifies an excited state):

Before proton impact:

Al V	$\rightarrow$	$1s^2\,2s^2\,2p^5$
Al IV*	$\rightarrow$	$1s^2\,2s^2\,2p^5\,3s^1$

After proton impact:

Al V	$\rightarrow$	$1s^1\,2s^2\,2p^5$
Al IV*	$\rightarrow$	$1s^1\,2s^2\,2p^5\,3s^1$

After K_α emission:

Al V	$\rightarrow$	$1s^2\,2s^2\,2p^4$
Al IV*	$\rightarrow$	$1s^2\,2s^2\,2p^4\,3s^1$

Note that the electronic configuration for the $n = 1$ and $n = 2$ shells of Al IV* and Al V are identical. Because the $3s$ electron is in an outer shell, it does not contribute significantly to the binding energy of the $2p$ electron that undergoes spontaneous decay. Thus, the wavelength for Al IV* should be similar to Al V.

We have attempted to address the following questions. What precisely are the wavelengths of the excited state transitions? Are the excited states sufficiently populated that they produce an observable K_α flux? We address the first question here. The second question is addressed in Section 3.2.4.

Figure 3.3 shows the K_α spectrum observed in the PBFA-II experiment and below it, two stick spectra indicating the calculated wavelengths of the K_α lines. The top stick spectrum includes only the low-lying states of each ion, while the bottom spectrum also includes excited state contributions from Al IV and Al V. For the excited states, only those states with an electron in the $3s$ shell are considered. One could also expect similar wavelengths for excited states with $3p$, $3d$, $4s$, etc. electrons as well. The wavelengths were computed using a multiconfiguration Hartree-Fock model with relativistic mass and Darwin corrections (Fischer 1978).

It is seen that about 12 lines from Al V* have wavelengths in the spectral region of Al VI, while at least 4 lines of Al IV* have wavelengths near those of Al V. Thus, in principle the Al V to Al IX features identified by Bailey et al. (1990) could include significant components from excited states of Al IV to Al VIII.

3.2. CRE Calculations of Al K_α Spectra

We have performed a series of CRE calculations to predict K_α emission spectra for conditions relevant to KALIF experiments. The primary objective of this year's work was to establish a procedure where we could use the results from KATACO simulations to predict time-dependent and time-integrated K_α spectra. In addition, we studied a number of physical effects which can influence the spectrum. These include: (1) the relationship between the plasma temperature, ionization state, and K_α line fluxes; (2) the sensitivity of the K_α spectrum to the beam energy; (3) its sensitivity to photoexcitation, photoionization, and gradients in plasma conditions; (4) the difference between spectra emitted from the front side and rear side of the target; (5) the contribution from excited states; and (6) the sensitivity of line shapes to the opacity. Each of these effects are

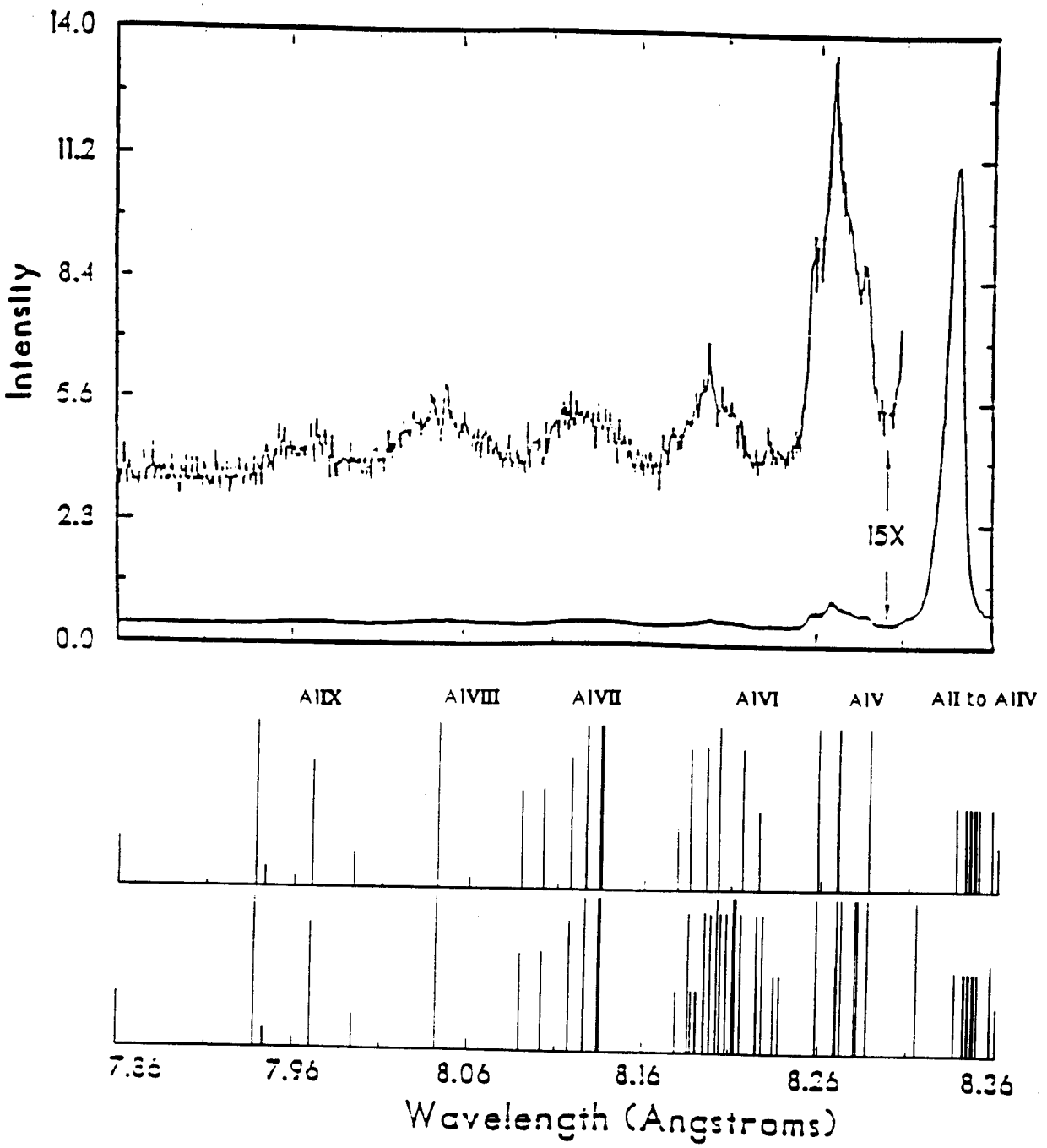

Figure 3.3. (Top) Time-integrated Al K_α spectrum obtained in PBFA-II experiment. (Middle) Stick spectrum indicating calculated wavelengths of K_α lines for low-lying states of Al ions. (Bottom) Same as upper stick spectrum, but including K_α lines from excited states of Al IV and Al V.

described below. At the end of this section, we also present a brief summary of our CRE calculations to simulate the experimental PBFA-II spectrum of Bailey et al. (1990).

3.2.1. Relation Between Temperature, Ionization State, and K_α Spectrum

Calculations were performed for targets with spatially uniform plasma and beam conditions to study the relationship between the temperature, ionization state, and K_α spectrum. Because of opacity effects, the dominant ionization stage generally does not emit the greatest K_α flux. To study this effect, we computed the spectrum for plasmas with the following conditions:

T(EV)	n/n_{solid}	L(μm)
2	0.33	100
15	0.10	100
40	0.033	100

Note that the density decreases while the slab thickness remains at 100 μm. Thus, the optical depths tend to decrease as the temperature increases.

Results are shown in Figs. 3.4–3.6. At $T = 2$ eV, the dominant ionization stages are Al I and Al II. The K_α line radiation is unimpeded by resonant self-absorption. On the other hand, the Al I K_β line flux ($\lambda = 7.95$ Å) is reduced by line opacity. (Note that we again follow the convention of referring to a K_α line from an ion by its ionization stage *prior* to proton impact ionization.) The continuum optical depth in this case due to L-shell photoabsorption is about $\tau_{cont} = 4$. At $T = 15$ eV, Al III and IV are the dominant ionization stages. The optical depths of these lines range up to about 30. At these temperatures, thermal excitation causes many ions to be excited to states which contain $2p$ vacancies. The Al V lines have an optical depth $\sim$1. Their fluxes are comparable to those of Al III and Al IV because the latter lines suffer from self-attenuation effects. At

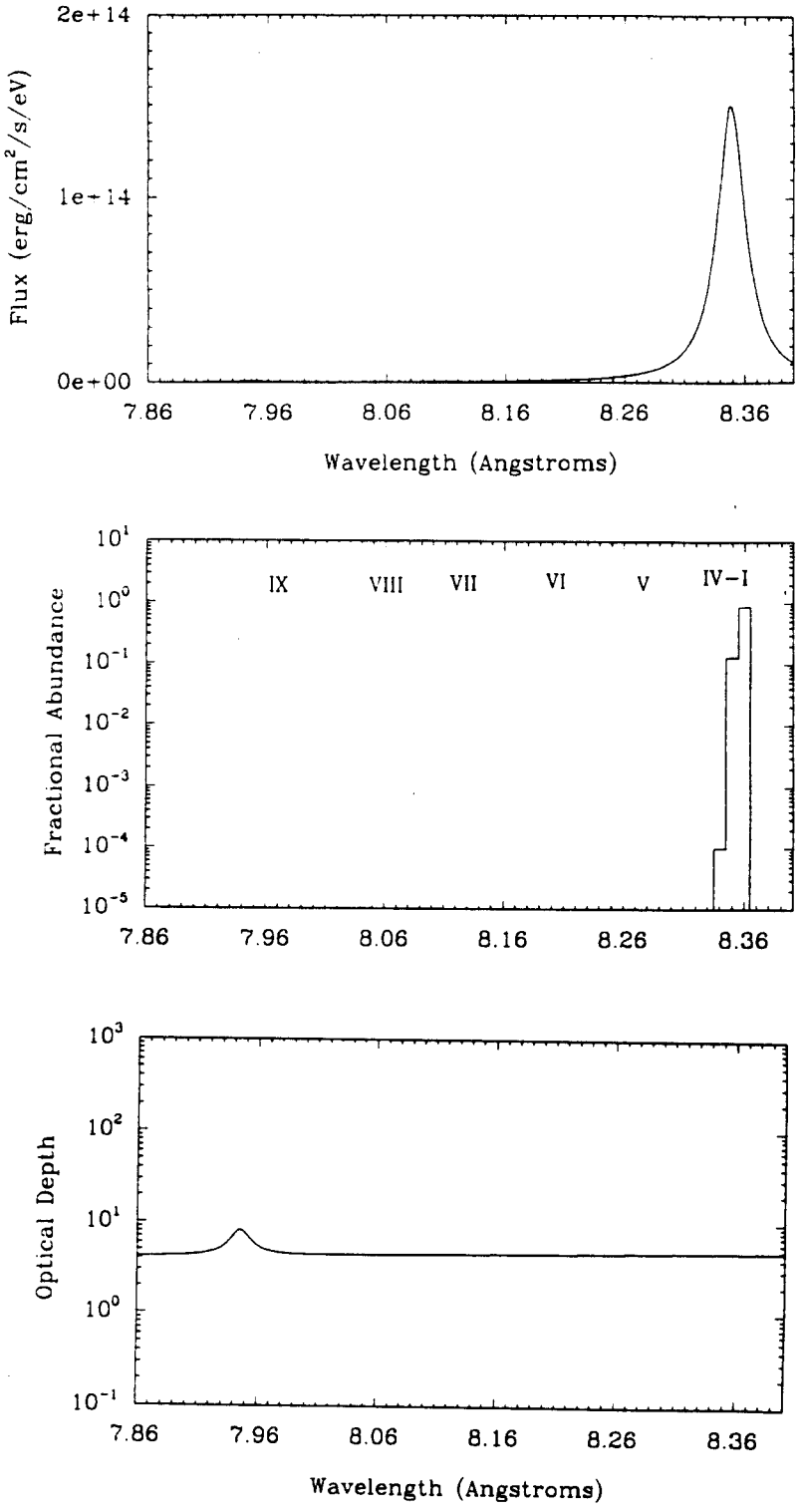

Figure 3.4. Calculated K_α flux (top), ionization distribution (middle), and optical depth for Al plasma with $T = 2$ eV, $n = \frac{1}{3} n_0$, and $L = 100\,\mu$m.

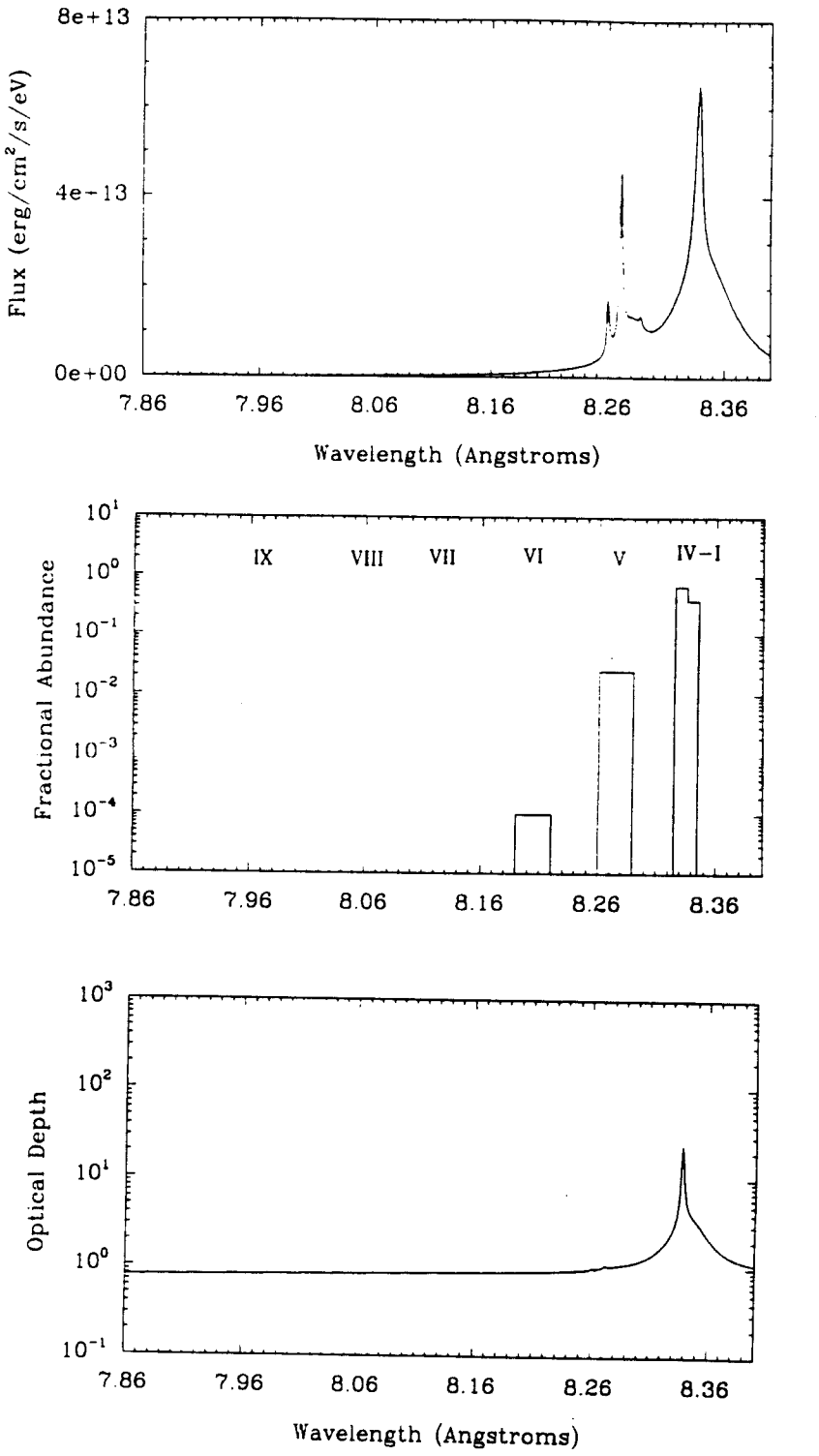

Figure 3.5. Same as Fig. 3.4, but for $T = 15$ eV, $n = 0.1\, n_0$, and $L = 100\, \mu$m.

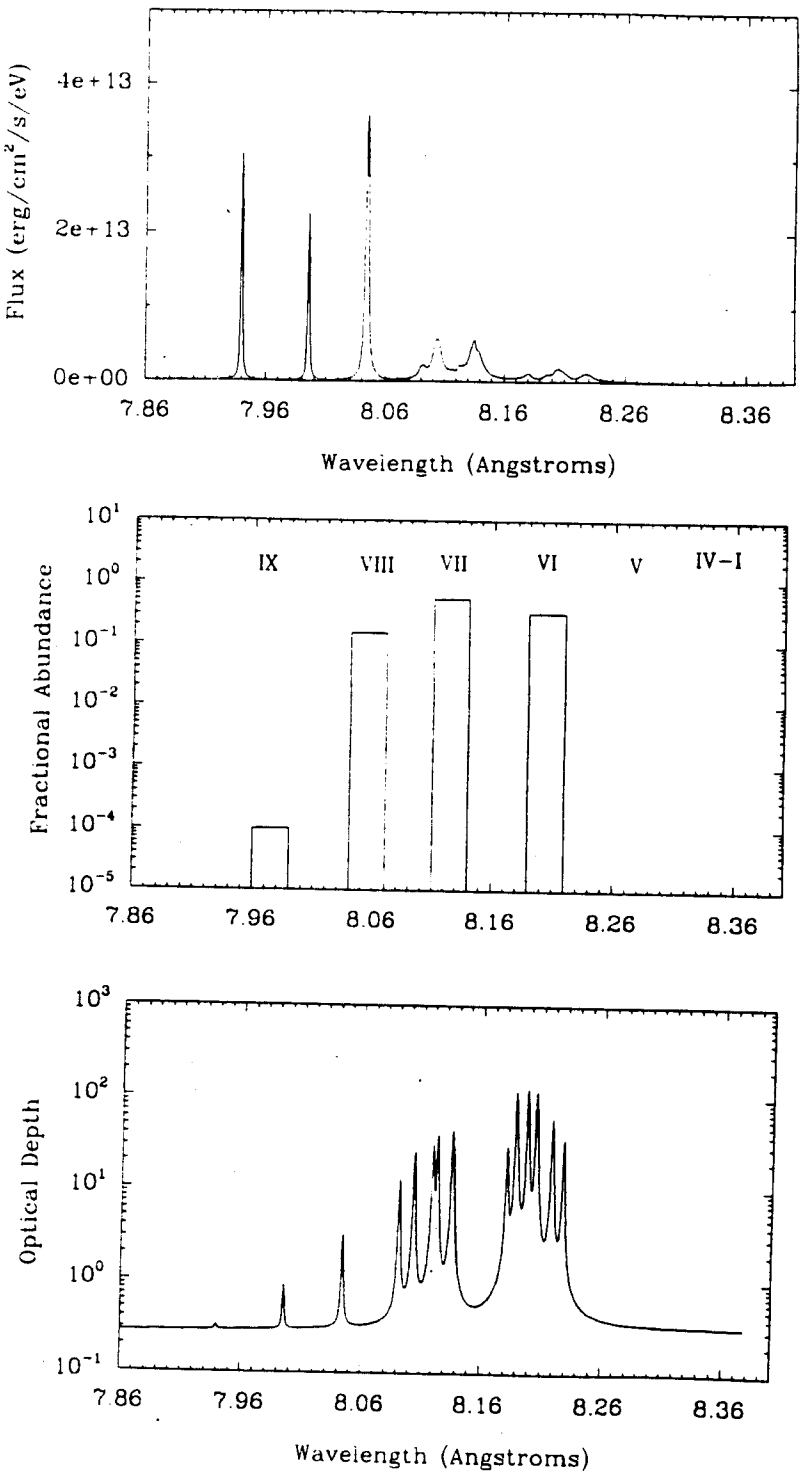

Figure 3.6. Same as Fig. 3.4, but for $T = 40$ eV, $n = \frac{1}{30} n_0$, and $L = 100\,\mu$m.

$T = 40$ eV, lines from Al VIII and Al IX show the highest fluxes. This occurs despite the fact that Al VII is the dominant ionization stage. The Al VI and Al VII lines are substantially attenuated by resonant self-absorption.

It is clear from these figures that ions with an ionization stage higher than the most abundant stage can exhibit a significant flux. On the other hand, the lines from relatively low ionization stages show smaller intensities. The reasons for this can be understood from the following analysis. The specific intensity along a path normal to a slab boundary can be written as (Mihalas 1978):

$$I_\nu = \int_0^{T_\nu} S_\nu e^{-t_\nu}\, dt_\nu \,, \tag{3.1}$$

where S_ν is the source function at frequency ν, and T_ν is the total optical depth along the line of sight. The source function for an isolated line is given by:

$$S = \left(\frac{2h\nu_0^3}{c^2}\right) \left[\left(\frac{n_\ell\, g_u}{n_u\, g_\ell}\right) - 1\right]^{-1} \tag{3.2}$$

$$\simeq \left(\frac{2h\nu_0^3}{c^2}\right) \frac{n_u\, g_\ell}{n_\ell\, g_u} \,, \tag{3.3}$$

where n_ℓ and n_u are the population densities of the lower and upper level, respectively, g_ℓ and g_u are the statistical weights, ν_0 is the transition frequency, and h and c are Planck's constant and the speed of light. The second relation is valid for K_α lines because $n_u \ll n_\ell$.

Assuming a spatially uniform plasma, Eq. (3.1) becomes:

$$I_\nu = S_\ell \left[1 - e^{-T_\nu}\right] , \tag{3.4}$$

which yields

$$I_\nu = \begin{cases} S_\ell & \text{for optically thick lines, and} \\ S_\ell\, T_\nu & \text{for optically thin lines } (T_\nu \ll 1) \,. \end{cases} \tag{3.5}$$

Thus, the line intensity is simply proportional to n_u/n_ℓ. This ratio can be estimated as follows. The steady-state rate equation for the upper state can be expressed as

$$\frac{dn_u}{dt} = n_{L,j-1}\, R_p - n_{u,j}\, D_{u\ell} = 0\,, \tag{3.6}$$

where R_p is the proton impact ionization rate, $D_{u\ell}$ is the total depopulating rate for the upper state, and $n_{L,j-1}$ is the density of a low-lying state (L) of the $j-1$ ionization stage. The relation between the density of the lower state of the K_α transition and $n_{L,j-1}$ can be estimated from the Saha equation:

$$n_{L,j-1} = n_{\ell,j}\, n_e \left(\frac{g_{L,j-1}}{g_{\ell,j}}\right) (1.66 \times 10^{-22}\ \mathrm{cm}^3\ \mathrm{eV}^{3/2})\, T^{-3/2}\, e^{\Delta E/T}\,, \tag{3.7}$$

where ΔE is the energy difference between states $(L, j-1)$ and (ℓ, j), and n_e is the electron density. Combining Eqs. (3.3), (3.6), and (3.7) we get:

$$S_\ell = (1.66 \times 10^{-22}\ \mathrm{cm}^3\ \mathrm{eV}^{3/2}) \left(\frac{2h\nu^3}{c^2}\right) \frac{g_{L,j-1}}{g_{u,j}} \frac{R_p}{D_{u\ell}} \cdot n_e\, T^{-3/2}\, e^{\Delta E/T}\,. \tag{3.8}$$

Assuming a weak temperature dependence for $D_{u\ell}$, the line flux falls off as $T^{-3/2}\, e^{\Delta E/T}$ for a given electron density. This of course represents the temperature dependence of $n_{L,j-1}/n_{\ell,j}$. To summarize, the flux for a line from a moderate ionization stage evolves as follows. At very low temperatures, the ionization fraction is too low to significantly populate the upper state of the K_α line. As the temperature rises, the flux increases as $n_{u,j}$ increases until the line optical depth is $\sim$1. The flux then decreases as T increases at a rate roughly proportional to $T^{-3/2}\ e^{\Delta E/T}$. This simple analysis has been validated by numerical simulations.

3.2.2. Sensitivity of K_α Spectrum to the Beam Energy and Gradients in Plasma Conditions

We next discuss the sensitivity of calculated K_α spectra to the ion beam properties and certain aspects of the radiative transfer model. Let us first consider the dependence on beam energy. In KALIF beam/plasma interaction experiments it is expected that proton energies will generally range from 0.2 MeV to 1.0 MeV. We therefore ran two calculations which had identical parameters with the exception of the proton impact ionization cross section. In the first calculation the cross section corresponded to a beam energy of 1.0 MeV, while we assumed a 0.2 MeV beam energy in the second calculation. In both calculations the plasma and beam conditions were spatially uniform, with $J_{beam} = 1$ MA/cm^2, $T = 15$ eV, $n = 10^{-1}\, n_0$, and $L = 100$ μm.

Results for the two cases are shown in Fig. 3.7, where 3 curves are shown: the $E_{beam} = 1$ MeV results (solid curve), the $E_{beam} = 0.2$ MeV results (lower thin dashed curve), and the $E_{beam} = 0.2$ MeV results multiplied by 14.9 (thick dashed curve overlying the solid curve). The value 14.9 corresponds to the ratio of the 1 MeV to 0.2 MeV proton impact ionization cross sections. Clearly, the computed K_α flux is proportional to cross section at each wavelength. This is because the line flux is proportional to the population of the upper state (i.e., the autoionizing state) of the K_α transition, which in turn is proportional to the proton impact ionization rate:

$$R_p = (6.242 \text{ MA}^{-1} \text{ cm}^2 \text{ barns}^{-1} \text{ s}^{-1})\, J_{beam}\, \sigma_p\, (E_{beam})\,, \tag{3.9}$$

where σ_p is the proton impact ionization cross section. Thus, for a given beam current density, the K_α intensities for each ion are proportional to the cross section.

In the above calculations, the cross section was assumed to be independent of the ionization stage. In this case, the ratio of the Al IV (8.35 Å) to Al V (8.26–8.29 Å) cross

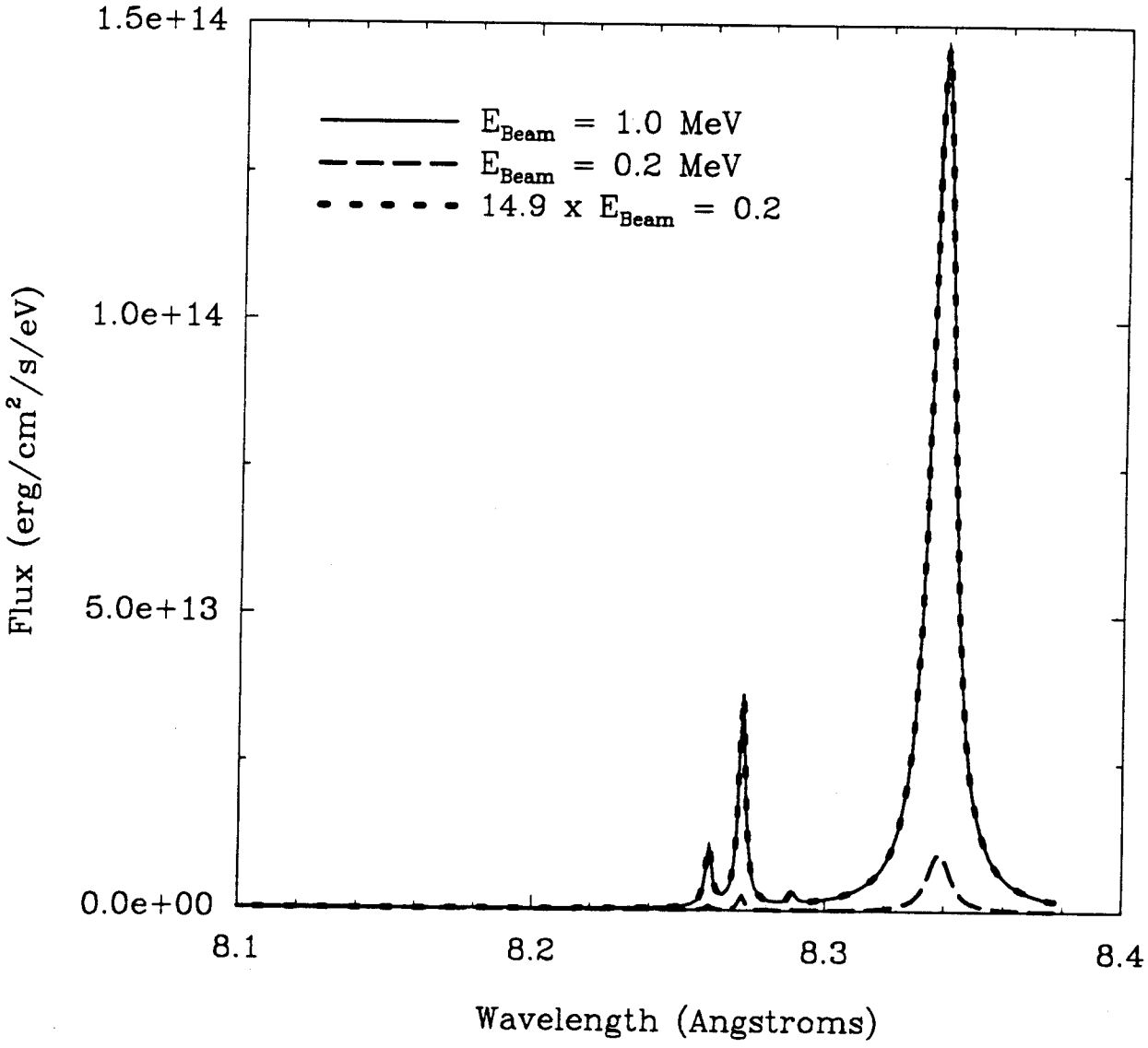

Figure 3.7. Dependence of computed K_α spectrum on proton beam energy. The flux at each wavelength is seen to be proportional to the proton impact ionization cross section. In each case, $T = 15$ eV, $n = 10^{-1}\, n_0$, $L = 100\,\mu$m, and $J_{beam} = 1$ MA/cm^2.

sections — and therefore the intensity ratio — is independent of the beam energy. However, ionization cross sections are a function of both the beam energy *and* the ionization stage (see Fig. 3.2). PWBA calculations indicate that for Al IV and Al V the ratio of the cross sections at 1.0 MeV to 0.2 MeV is 17.7 and 19.0, respectively. Thus, the *ratio* of Al V to Al IV lines should be 7% lower in the $E_{beam} = 0.2$ MeV case. A similar analysis for higher ionization stages indicates that the ratio of Al VI to Al IX intensities can change by about 30% between 0.2 and 1.0 MeV. We conclude that if one is attempting to deduce plasma or beam conditions from line intensity ratios between different ions, the dependence of the proton impact ionization cross section on the beam energy and ionization stage should be considered in the analysis.

We have also investigated the sensitivity of calculated K_α spectra to the details of our radiative transfer model for conditions relevant to KALIF experiments. We find that although the presence of the radiation field can change the populations of moderately excited (non-autoionizing) states by up to a factor of 4 for a plasma temperature of 50 eV, the K_α spectrum changes very little. Part of this is due to the fact that we do not presently consider contributions to the K_α spectrum from excited states for ions above Al V (see Sec. 3.2.4). The calculated spectrum at $T = 50$ eV includes contributions from low-lying states only. At $T = 15$ eV, a temperature where Al IV and Al V fluxes dominate, the populations change very little ($< 4\%$) when photoexcitation effects are ignored. Thus, the calculated K_α spectra tend to be insensitive to the details of the radiation transport scheme in modeling gradients in the line profiles and continuum-induced photoexcitations. It is possible, however, that if *excited* states contribute significantly to the K_α spectrum at moderately high temperatures (say, 40-50 eV), that the effects of radiation transport become more important. This is because the radiation field has a greater influence on the excited state populations than on those of lower energy states.

3.2.3. Comparison of Front and Rear Side Spectra

In the hydrodynamic simulations discussed later in this section, the protons at late times ($t \gtrsim 50$ ns) are stopped before they reach the rear side of the plasma. This gives rise to a rather interesting line absorption effect for the following reasons. K_α line emission originates only in regions where the beam is producing vacancies in the K-shell. No emission originates in the rear-side region if the beam is stopped prior to reaching that point. The non-emitting region, however, is still capable of resonant self-absorption (as well as continuum absorption) if the plasma is sufficiently hot. This phenomenon can lead to absorption lines superimposed on the K_α satellite spectrum.

To illustrate this point, consider an isothermal, isochoric slab with $T = 15$ eV, $n = 10^{-1}\, n_0$, and $L = 100\,\mu$m. Now assume that a 1 MeV, 1 MA/cm^2 proton beam irradiates the front half only (the beam is stopped after penetrating 50 μm). We now address the question: what are the differences between the front side and rear side spectra? This is shown in Fig. 3.8, where the K_α spectra for the front and rear side are shown. The front side spectrum shows prominent emission lines for Al I - IV and Al V. The rear side intensities are dramatically reduced by resonant self-absorbtion. This is especially true for the Al IV peak because its line opacities are higher at this temperature. Note also the appearance of an absorption line at the center of Al I - IV feature.

This effect raises some interesting issues concerning plasma diagnostics. One possibility for an experiment is that the target could be placed at an angle to the incoming beam so that both the front side and rear side spectra could be observed. The front side spectrum provides information about the beam-irradiated region, while the rear side spectrum provides additional information about the absorption region. One could also place thin layers (diagnostic tracers) in both regions tailored to look at such effects. One

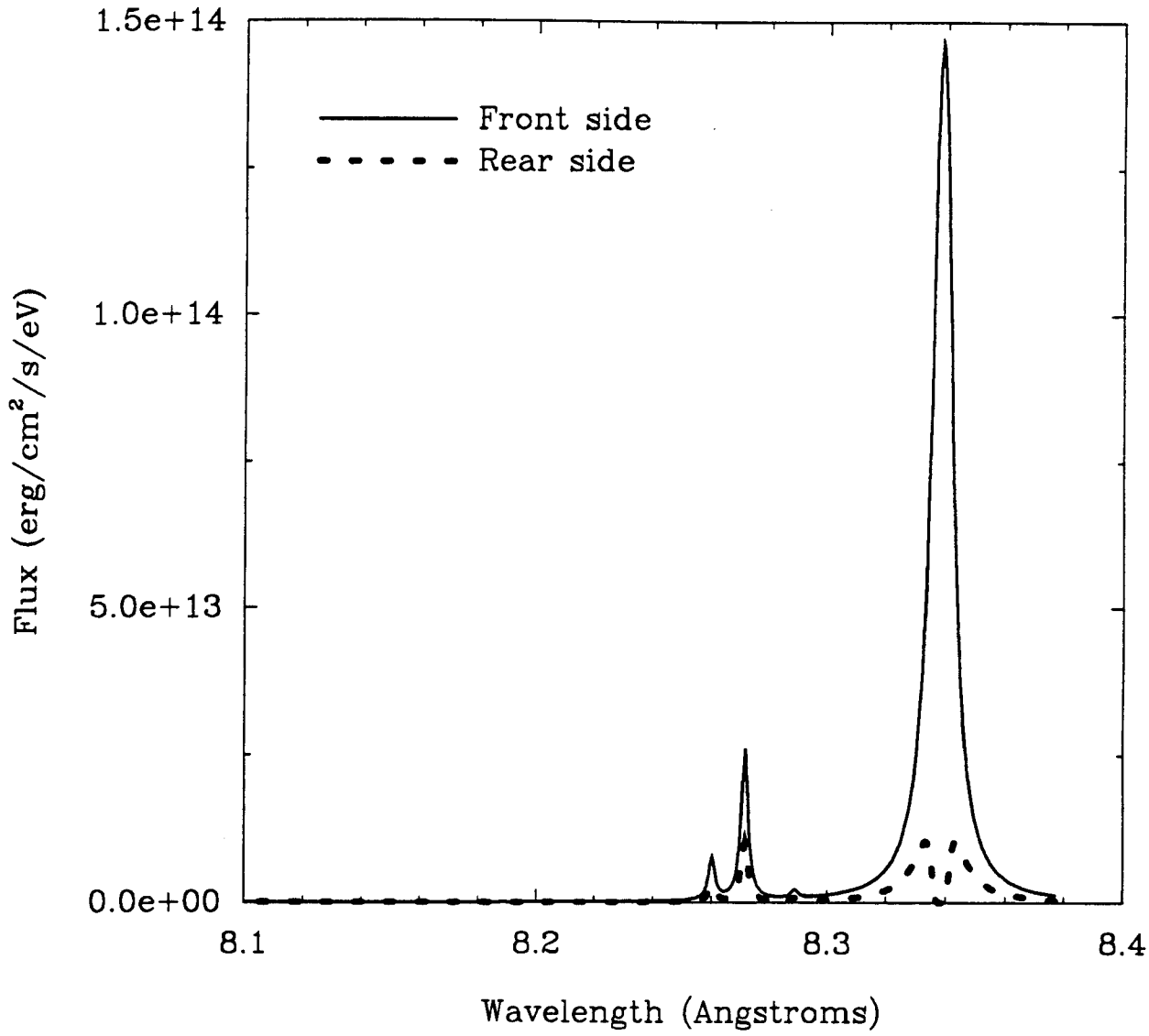

Figure 3.8. Comparison of front and rear side spectra for a $T = 15$ eV, $n = 10^{-1}\, n_0$, and $L = 100\,\mu$m Al plasma. The beam irradiates the front side, and is assumed to have a range of 50 μm.

potential concern is that the absorbing region could reduce the flux to the point that detection becomes difficult. In any case, these effects should be carefully considered in designing a target experiment.

3.2.4. Contributions from Excited States to K_α Spectra

In Section 3.1 it was shown that the wavelengths of K_α lines produced from excited states of one ion are similar to those for low-lying states of the next higher ionization stage. We now address the question of whether these levels are sufficiently populated that they can contribute in an observable way to the K_α spectrum.

To address this question we performed two similar sets of CRE calculations using slightly different atomic models. In the first case we considered only low-lying levels of each ion (i.e., for Al IV - IX, no electrons in the $n = 3$ shell), while in the second calculation we additionally consider excited states with the valence electron in the $3s$ shell for Al IV and Al V. Results are shown in Fig. 3.9 for the Al V spectral feature. When the excited states are included a broad feature on the long wavelength side of the central peak is seen (near 8.28 Å). This is qualitatively consistent with the PBFA-II spectrum (lower plot), where a broad feature is clearly seen between the central peak and long wavelength peak ($^1P \rightarrow {}^1S$ transition). Additional contributions could also arise from other excited states (with electrons in $3p$ and $3d$ states). It is also important to note that the line widths for the excited state lines are considerably larger than ground state lines. Because the excited states are more easily perturbed by their surroundings, their lifetimes are shorter. This suggests that the features observed in the PBFA-II spectrum may contain a significant component from excited states.

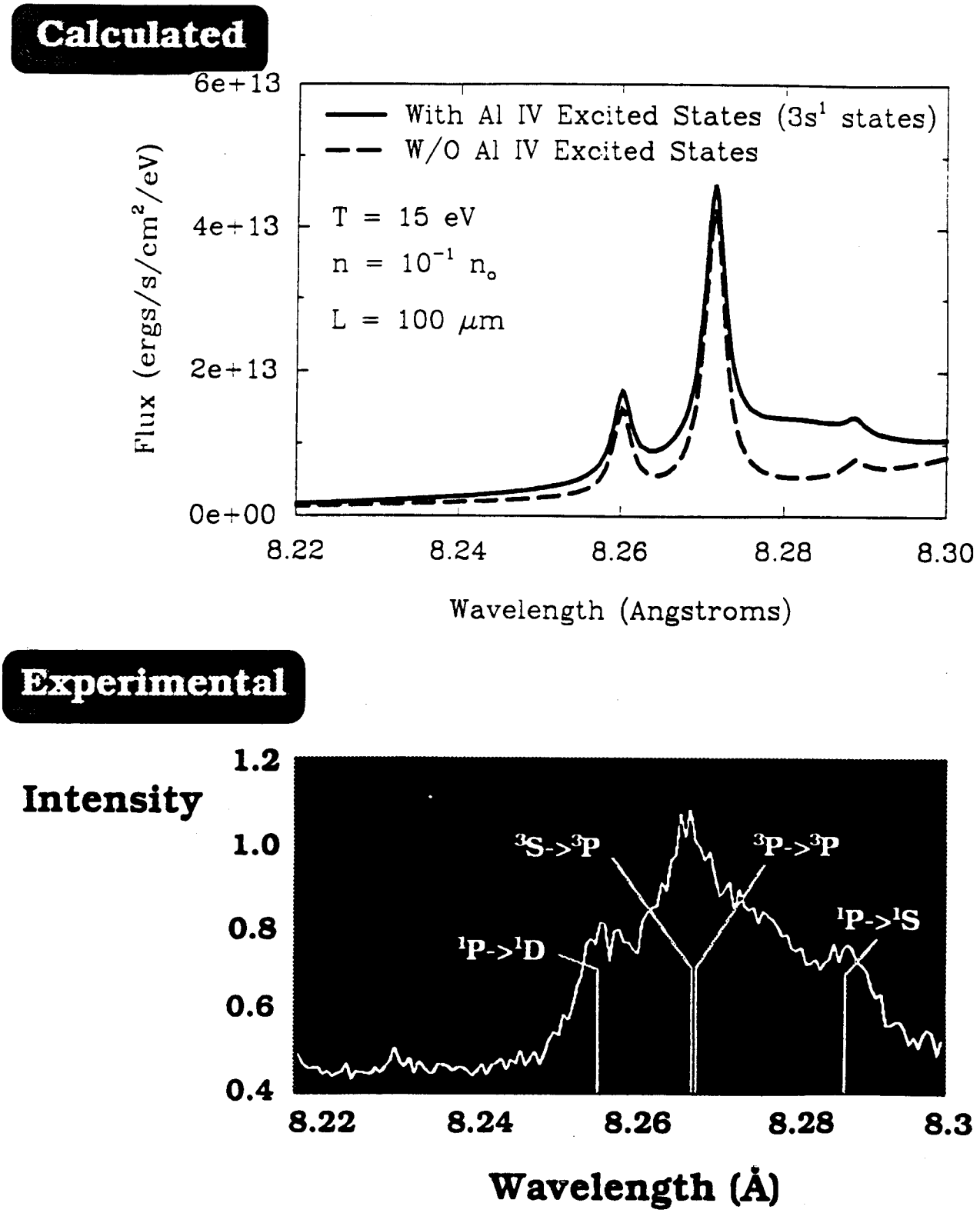

Figure 3.9. (Top) Calculated K_α spectrum for Al V spectral region. The solid curve includes the contribution from excited states of Al IV, whereas the dashed curve does not. (Bottom) Experimental data obtained in PBFA-II experiment (from Bailey et al. 1990).

3.2.5. Sensitivity of Line Shapes to Opacity Effects

A series of calculations was performed to assess the effects of opacity broadening on observed line profiles. The plasma parameters were $T = 20$ eV, $n = 10^{-1}\, n_0$, and $L = 0.1$ cm. The effects of the radiation field on the level populations (i.e., photoexcitation and photoionization) were ignored in these calculations. The differences that arise in the computed spectra are therefore due only to attenuation effects. Calculations were run for 3 cases: (1) optically thin (no attenuation); (2) bound-bound attenuation only; and (3) both bound-bound and bound-free attenuation. (Free-free opacities are negligible at these photon energies.)

Results for the Al V spectral region are shown in Fig. 3.10. All results are shown on a logarithmic scale in the plot at the left, while the latter 2 cases are shown on a linear scale at the right. Note the influence that bound-free opacity has on the line shape (right plot). This of course makes it extremely difficult to deduce plasma conditions from observed line *profiles* for targets of this thickness. Also note that the relative intensity of the central peak to the long wavelength peak changes by a factor of about 3 when opacity effects are included (left plot). The physical reasons for this can be understood from the analysis in Section 3.2.1. The point we wish to emphasize is that when plasmas are optically thick, the conditions deduced from an optically thin analysis may very well be inaccurate.

3.2.6. K_α Spectra Using Results from KATACO Simulations

We performed CRE calculations for Al targets using the temperature and density profiles from KATACO/MEDUSA simulations to predict time-dependent and time-integrated K_α spectra for KALIF experiments. The hydrodynamics results were furnished

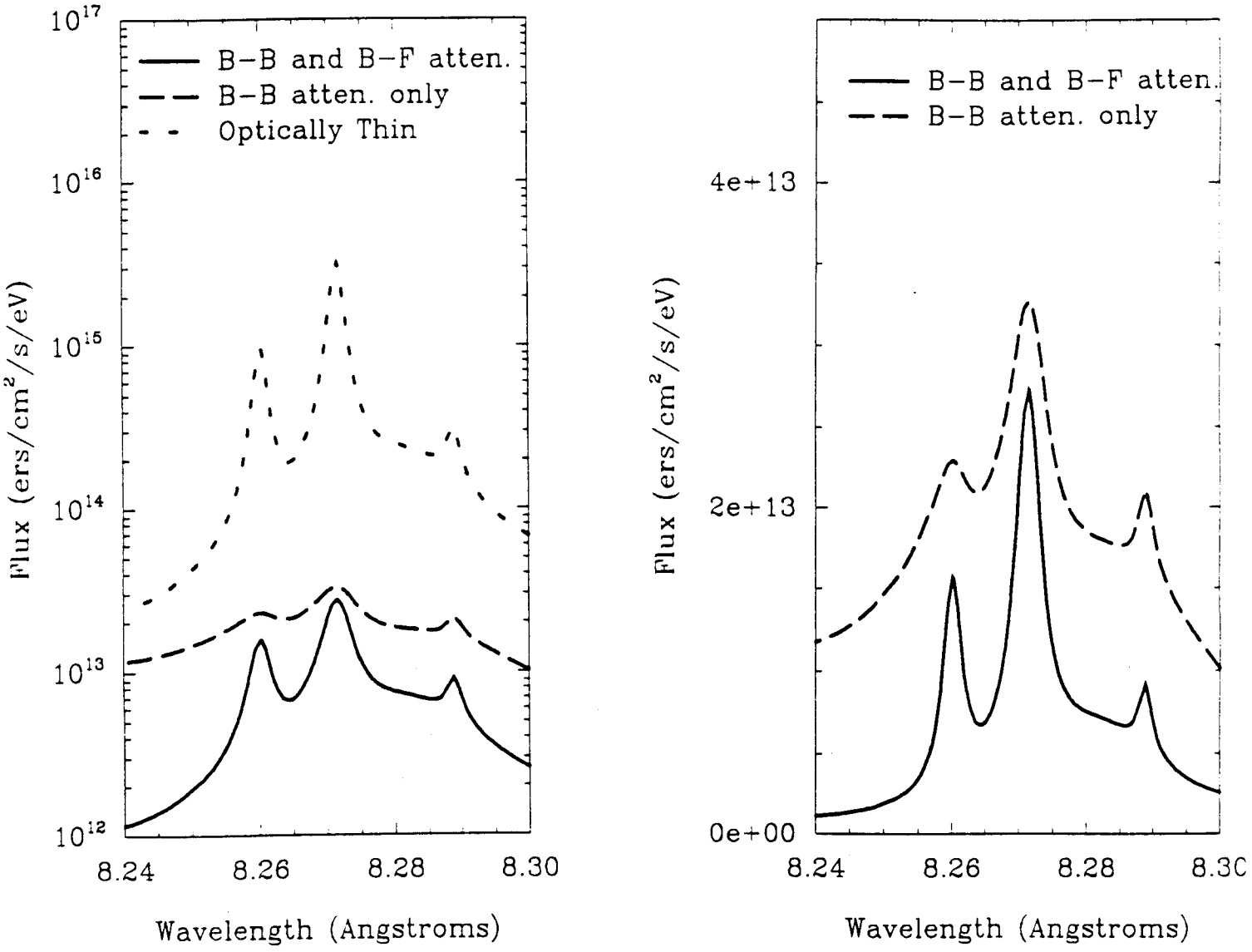

Figure 3.10. Sensitivity of K_α line shapes to opacity broadening. Both relative line intensities and line shapes are influenced by both bound-bound and bound-free opacity effects.

by B. Goel of KfK. These results are illustrated in Fig. 3.11 – 3.13. The peak temperature in the Al plasma is seen to be about 25–30 eV. Note that at the times when K_α lines are being emitted by hot material ($T \gtrsim 15$ eV) the densities are generally between 10^{-3} and $10^{-2}\, n_0$. It is also seen that at early times ($t \lesssim 50$ ns) the beam penetrates through the entire target, while at later times the protons are stopped before reaching the rear side. This is presumably due to range shortening caused by the heating of the target.

The computed K_α spectra at simulation times of 20, 40, 60, and 80 ns are shown in Fig. 3.14. (Note the fluxes are on a log scale.) These spectra are computed for the rear (non-irradiated) side of the target. The corresponding optical depths are shown in Fig. 3.15. The Al I - IV K_α ($\lambda = 8.34$ Å) and K_β ($\lambda = 7.95$ Å) peaks are clearly seen at 20 ns. Note, however, that the K_β flux is significantly reduced by opacity effects, while there is virtually no line opacity for the K_α line at this time. This is because the opacity of the K_β line (a $3p \rightarrow 1s$ transition) depends on the number of ions with vacancies in the $3p$ shell, while that of the K_α line (a $2p \rightarrow 1s$ transition) depends on vacancies in the $2p$ shell. At low temperatures, there are very few vacancies in the $2p$ shell for Al I–IV.

At 40 ns, Al I–IV and Al V emission lines are clearly visible. At this time the beam penetrates all the way through the target (see Fig. 3.13). At 60 ns, emission lines from Al VII and Al VIII are seen. A very interesting effect is seen for the Al IV through Al VI lines. Superimposed on their emission lines are deep absorption features which are caused by resonant absorption in the region not being irradiated by the beam. According to the hydrodynamics simulations the protons are stopped after penetrating two-thirds of the way through the target. At 80 ns, qualitatively similar features are seen.

Results for the time-dependent K_α spectra were run through a post-processor to compute the time-integrated spectrum. Results are shown in Fig. 3.16. The bottom plot shows identical results as the top plot, but on a different scale so that the Al V–Al VIII

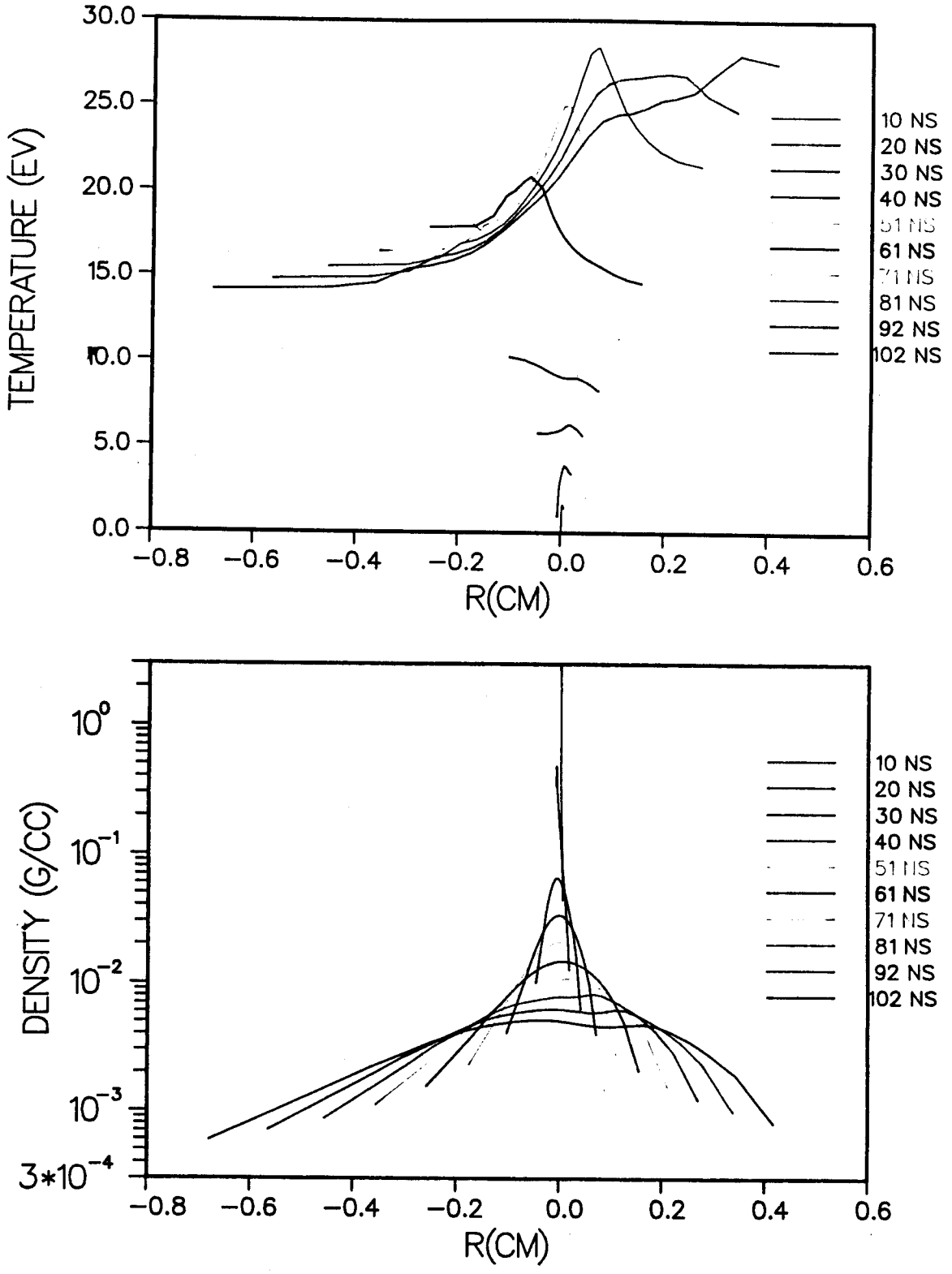

Figure 3.11. Temperature (top) and density (bottom) evolution in an Al target calculated using MEDUSA/KATACO. The beam enters the plasma from the right. The K_α spectra are computed assuming the detectors are at the left.

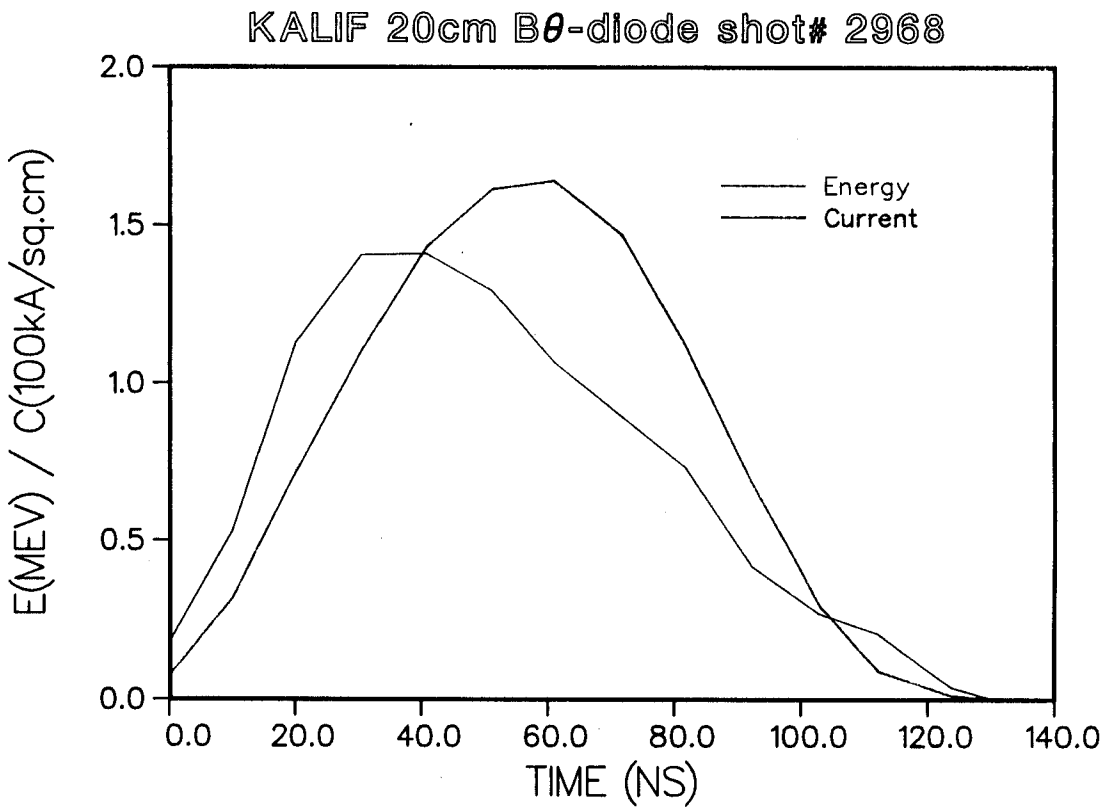

Figure 3.12. Time-dependent proton beam conditions used for MEDUSA/KATACO calculation.

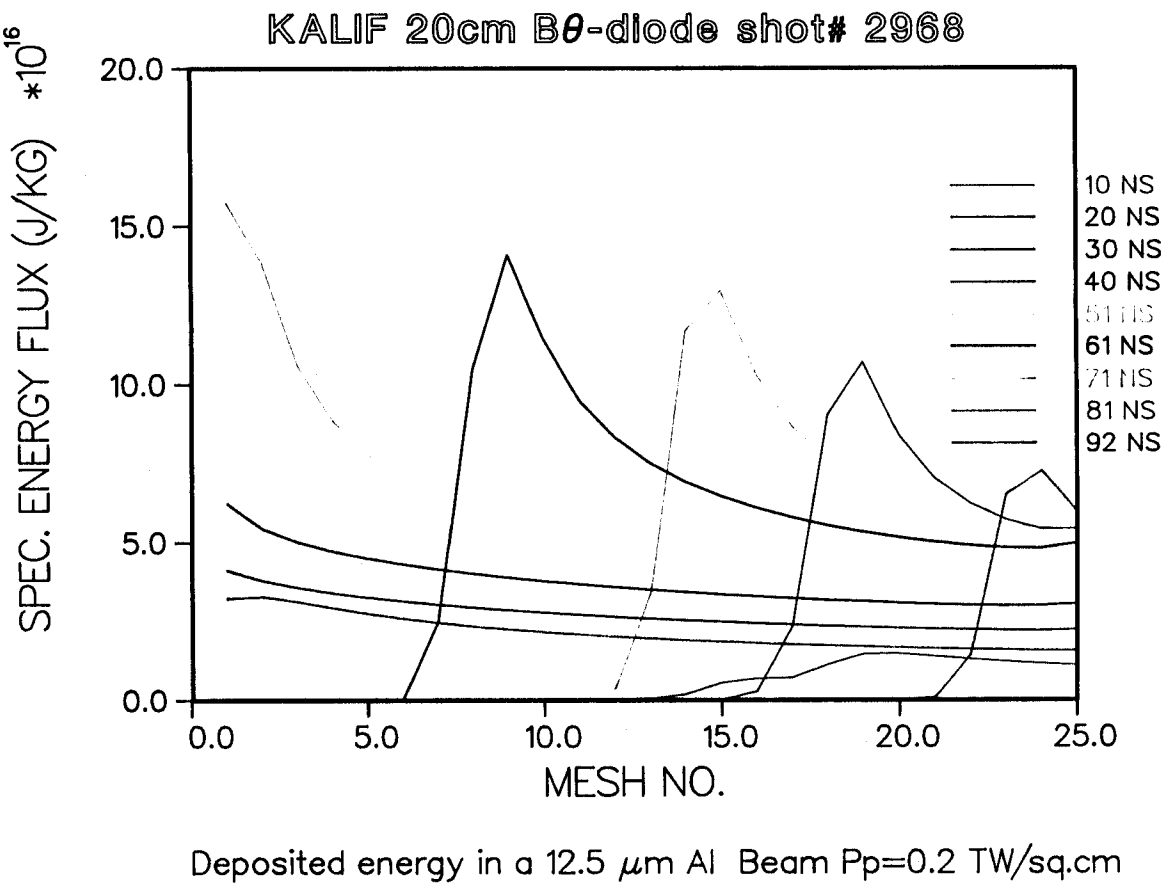

Figure 3.13. Specific energy deposition profiles from MEDUSA/KATACO simulation.

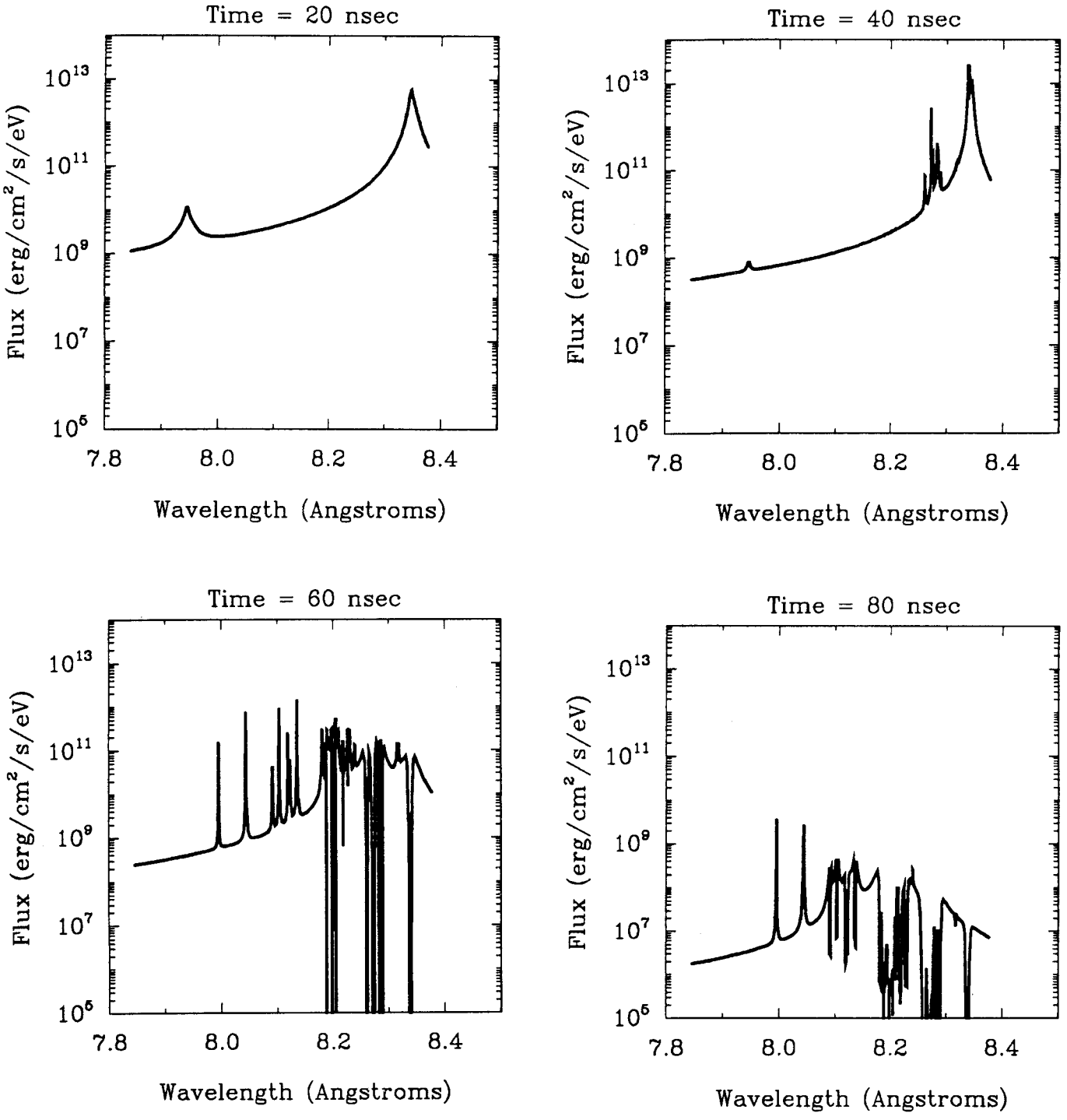

Figure 3.14. Time-dependent K_α spectra computed using temperature and density distributions in Fig. 3.11.

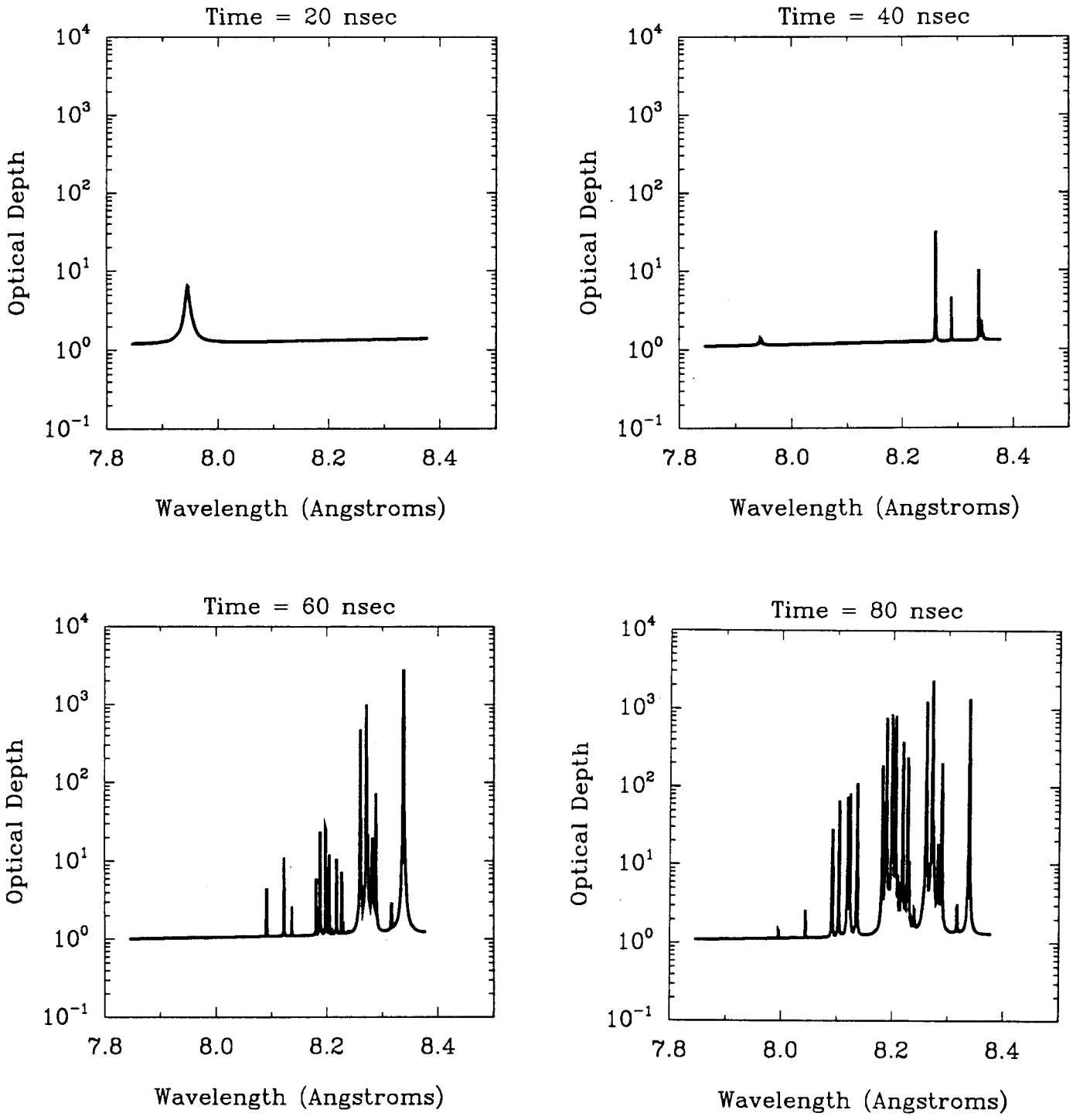

Figure 3.15. Frequency-dependent optical depths for the calculations shown in Fig. 3.14.

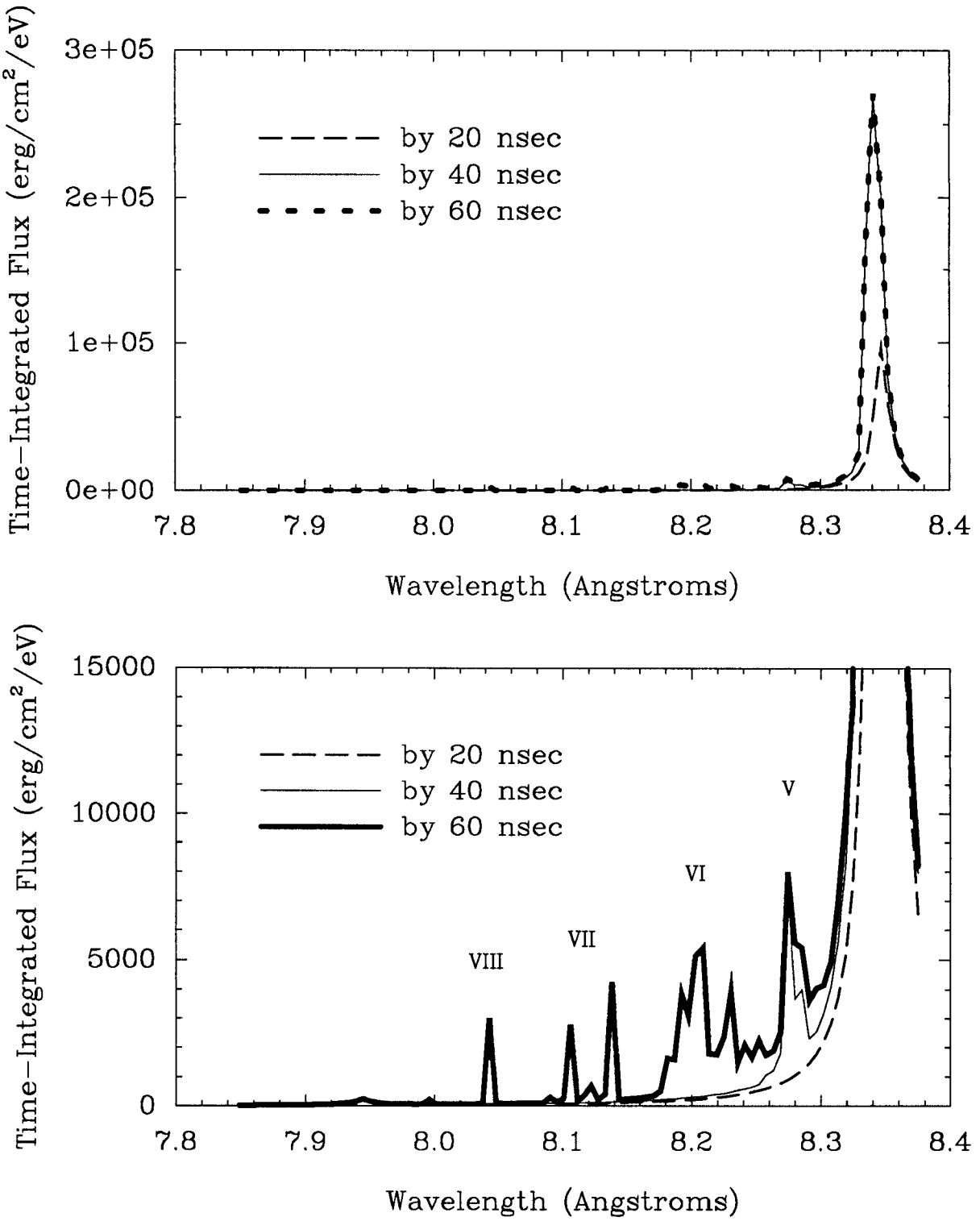

Figure 3.16. Time-integrated Al K_α spectrum calculated using temperature and density distributions from MEDUSA/KATACO simulation. The lower plot shows results on a different scale so that the Al V to Al VIII features can be more clearly seen.

features are more clearly seen. The results are displayed with a 1 eV resolution to mimic the resolution of a spectrometer. The 3 curves represent the K_α flux emitted by 20, 40, and 60 ns.

The highest flux comes from Al I–IV lines at early times ($t \lesssim 40$ ns) in the experiment. The relatively high flux for these lines is in large part due to the fact that resonant self-absorption is negligible at low temperatures ($T \lesssim 5$ eV). The bulk of the emission from Al VI to Al VIII lines comes at times after 40 ns.

The peak intensities in KALIF experiments will be lower than those in the PBFA-II experiments. A reduction by a factor of 2-3 could be expected because of the reduced cross section for a lower energy beam. In addition, the peak current density in KALIF experiments is about 0.15 MA/cm^2 compared with 1.1 MA/cm^2 in PBFA-II experiments. Since the K_α flux is proportional to the current density times the ionization cross section, one could expect lower K_α fluxes for KALIF experiments by a factor of about 15-20. This may stress the detection limits of the spectrometer. This, however, need not necessarily be a problem because there are differences in the experimental geometry, detector locations, sources of noise, and so forth.

3.2.7. Summary of Analysis of PBFA-II K_α Spectrum

A similar set of calculations was performed using hydrodynamics results from Sandia National Laboratories. The purpose of the calculations was to obtain a better understanding of the physical processes affecting the K_α spectrum and to check for consistency between the PBFA-II spectrum and the hydrodynamics simulations. In this section, we will only show the final results. A detailed description of the calculations is currently being prepared for publication. We will of course send a copy of this to KfK as soon as it is completed.

The calculated time-integrated spectrum is compared to the experimental spectrum in Fig. 3.17. The inset in both plots show the magnified flux for the Al V–Al IX ions. The overall agreement between the calculated and experimental spectra is quite good. The main conclusions from this study are as follows:

1. The relatively high flux from Al I–IV is a result of the absence of resonant self-absorption at early times when the plasma is relatively cool ($T \lesssim 5$ eV).

2. Excited states of ions (with valence electrons in the $n = 3$ state) likely contribute to the spectrum. These lines may very well be responsible for the rather broad features of the higher ionization stages.

3. The feature labelled Al IX in the experimental plot is very possibly due not to Al IX, but to K_β from Al I (at early times) and/or excited states of Al VIII at later times.

4. The plasma is in general optically thick to both L-shell photoabsorption and resonant self-absorption. Opacity effects significantly influence observed line shapes.

5. The K_α lines are emitted from the blowoff region. The lack of absorption features suggests that very little warm material which is outside the beam irradiated zone lies between the emitting region and the detector.

6. The CRE and hydrodynamics simulations suggest that the maximum temperature attained in the blowoff region is roughly 30 eV. The hydrodynamics simulations also suggest the peak temperature attained deep inside the plasma is about 45 eV.

.5

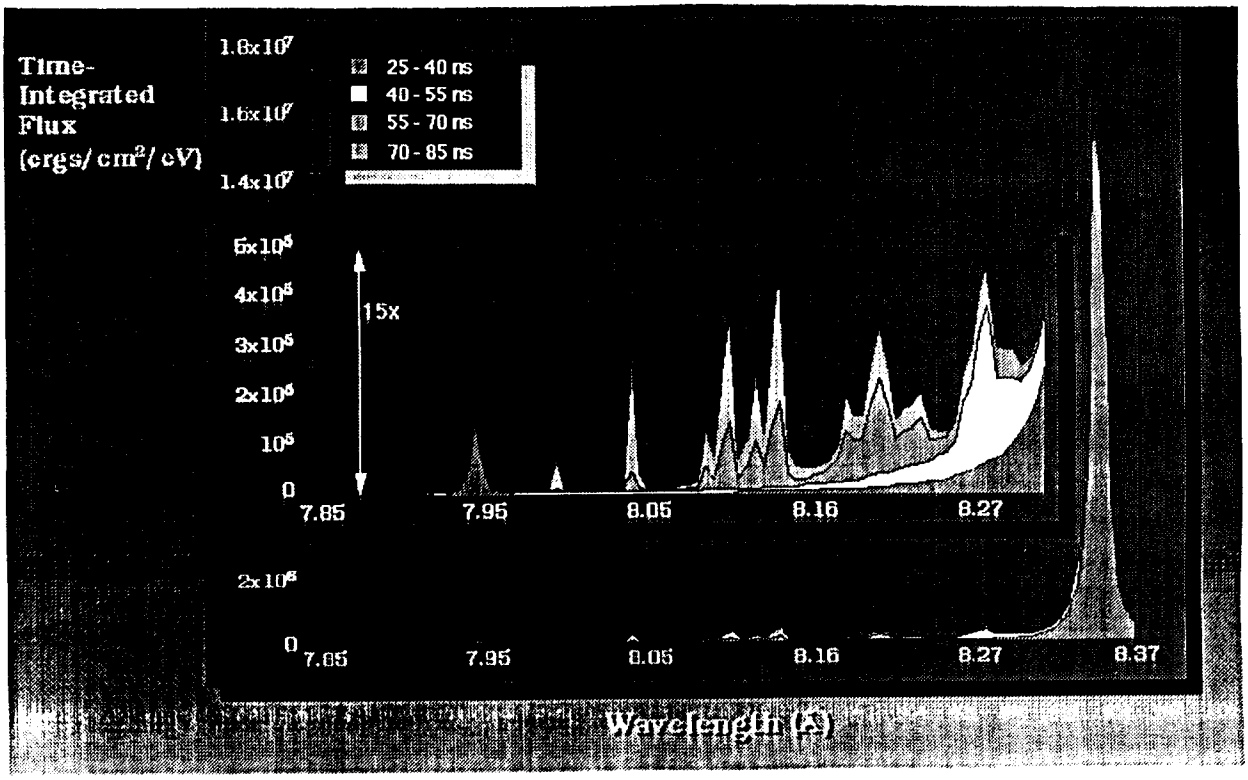

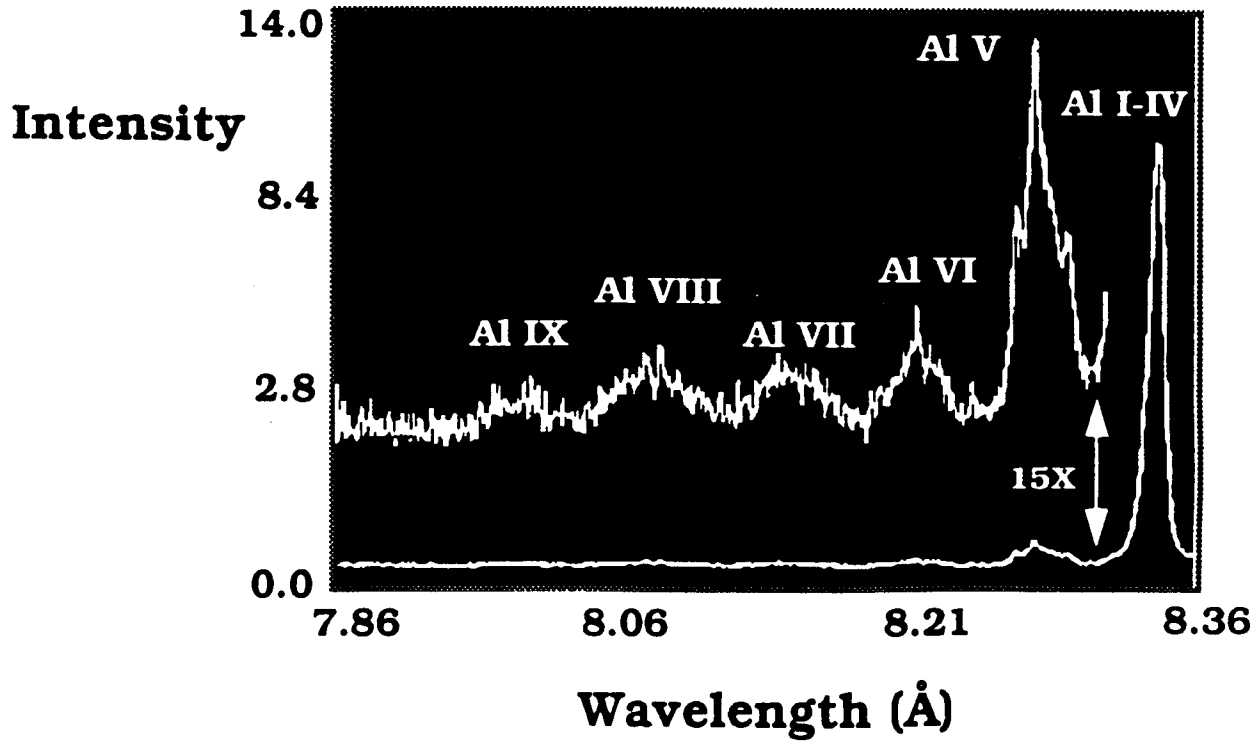

Figure 3.17. (Top) Time-integrated Al K_α spectrum calculated using temperature and density distributions from Sandia hydrodynamics simulation. (Bottom) Time-integrated K_α spectrum obtained from PBFA-II experiment. Insets in each figure show Al V–Al IX spectral features more clearly.

3.2.8. Discussion of Al K_α Simulations

Measuring the inner-shell line emission from light ion beam-irradiated targets presents good opportunities for determining target plasma conditions. The good agreement between calculated and experimental spectra suggests that a reasonably good understanding of the major physical processes that influence the K_α spectrum is being achieved. Opacity effects have been shown that have a very significant effect on the observed spectrum obtained in the PBFA-II spectrum reported by Bailey et al. (1990). However, one could also try to use very thin layers of Al (or some similar material) as a diagnostic tracer. This could eliminate problems caused by opacity, as well as provide some "spatial resolution" for diagnosing plasma conditions.

4. Diagnosing Beam Conditions from Gold Inner-Shell Line Emission

4.1. Introduction

One method which can be used to diagnose beam conditions in light ion beam fusion experiments is to examine x-ray line ratios (or band ratios) that result from beam-induced inner-shell transitions of high-Z materials. This approach can be used as either an independent check on other measurements, such as Rutherford scattering, or alternatively it can take the place of other measurements in experiments where practical considerations (target geometry, target composition, restrictions on positioning detectors, etc.) make other data acquisition techniques difficult or impossible. Thus, in principal the x-ray line diagnostic could allow for greater flexibility in designing target experiments.

Inner-shell x-ray lines are produced as a result of the interaction of the beam with the target material. As an example, consider the case of an $L\alpha_1$ line (see Fig. 4.1). The L_{III} state is populated as a $2p_{3/2}$ electron is ejected by proton-impact ionization. This vacancy is rapidly filled by outer-shell electrons. A fraction of these transitions results in the emission of a photon, while in other transitions additional outer-shell electrons can be ejected. In the case of the $L\alpha_1$ line, an electron in the $3d_{5/2}$ subshell drops down to fill the $2p_{3/2}$ subshell. This results in a photon with an energy of 9.7 keV being emitted.

In this section, we present calculations which show how the proton beam energy can be deduced from the ratios of M-shell to L-shell lines. This approach has been used previously in PBFA-II experiments (Derzon et al. 1992) as an independent check on other diagnostics. Calculations have been performed for the cases with $10^{-1} - 10^{1}$ MeV protons interacting with gold foils. This range of proton energies was chosen to cover the range of energies in KALIF and PFBA-II experiments.

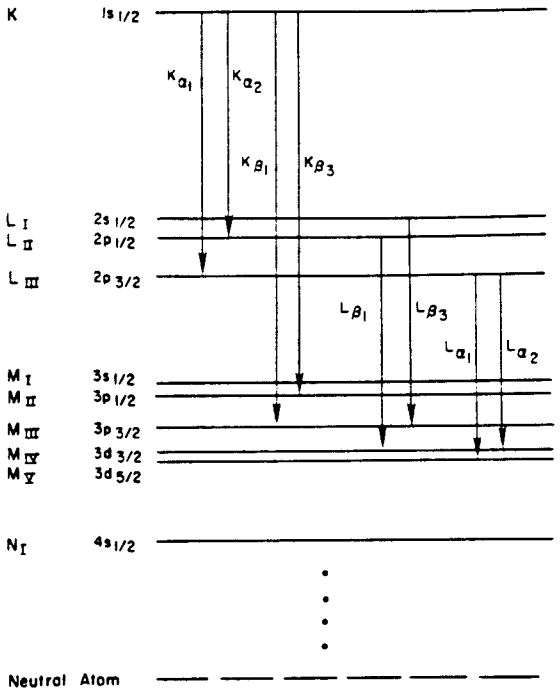

Lower level		Upper level: K	L_I	L_{II}	L_{III}	M_I	M_{II}	M_{III}	M_{IV}	M_V
K	$1s_{1/2}$									
L_I	$2s_{1/2}$									
L_{II}	$2p_{1/2}$	α_2								
L_{III}	$2p_{3/2}$	α_1								
M_I	$3s_{1/2}$		---	η	l					
M_{II}	$3p_{1/2}$	β_3	β_4	---	t					
M_{III}	$3p_{3/2}$	β_1	β_3	β_{17}	s					
M_{IV}	$3d_{3/2}$	β_5^{II}	β_{10}	β_1	α_2					
M_V	$3d_{5/2}$	β_5^{I}	β_9	---	α_1					
N_I	$4s_{1/2}$		---	γ_5	β_6		---	---		
N_{II}	$4p_{1/2}$	β_2^{II}	γ_2	---	---	---			ζ_2	
N_{III}	$4p_{3/2}$	β_2^{I}	γ_3	---	---	---			---	ζ_1
N_{IV}	$4d_{3/2}$	β_4	---	γ_1	β_{15}		---	γ_2		
N_V	$4d_{5/2}$	β_4	γ_{11}	---	β_2			γ_1		
N_{VI}	$4f_{5/2}$		---	v	u'				β	α_2
N_{VII}	$4f_{7/2}$		---		u					α_1
O_I	$5s_{1/2}$		---	γ_8	β_7			---		
O_{II}	$5p_{1/2}$	---	γ_4'	---	---				---	
O_{III}	$5p_{3/2}$	---	γ_4	---	---	---				
O_{IV}	$5d_{3/2}$		---	γ_6	β_5		---	---		
O_V	$5d_{5/2}$		---		β_5			---		

[a]Dashes indicate observed transitions that have not been given special symbols.

Figure 4.1. Energy level diagram and nomenclature for x-ray transitions (from Cowan 1981).

4.2. Energy Level and Cross Section Calculations

A multiconfiguration Dirac-Fock model (Grant et al. 1980) was used to compute energy levels and oscillator strengths. This is a fully relativistic model which includes the effects of the transverse (Breit) interaction, self-energy, and vacuum polarization (McKenzie et al. 1980). Calculated binding energies for the lowest 8 ionization stages of Au are plotted in Fig. 4.2 for electrons of each subshell. It is seen that the binding energy of the K-, L-, and M-shell electrons are relatively insensitive to the presence of outermost electrons. On the other hand, the binding energies of the N- and O-shell electrons show a noticeable dependence on ionization stage. This range of ionization corresponds to plasma temperatures of up to approximately 50 eV.

Tables 4.1 through 4.3 show the calculated transition energies and spontaneous decay rates for the principal K-, L-, and M-shell lines. As a check on the reliability of our calculations, the computed K and L rates are compared with the results of Scofield (1969), who used a relativistic Hartree-Slater model. The 2 sets of results are seen to be in good agreement, with typical differences being $\lesssim 10\%$.

Proton-impact ionization cross sections were computed using a plane-wave Born approximation (PWBA) model with Hartree-Fock wave functions. Results for the proton-impact ionization cross sections for the K and L subshells of Au are presented in Figs. 4.3 and 4.4. Shown with the calculated cross sections (solid curves) are results from experimental data (symbols) by Paul and Muhr (1986) for K-shell and by Datz et al. (1974) for L-shell. It is seen that for each of the subshells the calculations are in good agreement with experiment. Typical differences are on the order of a couple tens of percent.

Table 4.1. Principal K Transition Energies and Rates

Transition	ΔE(2Ry)	A(1/s)	$A_{scofild}$ (1/s)
L1 – K	2452.568	2.543(13)	2.766(13)
L2 – K	2475.649	2.144(16)	2.183(16)
L3 – K	2543.084	3.937(16)	3.713(16)
M2 – K	2866.051	4.071(15)	4.087(15)
M3 – K	2881.090	7.880(15)	7.904(15)
M4 – K	2897.978	0.977(13)	1.018(14)
M5 – K	2901.169	1.196(14)	1.262(14)
N2 – K	2958.447	9.576(14)	9.576(14)
N3 – K	2962.070	1.844(16)	1.8696(16)
N4 – K	2969.266	5.531(13)	5.867(13)

Table 4.2. Principal L Transition Energies and Rates

Transition	ΔE(2Ry)	A(1/s)	$A_{scofild}$ (1/s)
L2 – L1	23.082	4.351(13)	4.438(13)
M2 – L1	413.483	5.638(14)	5.670(14)
M3 – L1	428.521	6.848(14)	6.536(14)
M4 – L1	445.410	1.901(13)	1.885(13)
M5 – L1	448.601	2.800(13)	2.827(13)
N2 – L1	505.875	1.410(14)	1.429(14)
N3 – L1	509.501	1.933(14)	1.778(14)
O2 – L1	526.897	2.558(13)	2.568(13)
O3 – L1	527.637	3.111(13)	3.086(13)
M1 – L2	383.116	6.541(13)	6.384(13)
M3 – L2	408.441	2.413(12)	2.447(12)
M4 – L2	425.328	2.291(15)	2.378(15)
N1 – L2	481.395	1.588(13)	1.642(13)
N4 – L2	496.617	4.531(14)	4.697(14)
O4 – L2	509.566	4.288(13)	4.423(13)
M1 – L3	383.116	1.103(14)	1.0336(14)
M4 – L3	425.328	1.801(15)	1.845(15)
N1 – L3	481.396	2.391(13)	2.432(13)
N4 – L3	496.616	3.871(13)	3.815(13)
N5 – L3	497.265	3.192(14)	3.450(14)
O5 – L3	509.626	2.997(13)	3.420(13)

Table 4.3. Principal M Transition Energies and Rates

Transition	ΔE(2Ry)	A(1/s)
M3 – M1	25.325	3.781(12)
N2 – M1	102.682	2.563(13)
N3 – M1	106.305	2.862(13)
O2 – M1	123.700	2.701(12)
M4 – M2	31.927	5.987(12)
N1 – M2	87.994	8.891(12)
N4 – M2	103.215	5.606(13)
O1 – M2	112.064	0.923(12)
O4 – M2	116.164	1.411(12)
M5 – M3	20.079	1.727(12)
N1 – M3	72.955	1.399(13)
N4 – M3	88.176	6.102(12)
N5 – M3	88.825	5.121(13)
O1 – M3	97.025	2.671(12)
O5 – M3	101.185	3.665(12)
N2 – M4	60.470	5.969(12)
N3 – M4	64.093	4.852(11)
N4 – M4	81.258	9.443(13)
N3 – M5	60.901	3.622(12)
N6 – M5	78.201	4.192(12)
N7 – M5	78.201	8.611 (13)

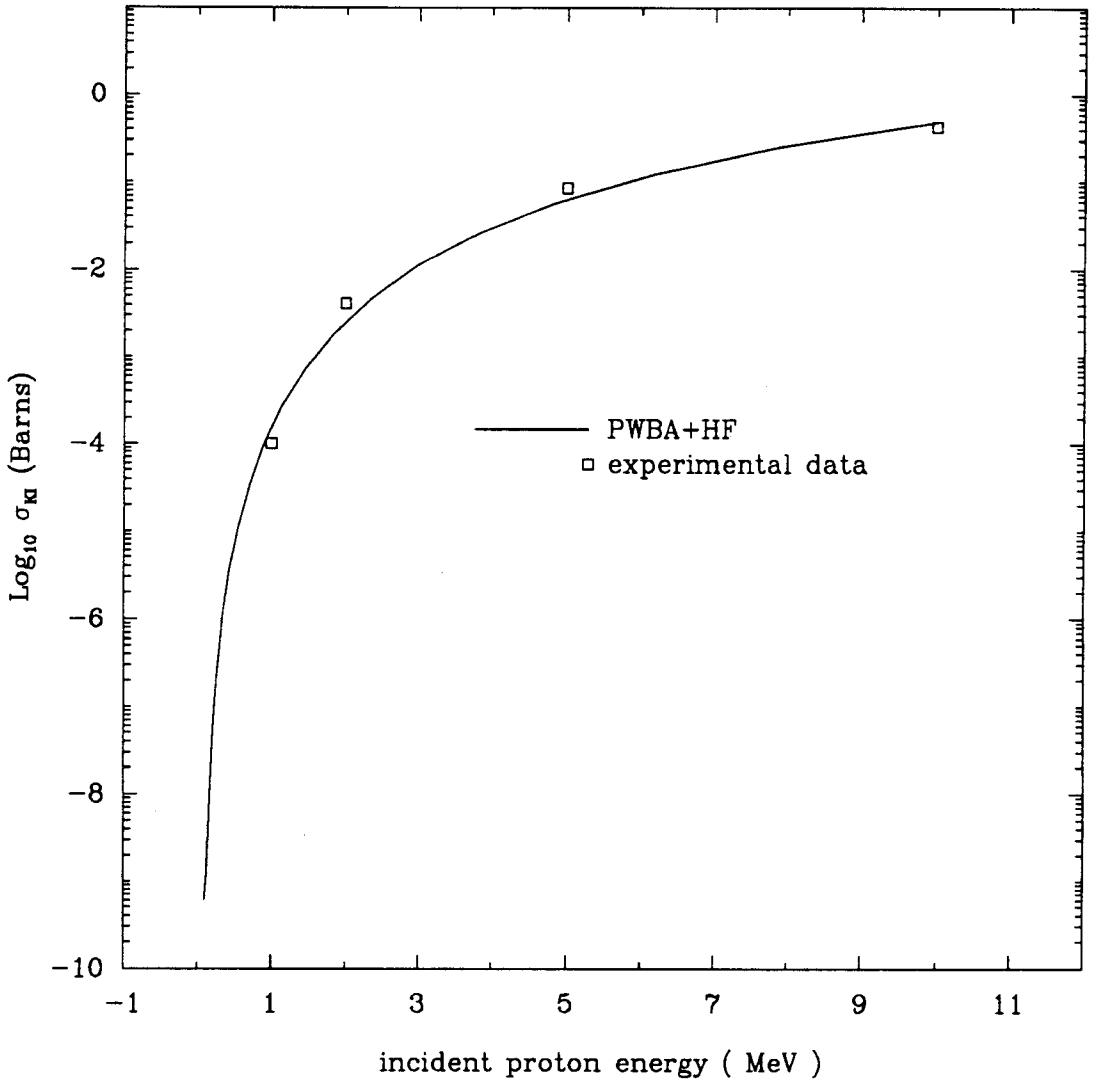

Figure 4.3. K-shell proton impact ionization cross section for Au as a function of incident proton energy. Experimental data is from Paul and Muhr (1986).

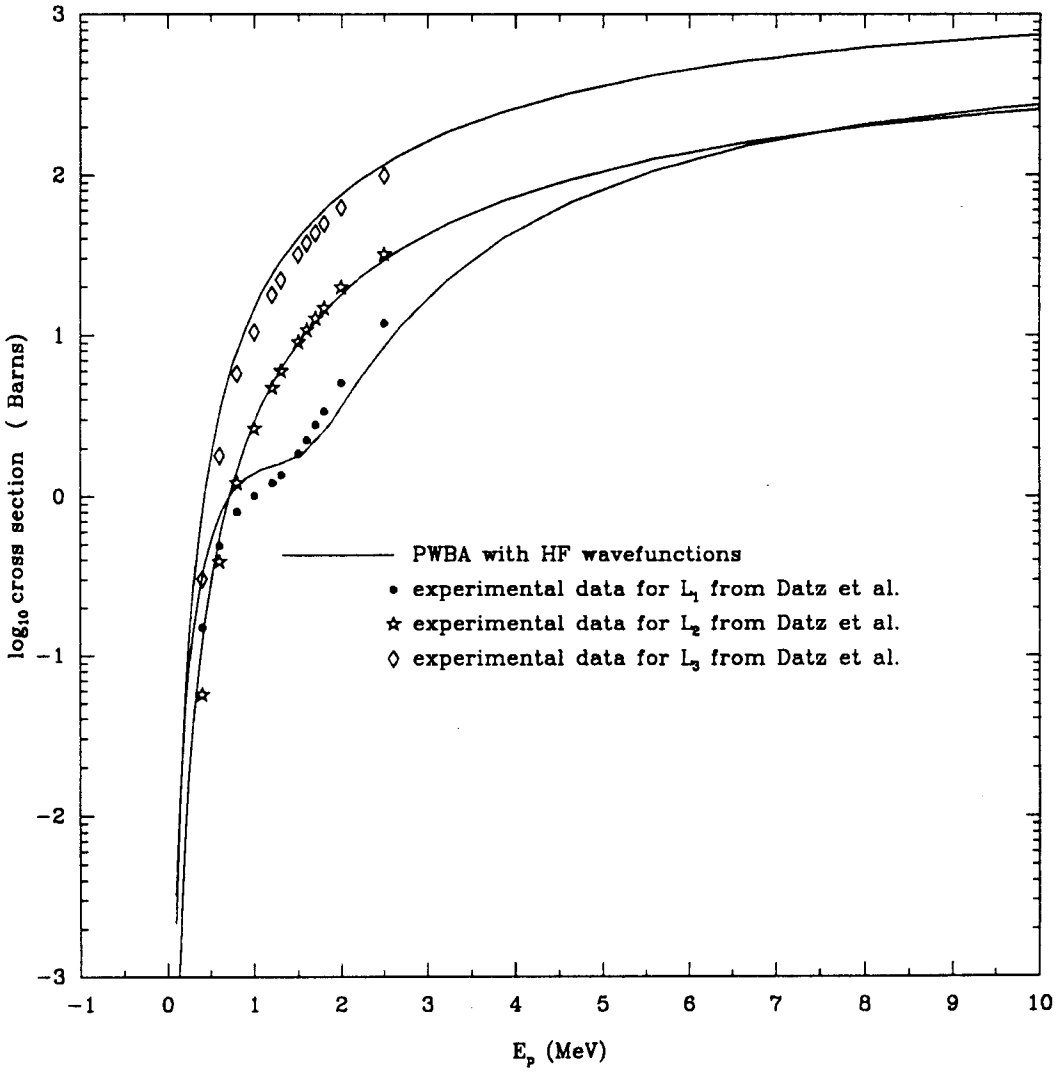

Figure 4.4. Proton impact ionization cross section for L subshells of Au.

To compute the x-ray production cross sections, one must take into account fluorescence yields, Coster-Kronig rates, and super Coster-Kronig rates. Examples of these transitions are illustrated below:

Fluorescence:

$$1s^1\,2s^2\,2p^6\,3s^2\,\cdots \rightarrow 1s^2\,2s^2\,2p^5\,3s^2\,\cdots$$

Coster-Kronig:

$$1s^2\,2s^1\,2p^6\,3s^2\,3p^6\,\cdots \rightarrow 1s^2\,2s^2\,2p^5\,3s^1\,3p^6\,\cdots$$

Super Coster-Kronig:

$$1s^2\,2s^2\,2p^6\,3s^1\,3p^6\,3d^{10}\,4s^2\,\cdots \rightarrow 1s^2\,2s^2\,2p^6\,3s^2\,3p^5\,3d^9\,4s^2\,\cdots$$

In fluorescence transitions, a photon is emitted as an inner-shell vacancy is filled by an electron from another subshell. Coster-Kronig reactions are those in which an electron undergoes a transition within the same shell (e.g., $2p \rightarrow 2s$; $L_I \rightarrow L_{III}$), with a second electron being ejected. For "normal" Coster-Kronig transitions the ejected electron originates from a different shell (the $n = 3$ shell in the example) from the transiting electron, while for super Coster-Kronig transitions the electron originates from the same shell.

To illustrate the relation between the ionization and x-ray cross sections we write the K- and L-shell x-ray production cross sections as:

$$\begin{aligned}
\underline{K}: \quad \sigma_X(K) &= \omega(K)\,\sigma_I(K) \\
\underline{L_I}: \quad \sigma_X(L_I) &= \omega(L_I)\,\sigma_I(L_I) \\
\underline{L_{II}}: \quad \sigma_X(L_{II}) &= \omega(L_{II})\{\sigma_I(L_{II}) + f(L_I, L_{II})\,\sigma_I(L_I)\} \\
\underline{L_{III}}: \quad \sigma_X(L_{III}) &= \omega(L_{III})\{\sigma_I(L_{III}) + f(L_{II}, L_{III})\,\sigma_I(L_{II}) \\
&+ [f(L_I, L_{III}) + f(L_I, L_{II})\,f(L_{II}, L_{III})]\,\sigma_I(L_I)\}
\end{aligned}$$

where ω is the fluorescence yield, f is the Coster-Kronig fraction, and S is the super Coster-Kronig fraction.

Figure 4.5 shows the dependence of the x-ray production cross sections for the five M subshells (dashed curves) and the total M-shell (solid curve) on the incident proton energy. Also shown are 2 sets of experimental data for the total M-shell cross section (symbols). The agreement between the calculated cross sections and experimental data is good, with typical differences again being a couple tens of percent.

Because of the unique dependence of the cross section for each shell on the incident proton energy, one can attempt to deduce the beam energy from measured line (or band) ratios. This is illustrated in Figs. 4.6 and 4.7, where 3 sets of line ratios between M- and L-shell lines are plotted as a function of the beam energy. Figure 4.6 shows results for protons ranging in energy from 0.1–1.0 MeV, while Fig. 4.7 shows results for higher beam energies. In principle, one can simply measure the line ratio and infer the beam energy. Although complications can arise from opacity effects (see below), non-monoenergetic beams, and some uncertainty in the cross sections, we feel the method has good potential for use in light ion beam experiments.

4.3. Opacity Effects

We have performed a series of CRE calculations to determine the plasma conditions at which one could expect line opacity effects to become important. Line self-attenuation can occur when the lower state in the x-ray transition becomes populated. For instance, the $M\alpha_1$ line is produced as a $4f_{7/2}$ electron drops down to fill a vacancy in the $3d_{5/2}$ subshell ($M_V \rightarrow N_{VII}$) (see, e.g., Cowan 1981). To determine the opacity, one needs to know the population of the N_{VII} state (i.e., the state with a vacancy in the $4f_{7/2}$ subshell). This state can be populated by 2 processes: proton-impact ionization and thermal collisions. As the target plasma temperature increases, the populations of

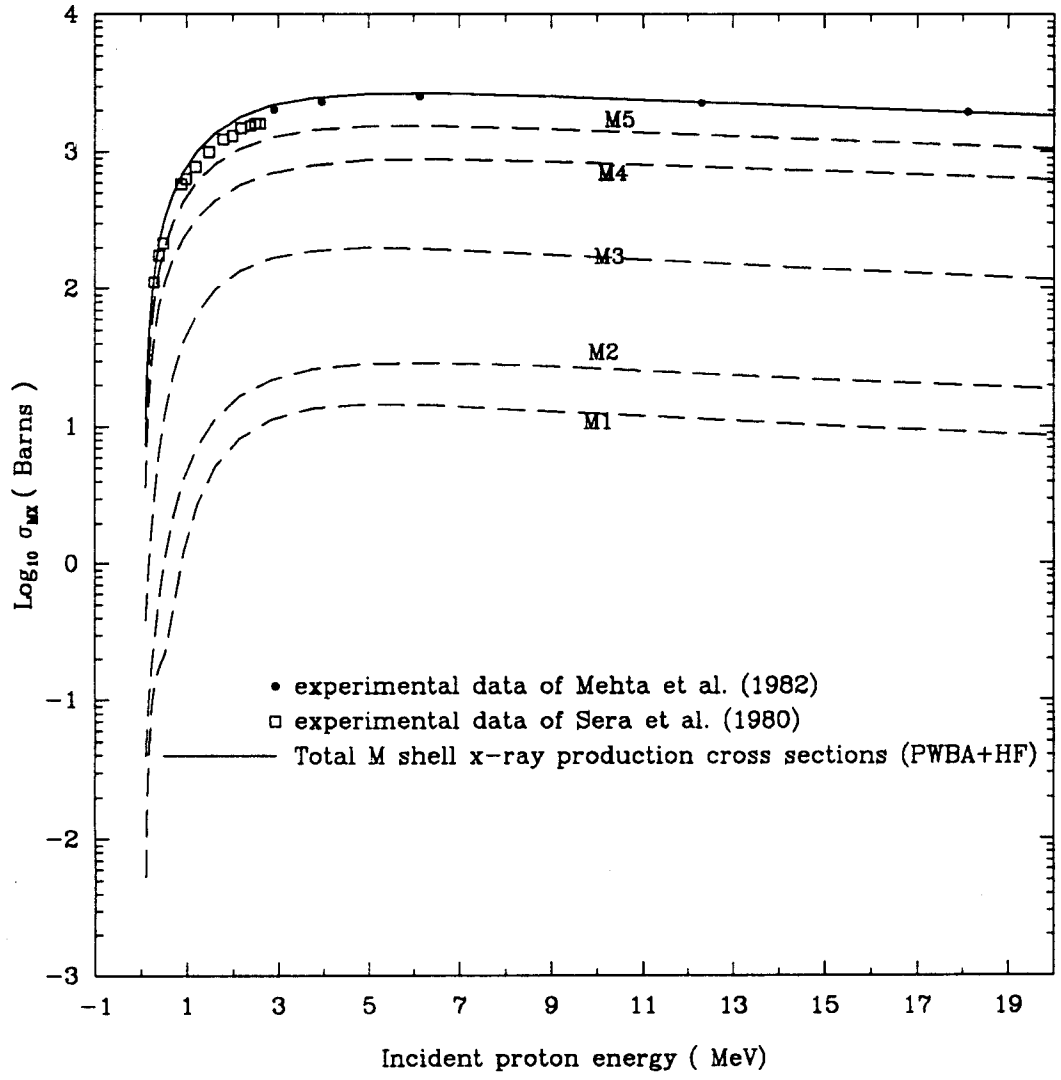

Figure 4.5. M-shell x-ray production cross sections for Au as a function of incident proton energy.

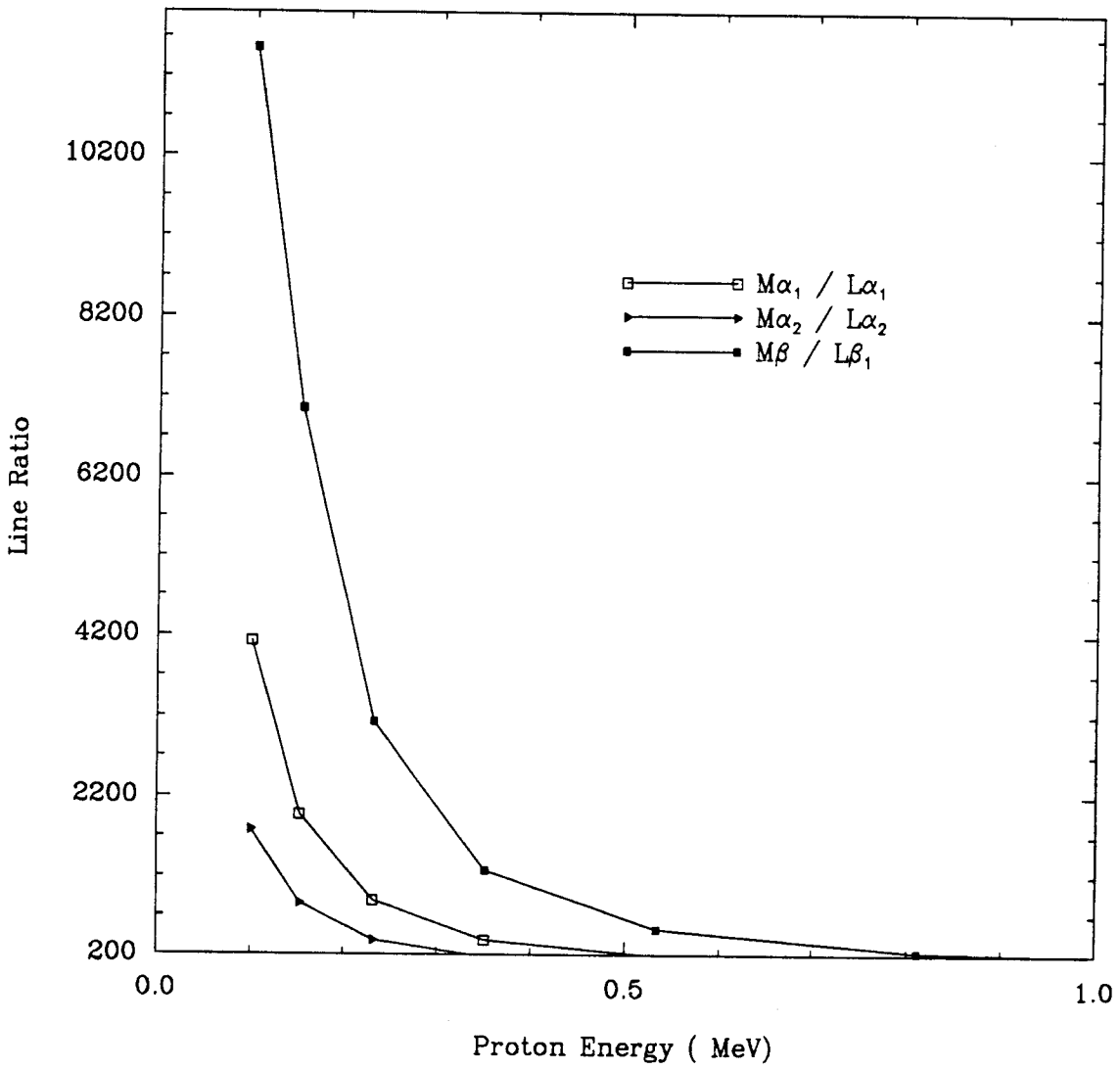

Figure 4.6. Dependence of $M\alpha_1/L\alpha_1$, $M\alpha_2/L\alpha_2$, and $M\beta/L\beta_1$ line ratios on incident proton beam energy.

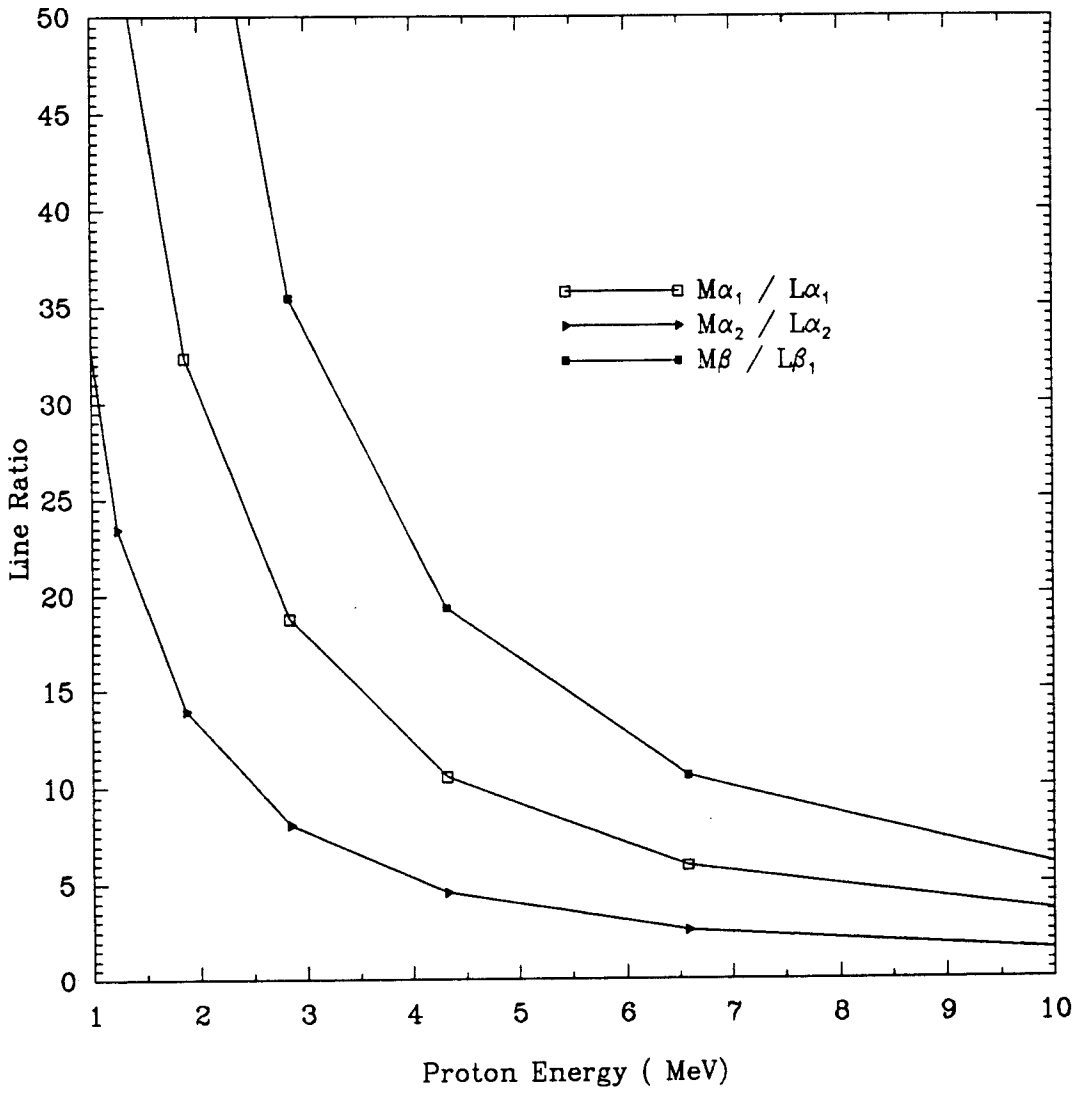

Figure 4.7. Same as Fig. 4.6, but over a larger range of proton energies.

these states increase due to thermal (electron-impact) excitations and ionizations. In this section, we address the following questions:

1. What are the line optical depths which result from beam-produced vacancies?
2. How does the line optical depth produced by thermal effects change with temperature?
3. Which lines are most likely to be influenced?

To determine when opacity effects become important we performed CRE calculations for the following conditions: $L = 10\,\mu$m, $n = 10^{-1}\,n_0$, and $T = 2$, 4, 8, 16, and 32 eV. The density and thickness correspond to a 1 μm-thick foil that has expanded by a factor of 10. The range of temperatures is typical of those attained in present-day light ion beam fusion experiments. In our CRE calculations, our atomic model consisted of 108 energy levels distributed over the lowest 6 ionization states of gold. In each calculation we assume a 1 MA/cm^2 current density (5 MeV protons, 5 TW/cm^2).

Preliminary results from our calculations are shown in Figs. 4.8 and 4.9. Figure 4.8 shows calculated line center optical depths for 3 M-shell lines as a function of the Au plasma temperature. The optical depth of the $M_V\,N_{III}$ line ($M\zeta_1$) is very small ($< 10^{-6}$) and shows little dependence on temperature. The fact that the curve is flat indicates that thermal effects are unimportant. At these temperatures, the N_{III} state, which has a vacancy in the $4p_{3/2}$ subshell, is being populated entirely by proton-impact ionizations. This is easily understood because the energy of the N_{III} state is 559 eV with respect to the ground state, whereas the maximum temperature in our calculations is 32 eV. On the other hand, the $M_V\,M_{III}(M\alpha_1)$ and $M_{IV}\,N_{VI}$ ($M\beta$) transitions show a strong dependence on temperature. This is because the N_{VI} and N_{VII} states have much lower energies

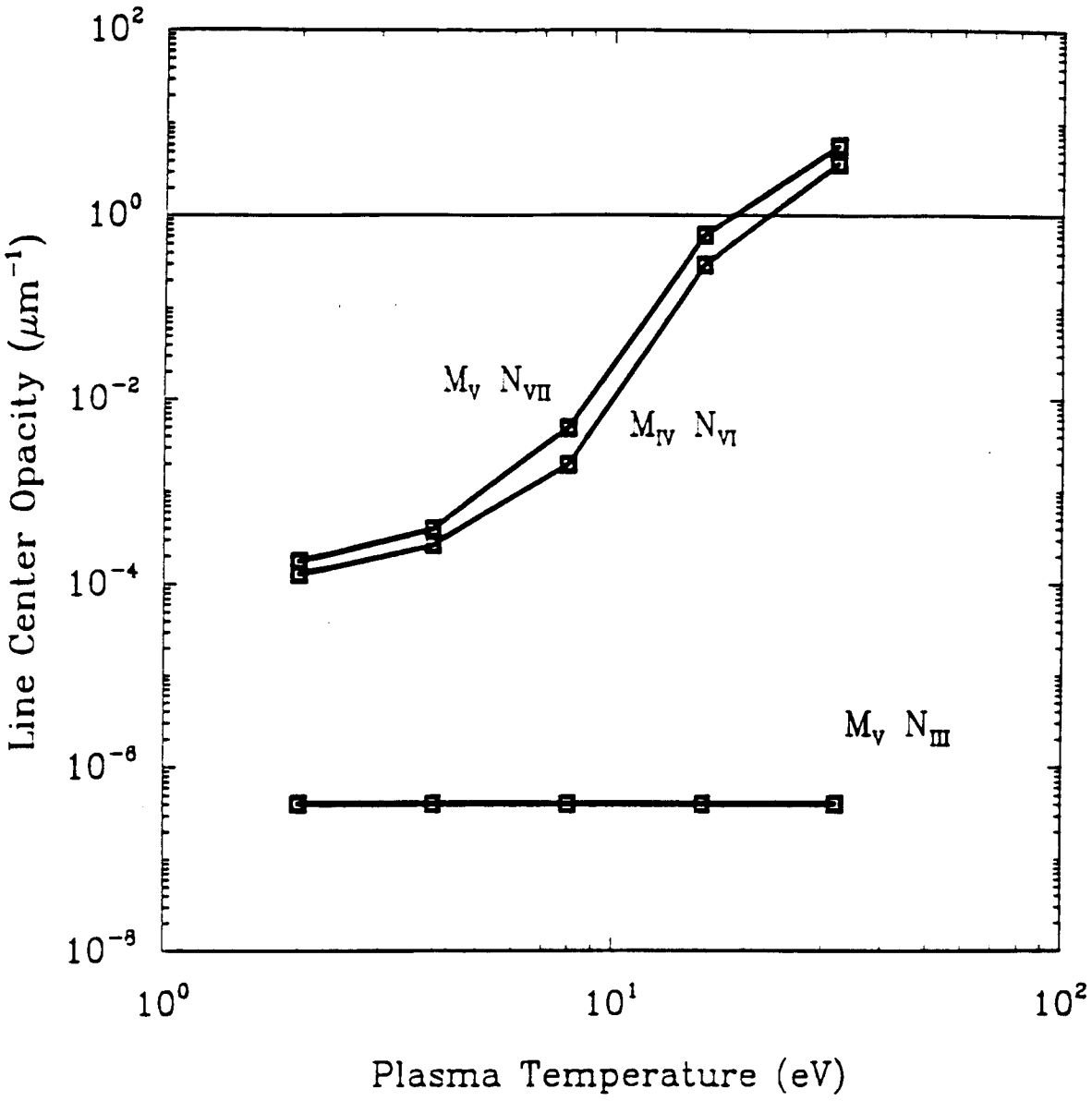

Figure 4.8. Dependence of line center optical depth of Au, $M\alpha_1$, M_β, and $M\zeta_1$ lines on plasma temperature. At $T \gtrsim 20$ eV, the $M\alpha$ and $M\beta$ lines become optically thick for micron-sized Au foils.

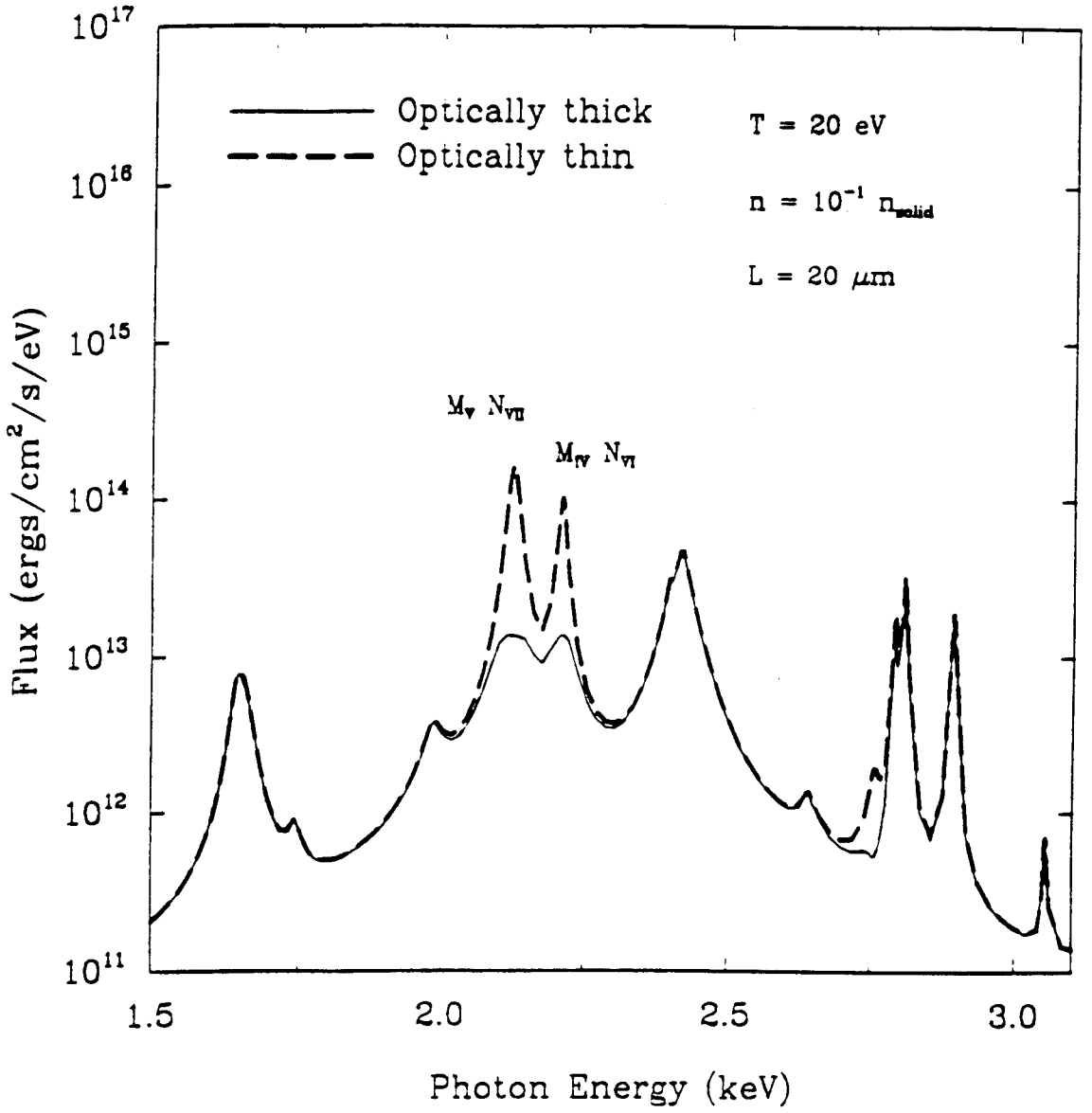

Figure 4.9. Calculated M-shell line spectrum for a proton beam-irradiated Au plasma with $T = 20$ eV, $n = 10^{-1}\, n_0$, and $L = 20$ μm. The dashed curve represents results in which attenuation effects were neglected.

with respect to ground — 92 and 88 eV, respectively. The optical depths resulting from proton-impact ionizations for both lines are quite small ($\sim 10^{-4}$). However, as the temperature rises above about 10 eV, the opacity increases rapidly due to thermal effects. Our calculations indicate that the line center optical depths of the $M\alpha_1$ and $M\beta$ lines exceed unity at temperatures $\gtrsim$ 20 eV.

The effect of the line opacity on the emitted spectrum is shown in Fig. 4.9, where the M-shell spectral flux has been computed for a 20 μm-thick plasma with $T = 20$ eV and $n = 10^{-1}\, n_0$. The two curves shown represent results from calculations in which line opacity effects are included (solid curve) and not included (dashed curve). Note the reduction in the flux from the strongest (i.e., $M\alpha$ and $M\beta$) lines. For these conditions we see that the line center flux from these lines is reduced by about one order of magnitude by line self-attenuation. Note, however, that the flux from the weaker lines is unaffected (with the exception of the $M_{III}\, O_V$ line at 2.76 keV).

The implications of these results for diagnosing beam energies from x-ray lines are significant. Inferring beam energies from M/L *band* intensity ratios will be inaccurate if μm-sized Au foils are heated to temperatures $\gtrsim$ 20 eV. This is illustrated in Fig. 4.10, where the M-band/L-band intensity ratio is plotted as a function of the beam energy. The solid curve includes the contribution from all M-shell lines, while the dashed and dot-dashed curves exclude the $M\alpha$ and $M\alpha + M\beta$ lines, respectively. Clearly, the $M\alpha$ and $M\beta$ lines represent the dominant contribution to the M-band intensity. At 1 MeV, the M-band intensity could be reduced by up to an order of magnitude if the $M\alpha$ and $M\beta$ lines are drastically attenuated.

There are at least 2 ways in which one can attempt to bypass these opacity problems. First, one could use a much thinner Au (or other high-Z material) diagnostic layer. From our preliminary calculations, we expect the maximum line center optical depths to

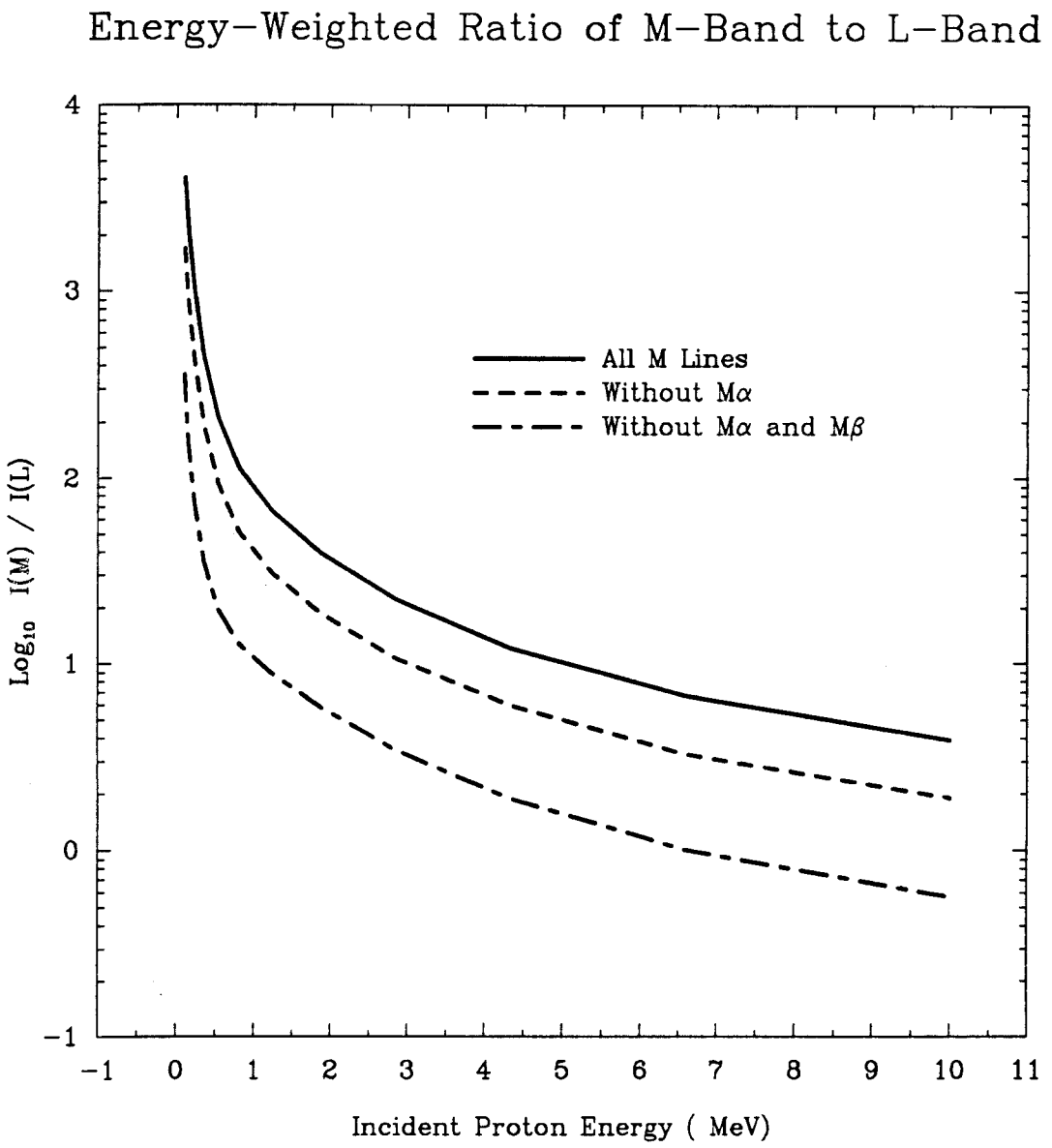

Figure 4.10. Dependence of M-band to L-band ratio for Au as a function of incident proton energy. The dashed curves show the significant contribution the $M\alpha$ and $M\beta$ lines make to the total M-band flux.

be $\sim 10^1$ for μm-sized foils. Thus, if a target could be fabricated with a Au coating of thickness $\sim 10^{-2}\,\mu$m ($\sim 10^2$ Å), opacity effects should be unimportant. Alternatively, if one could measure the flux from M lines that are not optically thick — such as with a spectrometer or with filtered broadband detectors — opacity effects would again become unimportant. A third alternative is to find a material which has the right combination of ionization cross sections and atomic properties that resonant self-absorption is unimportant over the temperature range of interest.

5. Diode Plasma Calculations

We have performed a series of calculations to provide theoretical support for KALIF diode plasma experiments carried out by H. Laqua and H. Bluhm. The purpose of the calculations is to determine whether spectral lines used to diagnose plasma conditions are optically thick over the range of conditions expected in the experiments. If a line is optically thick, the plasma conditions deduced from its shape or its intensity relative to other lines can be inaccurate. This is because line self-absorption effects will both broaden the observed line profile and reduce the overall line intensity.

The plasma in the diode region is assumed to have the following characteristics:

- ion density between 10^{14} and 10^{18} cm^{-3};
- electron temperature between 0.75 and 8 eV;
- composition: 90% H, 5% C, 5% Ti; and
- dimensions: 0.7 cm $\times$ 2.5 cm $\times$ 7.0 cm (7.0 cm along line-of-sight to detector).

In all of our calculations, we model the plasma as a planar slab (1-D, infinitely extending in the 2nd and 3rd dimension) with a width of $L = 0.7$ cm. This represents the shortest pathlength for escape of photons and therefore is the most suitable for modelling photoexcitation effects. Optical depths along the detector line-of-sight are then estimated by multiplying the computed optical depths by a factor of 10 (= 7 cm/0.7 cm).

Since hydrogen is the most abundant plasma component, we have first performed a series of calculations for pure H. In addition to computing the optical depths, we performed two additional sets of calculations: one to benchmark our ionization balance results with the recently published results of Mihalas et al. (1990); the second to assess

the effects of the radiation field on the atomic level populations. We then performed calculations for binary mixtures of H/C and H/Ti. We performed two-component plasma calculations rather than three component calculations in order to reduce the total number of levels in a calculation. This enabled us to run the calculations locally on a workstation.

The properties of our atomic models for H, C, and Ti are listed in Tables 5.1 through 5.3. Shown are the level index, ionization stage, configuration, term symbol, statistical weight, and energy ($E = 0$ corresponds to the ground state of the neutral atom). Energies for levels involved in diagnostic lines of interest were selected from National Bureau of Standards tables (Moore 1965, Weise and Musgrove 1989). Other level energies were obtained from Hartree-Fock calculations. For hydrogen, we considered a total of 7 levels (6 for H I, 1 for H II). We considered 24 levels for carbon (3 for C I, 17 for C II, 3 for C III, and 1 for C IV) and 39 levels for titanium (16 for Ti I, 19 for Ti II, 3 for Ti III, and 1 for Ti IV). Relatively detailed atomic models including fine structure were used for C II, Ti I, and Ti II because of the interest in examining the properties of specific lines.

The transitions of interest were specified by H. Laqua and are listed in Table 5.4. Not included are 2 lines (Ti I λ3904 and Ti II λ3343) which we could not identify in the tables of Weise and Musgrove (1989). There is also some ambiguity in the two other Ti I lines because there are nearby transitions at 3982.48 Å and 5000.99 Å. Because these lines are weaker, we have chosen to examine the lines listed in Table 5.4.

As a quick check of our ionization model, we have compared some LTE results from our pure H calculations with those of Mihalas et al. (1990). The comparison is a little difficult because the calculations of Mihalas are for a solar composition plasma (roughly 90% H, 10% He, and trace amounts of higher-Z species) while our calculations were for pure hydrogen. Nevertheless, we felt it worthwhile to check for qualitative agreement.

Table 5.1. Hydrogen Energy Levels

Level Index	Ionization Stage	Configuration	Term	Statistical Weight	Energy (eV)
1	1	1s(1)	hy	2.	0.0000
2	1	2s(1)	hy	8.	10.2043
3	1	3s(1)	hy	18.	12.0940
4	1	4s(1)	hy	32.	12.7554
5	1	5s(1)	hy	50.	13.0616
6	1	6s(1)	hy	72.	13.2279
7	2		av	1.	13.6058

Table 5.2. Carbon Energy Levels

Level Index	Ionization Stage	Configuration	Term	Statistical Weight	Energy (eV)
1	1	1s(2)2s(2)2p(2)	1S	1.	0.0000
2	1	1s(2)2s(2)2p(1)3s(1)	1P	3.	3.6191
3	1	1s(2)2s(1)2p(3)	1P	3.	11.8050
4	2	1s(2)2s(2)2p(1)	$2P_{1/2}$	2.	7.0035
5	2	1s(2)2s(2)2p(1)	$2P_{3/2}$	4.	7.0114
6	2	1s(2)2s(1)2p(2)	$4P_{1/2}$	2.	12.3353
7	2	1s(2)2s(1)2p(2)	$2D_{5/2}$	6.	16.4176
8	2	1s(2)2s(1)2p(2)	$2S_{1/2}$	2.	18.9673
9	2	1s(2)2s(1)2p(2)	$2P_{1/2}$	2.	20.7195
10	2	1s(2)2s(2)3s(1)	$2S_{1/2}$	2.	21.4526
11	2	1s(2)2s(2)3p(1)	$2P_{1/2}$	2.	23.3353
12	2	1s(2)2s(2)3p(1)	$2P_{3/2}$	4.	23.3367
13	2	1s(2)2s(2)3d(1)	$2D_{3/2}$	4.	25.0494
14	2	1s(2)2s(2)3d(1)	$2D_{5/2}$	6.	25.0497
15	2	1s(2)2s(2)4s(1)	$2S_{1/2}$	2.	26.4981
16	2	1s(2)2s(2)4p(1)	$2P_{1/2}$	2.	27.1534
17	2	1s(2)2s(2)4p(1)	$2P_{3/2}$	4.	27.1542
18	2	1s(2)2s(2)4d(1)	$2D_{3/2}$	4.	27.8484
19	2	1s(2)2s(2)4d(1)	$2D_{5/2}$	6.	27.8484
20	2	1s(2)2s(2)4f(1)	$2F_{5/2}$	6.	27.9542
21	3	1s(2)2s(2)	1S	1.	31.0516
22	3	1s(2)2s(1)2p(1)	1P	3.	43.2236
23	3	1s(2)2s(1)3s(1)	1S	1.	58.8661
24	4	1s(2)2s(1)	2S	2.	76.8333

Table 5.3. Titanium Energy Levels

Level Index	Ionization Stage	Configuration	Term	Statistical Weight	Energy (eV)
1	1	[Ar]3d(2)4s(2)	$3F_2$	5.	0.0000
2	1	[Ar]3d(2)4s(2)	$3F_3$	7.	0.0211
3	1	[Ar]3d(2)4s(2)	$3F_4$	9.	0.0479
4	1	[Ar]3d(3)4s(1)	$5F_1$	3.	0.8129
5	1	[Ar]3d(3)4s(1)	$5F_2$	5.	0.8181
6	1	[Ar]3d(3)4s(1)	$5F_3$	7.	0.8258
7	1	[Ar]3d(2)4s(1)4p(1)	$3F_2$	5.	3.1129
8	1	[Ar]3d(2)4s(1)4p(1)	$3F_3$	7.	3.1278
9	1	[Ar]3d(2)4s(1)4p(1)	$5D_0$	25.	3.1746
10	1	[Ar]3d(2)4s(1)4p(1)	$5D_1$	3.	3.1784
11	1	[Ar]3d(2)4s(1)4p(1)	$5D_2$	5.	3.1864
12	1	[Ar]3d(2)4s(1)4p(1)	$5D_3$	7.	3.1986
13	1	[Ar]3d(2)4s(1)4p(1)	$5D_4$	9.	3.2145
14	1	[Ar]3d(3)4p(1)	$5G_2$	5.	3.2849
15	1	[Ar]3d(3)4p(1)	$5G_3$	7.	3.2936
16	1	[Ar]3d(3)4p(1)	$5G_4$	9.	3.3051
17	2	[Ar]3d(2)4s(1)	$4F_{3/2}$	4.	5.5129
18	2	[Ar]3d(2)4s(1)	$4F_{5/2}$	6.	5.5246
19	2	[Ar]3d(2)4s(1)	$4F_{7/2}$	8.	5.5446
20	2	[Ar]3d(2)4s(1)	$4F_{9/2}$	10.	5.5617
21	2	[Ar]3d(3)	$4F_{3/2}$	4.	5.6255
22	2	[Ar]3d(3)	$4F_{5/2}$	6.	5.6349
23	2	[Ar]3d(2)4s(1)	$2G_{9/2}$	10.	7.4046
24	2	[Ar]3d(2)4s(1)	$2G_{7/2}$	8.	7.4057
25	2	[Ar]3d(2)4p(1)	$4G_{5/2}$	6.	9.1760
26	2	[Ar]3d(2)4p(1)	$4G_{7/2}$	8.	9.1996
27	2	[Ar]3d(2)4p(1)	$4G_{9/2}$	10.	9.2285
28	2	[Ar]3d(2)4p(1)	$4G_{11/2}$	12.	9.2624
29	2	[Ar]3d(2)4p(1)	$4F_{3/2}$	4.	9.3362
30	2	[Ar]3d(2)4p(1)	$4F_{5/2}$	6.	9.3513
31	2	[Ar]3d(2)4p(1)	$4F_{7/2}$	8.	9.3706
32	2	[Ar]3d(2)4p(1)	$2G_{7/2}$	8.	10.9353
33	2	[Ar]3d(2)4p(1)	$2G_{9/2}$	10.	10.9411
34	2	[Ar]3d(2)4p(1)	$2H_{9/2}$	10.	11.1757
35	2	[Ar]3d(2)4p(1)	$2H_{11/2}$	12.	11.2049
36	3	[Ar]3d(2)	av	45.	19.4104
37	3	[Ar]3d(1)4s(1)	av	20.	23.2540
38	3	[Ar]3d(1)4p(1)	av	60.	27.8846
39	4	[Ar]3d(1)	av	10.	45.0775

Table 5.4. Diagnostic Lines for H, C, and Ti

Line	Wavelength (Å)	Upper Level*	Lower Level*
H_α	6562.79[a]	3	2
H_β	4861.33[a]	4	2
H_γ	4340.47[a]	5	2
H_δ	4101.74[a]	6	2
C II	4267.26[b]	20	14
C II	4267.00[b]	20	13
C II	6578.05[b]	12	10
C II	6582.88[b]	11	10
C II	7236.42[b]	13	11
C II	7231.32[b]	13	12
Ti I	3981.76[c]	7	1
Ti I	4999.50[c]	16	6
Ti II	3287.66[c]	34	24
Ti II	3504.90[c]	33	23
Ti II	3510.86[c]	32	24
Ti II	3361.23[c]	27	19
Ti II	3383.77[c]	25	17

*Indices correspond to those in Tables 5.1-5.3.
[a]Herzberg (1944).
[b]Moore (1965).
[c]Weise and Musgrove (1989).

Table 5.5. Comparison of Ionization Balance Results for Hydrogen

	Our Results		Mihalas et al. (1990)	
T(k)	f(H I)	f(H II)	f(H I)	f(H II)
10^4	.972	.028	.974	.028
$10^{4.5}$	8.4 e-3	.9916	6.7 e-3	.9933
10^5	6.0 e-4	.9994	3.0 e-4	.9997
10^6	1.6 e-5	1.000	7.7 e-6	1.000

The results, compared in Table 5.5, correspond to a solar composition mass density of $\rho = 10^{-6}$ g/cm^3 for Mihalas et al. and a hydrogen particle density of 4.25×10^{17} cm^{-3} for our calculations. The agreement between the 2 calculations is reasonably good. However, at high temperatures our neutral hydrogen fraction is about a factor of 2 higher. We feel this difference is likely due to the number of levels used in our calculations, although it is also possible that differences arise due to the different plasma compositions. The results in Table 5.5 were obtained using 6 H I levels ($n = 1$ through $n = 6$). To examine the sensitivity to the atomic level structure, we varied n_{max} for the case with $T = 10^{4.5}$ and obtained the following results:

n_{max}	f(H I)	f(H II)
6	6×10^{-4}	.9994
5	4×10^{-4}	.9996
4	2×10^{-4}	.9998
3	1×10^{-4}	.9999

By comparison the result of Mihalas et al. is f(H I) = 3×10^{-4}. Clearly, our results are somewhat sensitive to the number of levels used (for a discussion of this effect, see Hummer and Mihalas 1988). The relative uncertainty in the minor species population, H I, is fairly large (a factor of 6 between $n_{max} = 3$ and $n_{max} = 6$). However, the fractional

error in the major species H II is very small. In fact, we have examined the sensitivity of the optical depths for the H_α through H_δ lines on n_{max} at $T = 1$ eV and $n = 10^{17}$ cm^{-3}, i.e., conditions for which H I is the major species. We find that the computed optical depths differed from the $n_{max} = 6$ values by less than 7% as n_{max} was varied between 4 and 9. We therefore conclude that our ionization balance model is reasonably accurate and that the number of levels in our atomic models is sufficiently large that the errors introduced by this effect in computing the optical depths are minor.

We have also examined the effects of the radiation field (i.e., photoexcitations and photoionizations) on the state of the plasma and the optical depths of the Balmer lines. To do this, we performed calculations for 2 cases: one in which radiation-induced transitions were included and one in which they were neglected. In each case the conditions were $T = 1$ eV, $n = 10^{18}$ cm^{-3}, and $L = 0.7$ cm. The populations for the $n =$ 1, 2, and 3 states are plotted in Figure 5.1 as a function of position. Note that without radiation effects included, the $n = 2$ and $n = 3$ state populations are reduced by 3 to 4 orders of magnitude. This is especially important for the Balmer line optical depths because of their dependence on the lower level ($n = 2$) population. For comparison, the computed LTE populations are: 0.941 ($n = 1$), 1.4×10^{-4} ($n = 2$), and 4.7×10^{-5} (n = 3). These values are about 20% to 40% lower than those computed at the midplane in the calculations with radiation effects. Thus an LTE model provides a much better estimate of the level populations for these conditions. This, however, will not be the case for the relatively low density plasmas because in this case the radiation can escape the plasma. The computed optical depths with and without photopumping are as follows:

Line	τ (with photopumping)	τ (no photopumping)
H_α	6.02	0.013
H_β	0.46	0.002
H_γ	0.072	5×10^{-4}
H_δ	0.017	2×10^{-4}

This shows that photoexcitations significantly affect the state of the plasma in the diode region.

We present our results for line optical depths in both graphical and tabular form to provide the greatest flexibility for use. Results for pure hydrogen plasmas are presented in Table 5.6 and Figures 5.2 - 5.5. *The optical depths correspond to the detector line-of-sight where the path length is assumed to be 7 cm.* The optical depths are those at line center computed using a Voigt line profile which includes the effects of Stark, Doppler, and natural broadening.

The hydrogen lines show the largest optical depths at temperatures of about 1 to 2 eV. At lower temperatures, the $n = 2$ state population decreases as most atoms are in the ground state. At relatively high temperatures, hydrogen becomes ionized and the H I line optical depths decrease. If one uses the criterion that τ must be less than 10^{-1} ($e^{-0.1} = .905$), then at all temperatures H_α will be optically thin for $n \lesssim 3 \times 10^{15}$ cm^{-3}. Similarly, the density must be below 1×10^{16}, 5×10^{16}, and 1×10^{17} cm^{-3} for the H_β, H_γ, and H_δ lines. More stringent criteria of course require even lower densities.

Results for carbon lines are shown in Figure 5.6 and Table 5.7, while those for the Ti lines are shown in Figures 5.7-5.9 and Table 5.8. The C II lines generally have relatively low optical depths because the lines of interest involved transitions between relatively highly excited states. On the other hand, the Ti II lines, which involve transitions between low lying states, can have very large optical depths. For the thickest line ($\lambda =$

Table 5.6. Hydrogen Line Center Optical Depths

T	n	n_e	Line Center Optical Depth			
(eV)	(cm^{-3})	(cm^{-3})	H_α	H_β	H_γ	H_δ
0.75	10^{18}	2.6e15	1.6e+1	1.9e+0	4.2e-1	1.2e-1
0.75	10^{17}	2.5e14	6.2e-1	8.7e-2	2.7e-2	1.1e-2
0.75	10^{16}	9.1e13	4.5e-3	6.8e-4	2.2e-4	9.7e-5
0.75	10^{15}	7.4e12	3.0e-6	0	0	0
0.75	10^{14}	1.6e12	0	0	0	0
1	10^{18}	4.6e16	6.0e+1	4.6e+0	7.2e-1	1.7e-1
1	10^{17}	4.9e15	1.5e+1	1.6e+0	3.2e-1	8.6e-2
1	10^{16}	1.6e14	1.3e-1	1.8e-2	5.7e-3	2.5e-3
1	10^{15}	1.0e13	6.7e-5	9.8e-6	3.2e-6	1.5e-6
1	10^{14}	1.9e12	0	0	0	0
2	10^{18}	8.9e17	5.1e+1	4.2e+0	6.9e-1	1.7e-1
2	10^{17}	9.6e16	7.4e+0	6.0e-1	9.7e-2	2.4e-2
2	10^{16}	9.3e15	1.1e+0	1.2e-1	2.4e-2	6.6e-3
2	10^{15}	8.6e14	6.3e-3	8.6e-4	2.6e-4	1.1e-4
2	10^{14}	9.1e13	9.8e-6	1.2e-6	0	0
4	10^{18}	9.93e17	7.6e+0	6.6e-1	1.1e-1	2.8e-2
4	10^{17}	9.98e16	8.2e-1	7.5e-2	1.3e-2	3.2e-3
4	10^{16}	9.98e15	9.5e-3	1.3e-3	3.5e-4	1.1e-4
4	10^{15}	9.98e14	3.4e-5	0	0	0
4	10^{14}	9.98e13	0	0	0	0
8	10^{18}	9.98e17	1.4e+0	1.2e-1	2.1e-2	5.3e-3
8	10^{17}	1.00e17	5.4e-2	6.9e-3	1.3e-3	3.6e-4
8	10^{16}	1.00e16	0	0	0	0
8	10^{15}	1.00e15	0	0	0	0
8	10^{14}	1.00e14	0	0	0	0

Table 5.7. Carbon Line Center Optical Depths

T	n	n_e	Line Center Optical Depth					
(eV)	(cm^{-3})	(cm^{-3})	4267.00	4267.26	6578.05	6582.88	7231.32	7236.42
0.75	10^{18}	4.9e16	0	0	3.9e-5	1.9e-5	7.0e-7	2.9e-6
1	10^{18}	7.9e16	8.0e-5	6.2e-6	3.3e-3	1.6e-3	1.1e-4	4.5e-4
1	10^{17}	9.3e15	5.9e-5	4.5e-6	1.9e-3	9.3e-4	6.7e-5	2.8e-4
2	10^{18}	8.9e17	5.7e-2	4.4e-3	3.6e-1	1.8e-1	3.0e-2	1.3e-1
2	10^{17}	9.7e16	4.4e-2	3.4e-3	2.8e-1	1.4e-1	2.3e-2	9.7e-2
2	10^{16}	9.4e15	1.5e-2	1.3e-3	6.4e-2	3.3e-2	6.1e-3	2.4e-2
2	10^{15}	8.7e14	2.8e-4	2.8e-5	1.0e-3	5.2e-4	9.6e-5	3.7e-4
3	10^{18}	1.01e18	3.4e-1	2.6e-2	1.2e+0	5.8e-1	1.3e-1	5.5e-1
3	10^{17}	1.04e17	6.8e-2	5.4e-3	2.3e-1	1.2e-1	2.7e-2	1.1e-1
3	10^{16}	1.03e16	2.0e-2	1.8e-3	4.5e-2	2.4e-2	5.9e-3	2.3e-2
4	10^{18}	1.05e18	1.3e-1	9.9e-3	3.2e-1	1.6e-1	4.2e-2	1.7e-1
4	10^{17}	1.07e17	1.6e-2	1.3e-3	4.1e-2	2.1e-2	5.4e-3	2.2e-2
4	10^{16}	1.07e16	6.5e-3	5.4e-4	1.1e-2	5.3e-3	1.5e-3	5.9e-3
8	10^{18}	1.10e18	8.1e-5	6.3e-6	1.2e-4	6.1e-5	2.0e-5	8.2e-5
8	10^{17}	1.10e17	1.4e-5	1.2e-6	1.9e-5	9.8e-6	3.2e-6	1.3e-5
8	10^{16}	1.10e16	1.3e-5	1.0e-6	1.1e-5	5.3e-6	1.7e-6	7.5e-6

Table 5.8. Titanium Line Center Optical Depths

T	n	n_e	Line Center Optical Depth						
(eV)	(cm^{-3})	(cm^{-3})	3981.76	4999.50	3287.66	3504.90	3510.86	3361.23	3383.77
0.75	10^{18}	5.0e16	3.2e+1	4.8e+1	9.0e+2	8.7e+2	6.8e+2	9.9e+3	3.5e+3
0.75	10^{17}	5.2e15	2.0e+0	3.2e+0	4.5e+2	4.5e+2	3.5e+2	4.9e+3	2.2e+3
0.75	10^{16}	5.6e14	6.9e-2	1.1e-1	6.2e+1	6.4e+1	4.9e+1	6.8e+2	3.5e+2
0.75	10^{15}	6.1e13	4.9e-3	8.3e-3	5.8e+0	6.1e+0	4.6e+0	6.4e+1	3.4e+1
0.75	10^{14}	6.6e12	5.3e-4	9.0e-4	5.8e-1	5.9e-1	4.6e-1	6.3e+0	3.3e+0
1	10^{18}	8.2e16	3.4e+0	6.5e+0	1.1e+3	1.0e+3	7.8e+2	6.2e+3	2.2e+3
1	10^{17}	1.1e16	2.4e-1	4.8e-1	4.2e+2	4.1e+2	3.2e+2	2.5e+3	1.0e+3
1	10^{16}	8.7e14	1.3e-2	2.7e-2	5.6e+1	5.9e+1	4.4e+1	3.4e+2	1.7e+2
1	10^{15}	7.1e13	2.2e-3	4.7e-3	7.2e+0	7.7e+0	5.7e+0	4.2e+1	2.2e+1
1	10^{14}	7.1e12	3.7e-4	8.3e-4	8.9e-1	9.1e-1	7.0e-1	5.2e+0	2.7e+0
2	10^{18}	9.4e17	4.1e-3	1.1e-2	1.4e+1	1.3e+1	1.0e+1	3.2e+1	1.1e+1
2	10^{17}	1.01e17	6.1e-5	1.8e-4	1.7e+0	1.6e+0	1.2e+0	3.9e+0	1.4e+0
2	10^{16}	9.8e15	1.7e-6	6.2e-6	2.0e-1	1.9e-1	1.5e-1	4.4e-1	2.0e-1
2	10^{15}	9.2e14	1.7e-7	7.0e-7	2.7e-2	2.7e-2	2.1e-2	6.0e-2	3.0e-2
2	10^{14}	9.6e13	0 2.5e-7	6.0e-3	6.1e-3	4.7e-3	1.3e-2	6.5e-3	
4	10^{18}	1.09e18	4.4e-7	1.5e-6	2.3e-2	2.1e-2	1.6e-2	3.3e-2	1.1e-2
4	10^{17}	1.10e17	0	0	1.6e-3	1.4e-3	1.1e-3	2.2e-3	7.9e-4
4	10^{16}	1.10e16	0	0	3.0e-4	2.8e-4	2.2e-4	3.9e-4	1.8e-4
8	10^{18}	1.10e18	0	0	3.7e-5	3.2e-5	2.6e-5	4.3e-5	1.5e-5

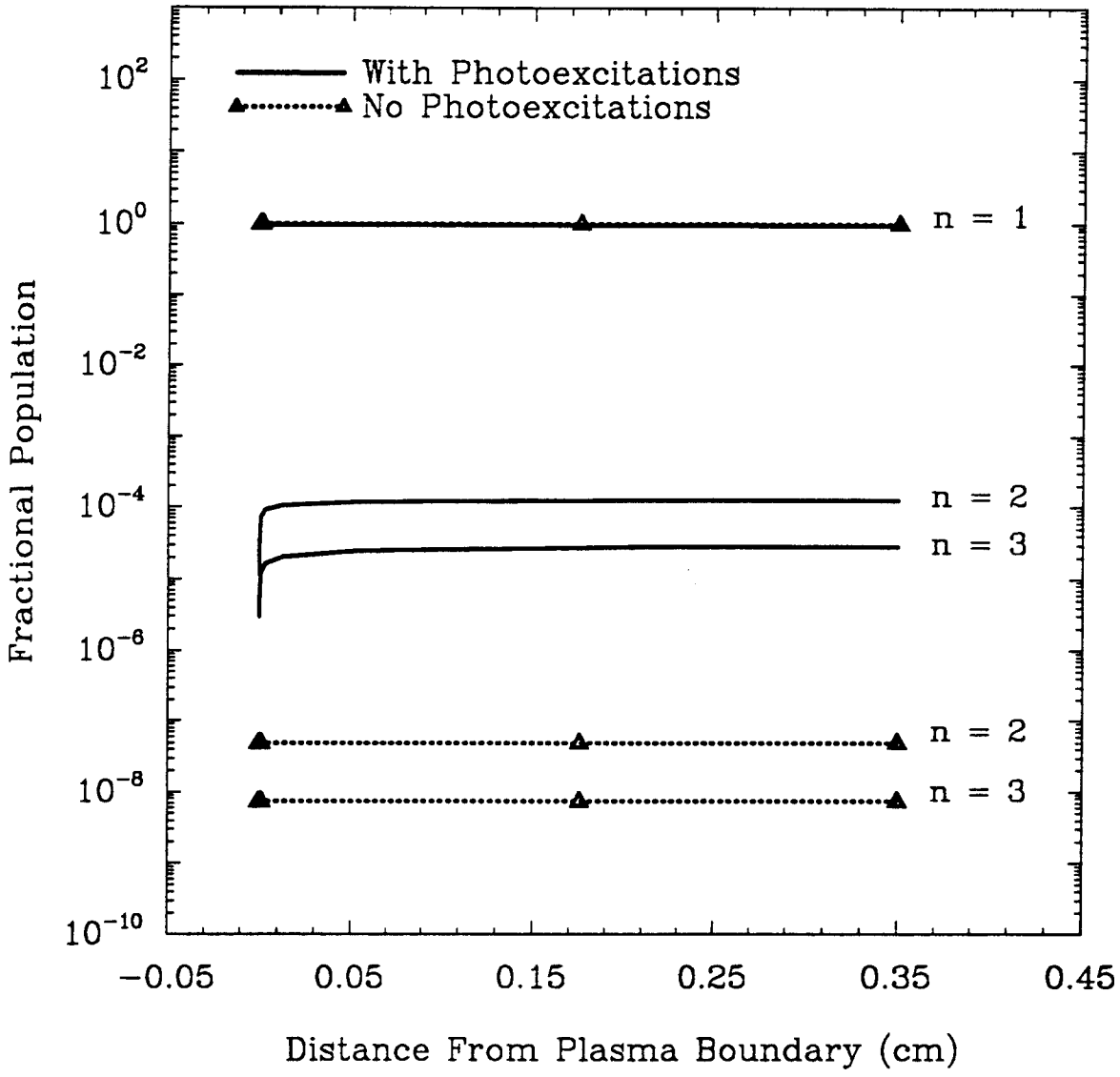

Figure 5.1. Fractional populations of the ground state and first 2 excited states of neutral hydrogen as a function of position in a planar plasma with $T = 1$ eV, $n = 10^{18}$ cm^{-3}, and $L = 0.7$ cm.

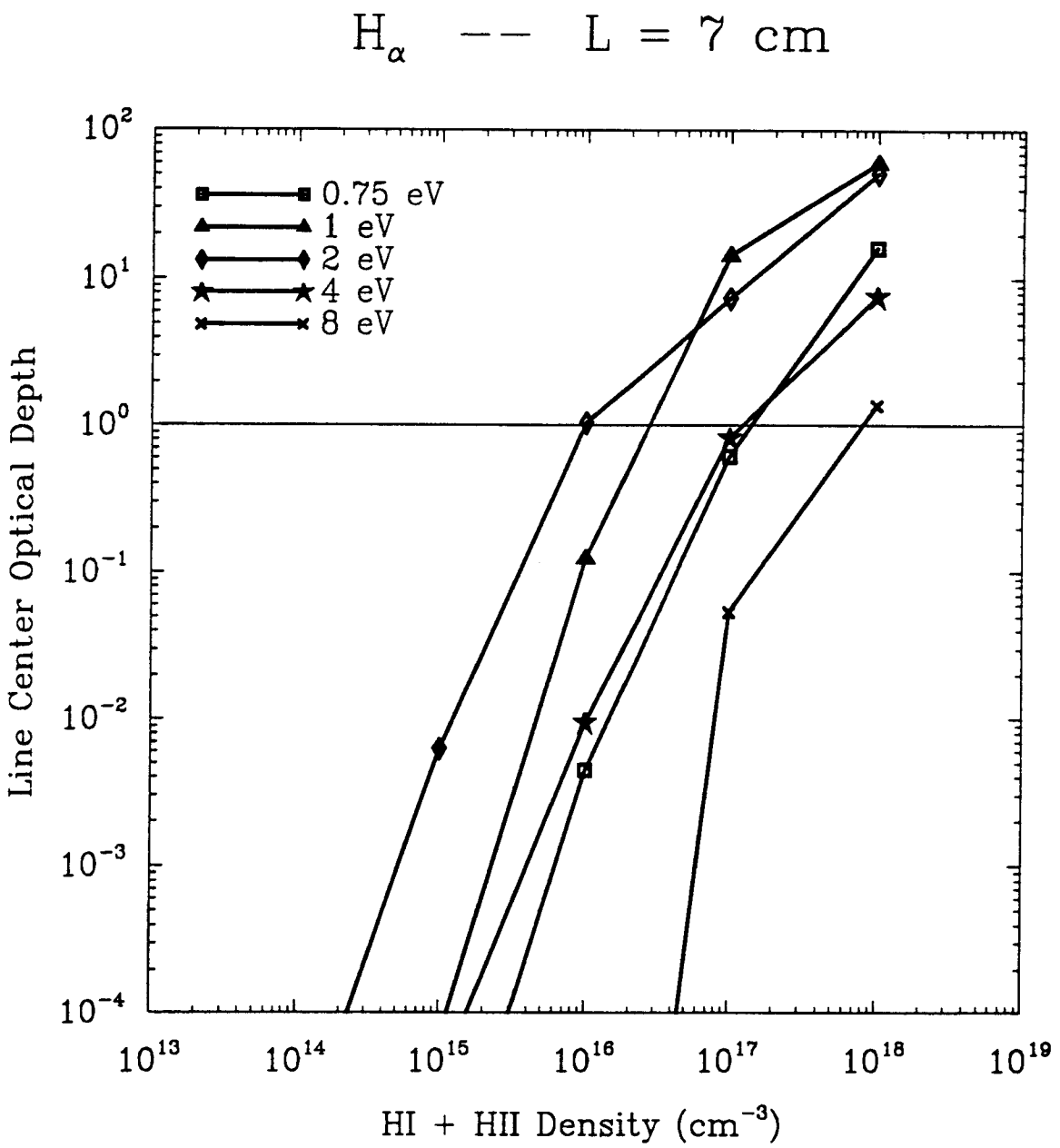

Figure 5.2. H_α line center optical depth as a function of hydrogen number density. The optical depths correspond to a line-of-sight distance of 7 cm. The horizontal line corresponds to an optical depth of 1.

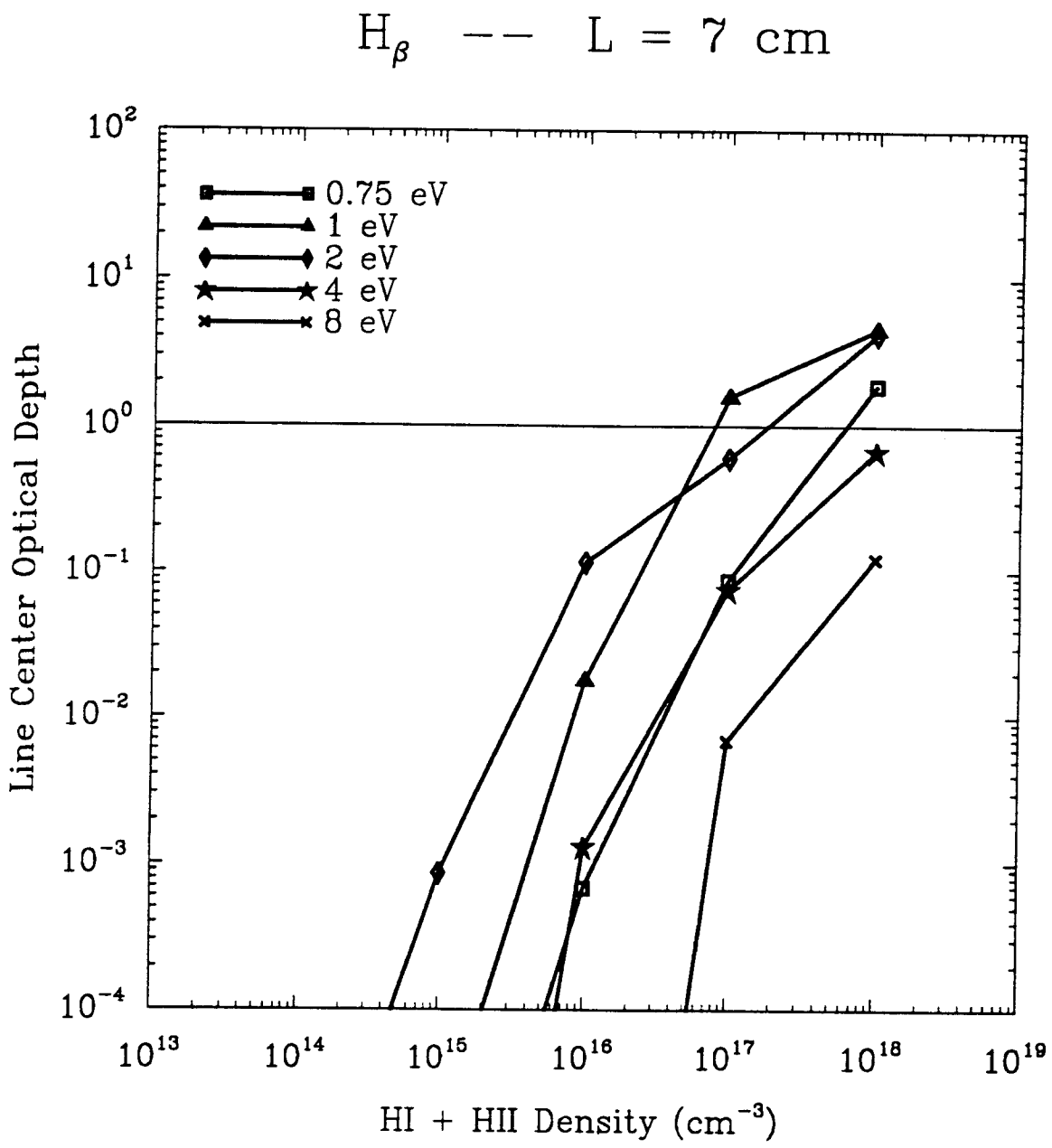

Figure 5.3. H_β line center optical depth as a function of hydrogen number density. The optical depths correspond to a line-of-sight distance of 7 cm. The horizontal line corresponds to an optical depth of 1.

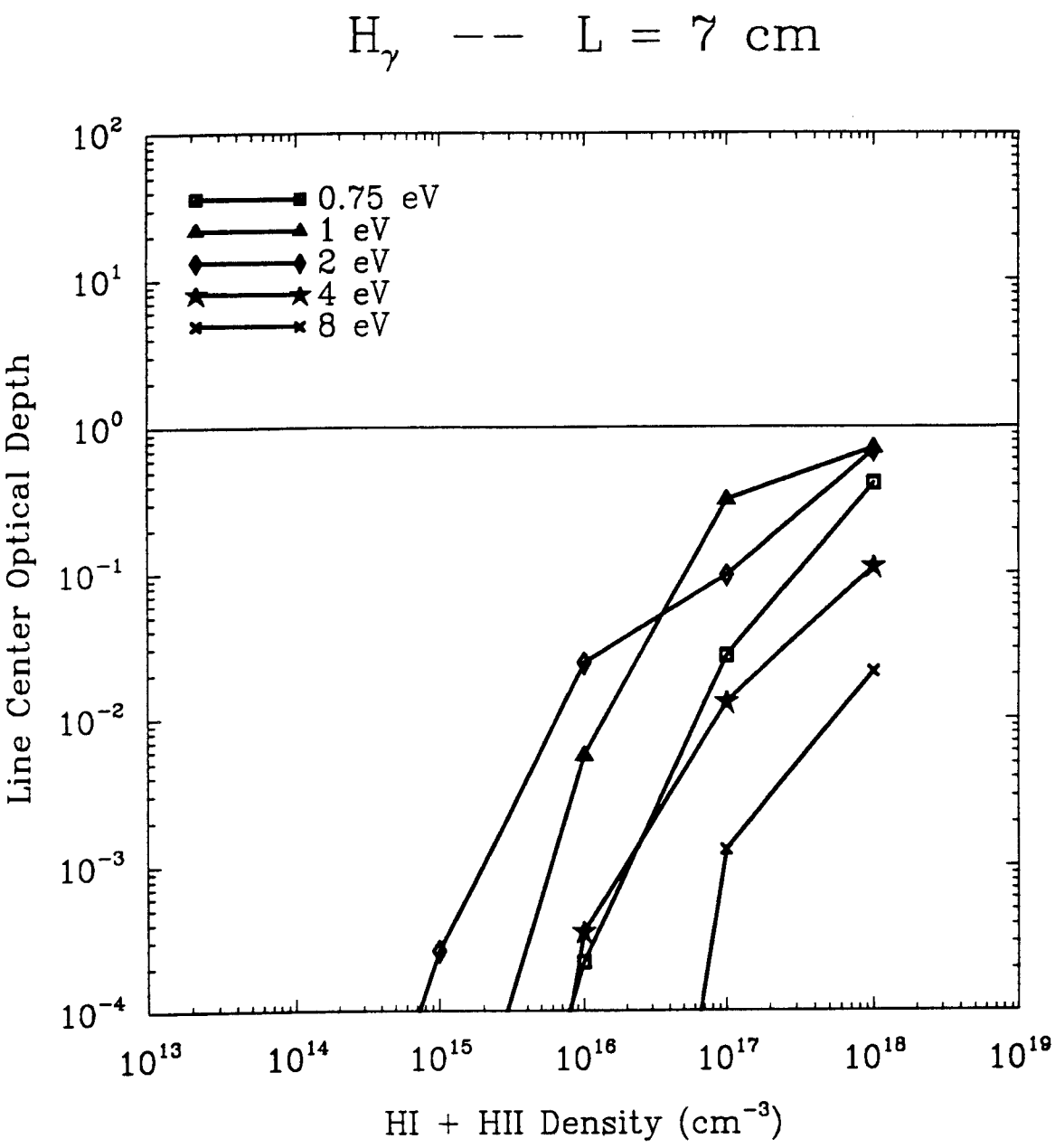

Figure 5.4. H_γ line center optical depth as a function of hydrogen number density. The optical depths correspond to a line-of-sight distance of 7 cm. The horizontal line corresponds to an optical depth of 1.

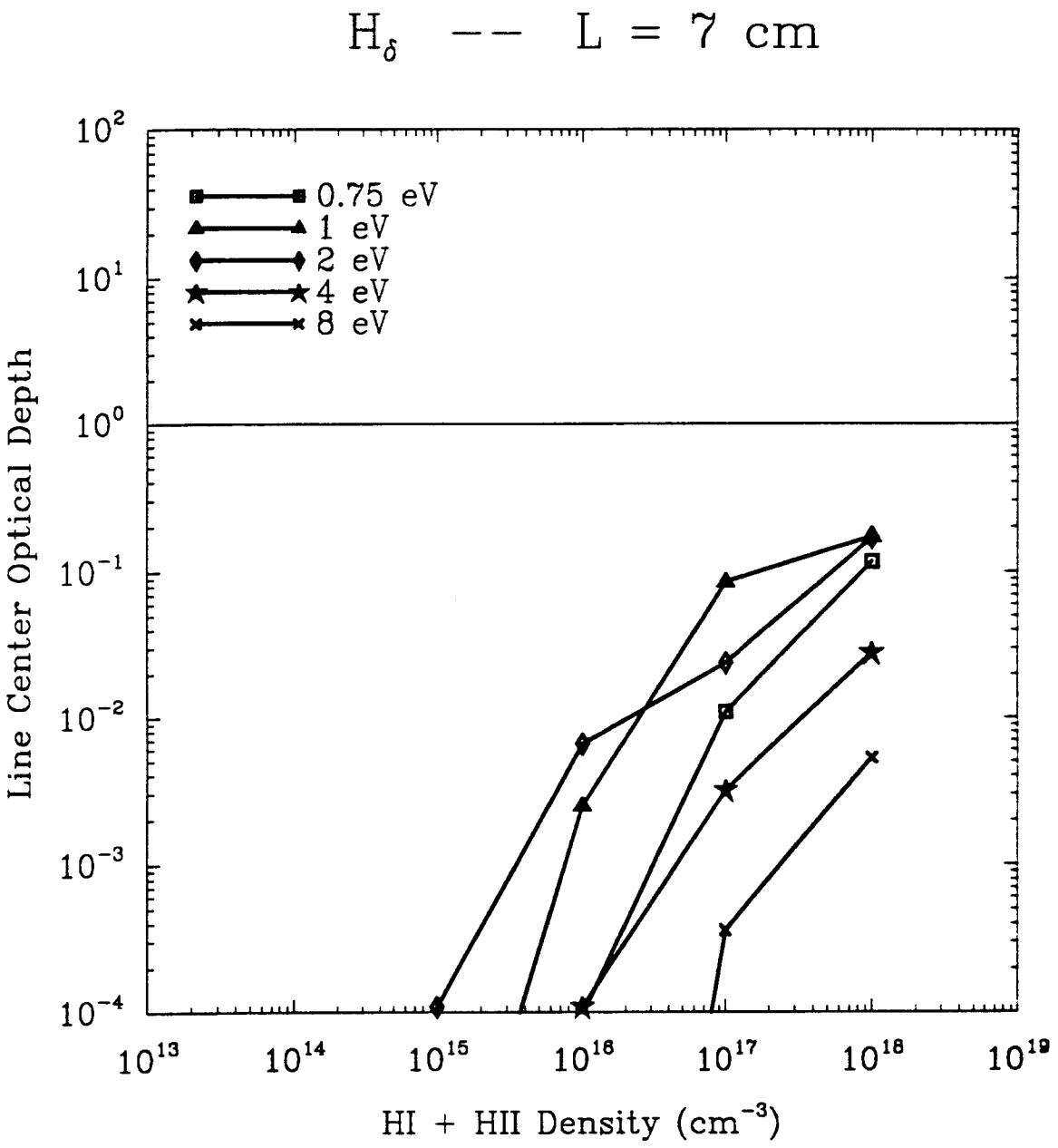

Figure 5.5. H_δ line center optical depth as a function of hydrogen number density. The optical depths correspond to a line-of-sight distance of 7 cm. The horizontal line corresponds to an optical depth of 1.

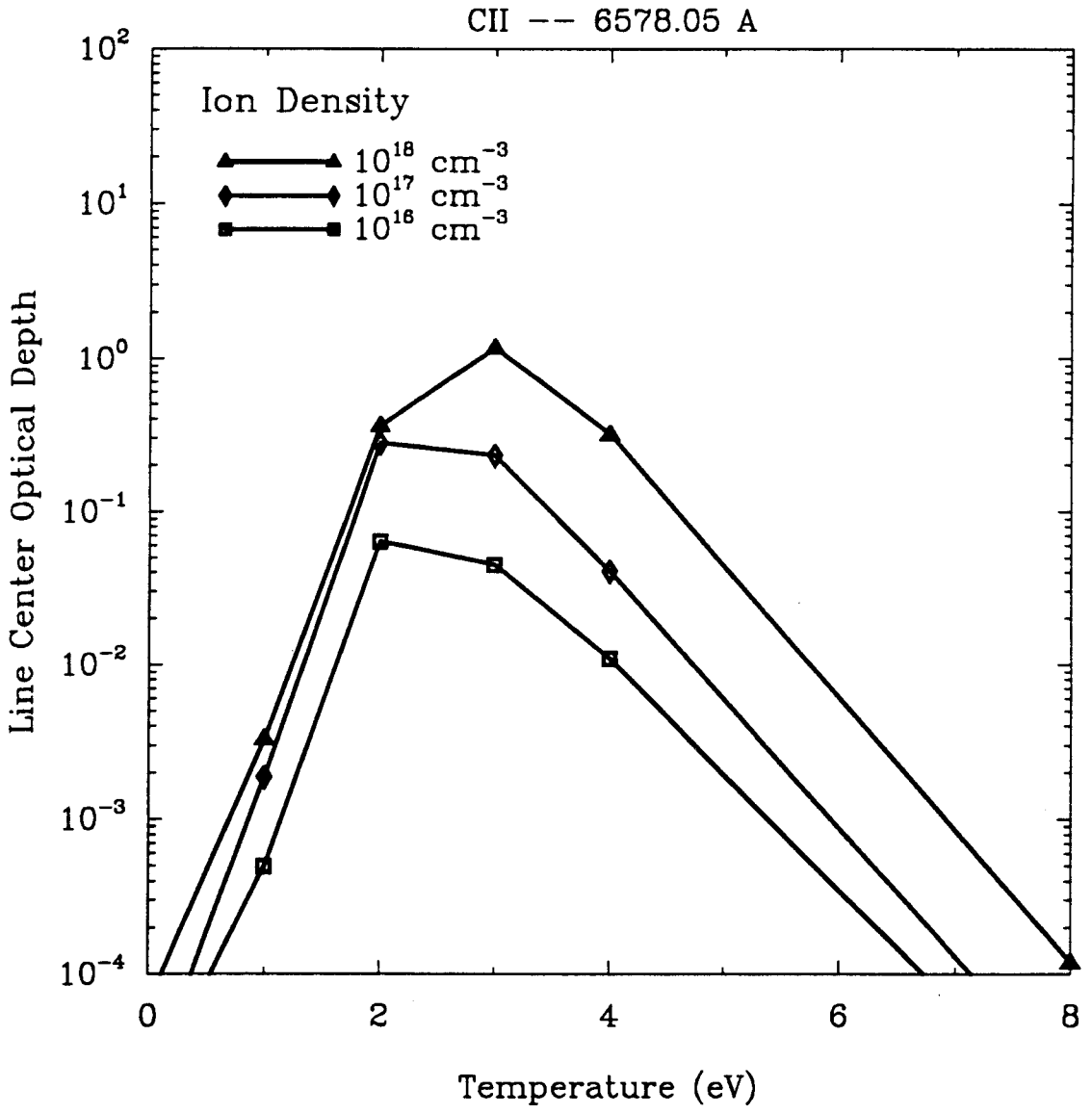

Figure 5.6. Line center optical depth of C II line at $\lambda = 6578.05$ Å as a function of temperature and carbon number density. The optical depths correspond to a line-of-sight distance of 7 cm.

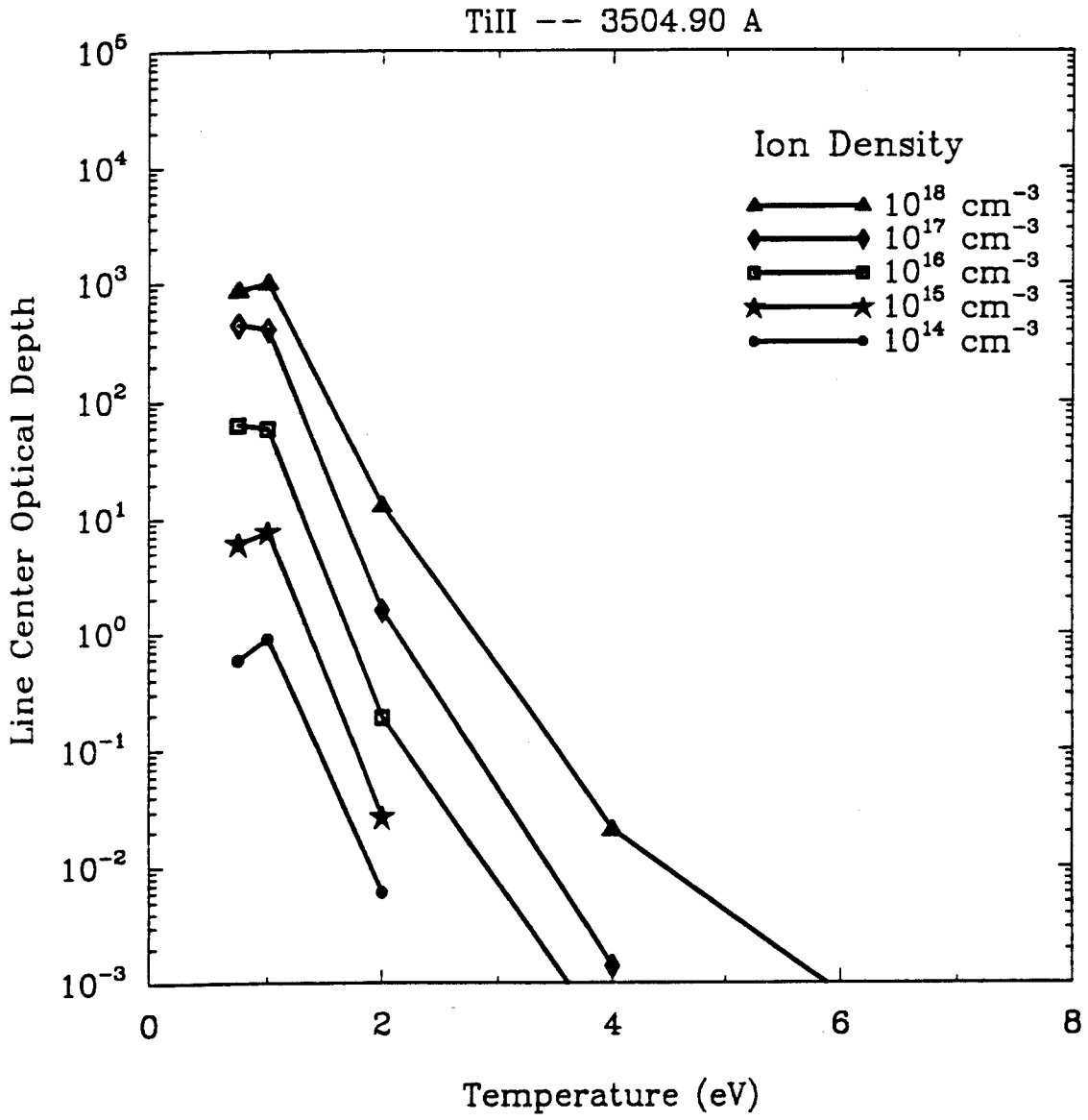

Figure 5.7. Line center optical depth of Ti II line at $\lambda = 3504.90$ Å as a function of temperature and carbon number density. The optical depths correspond to a line-of-sight distance of 7 cm.

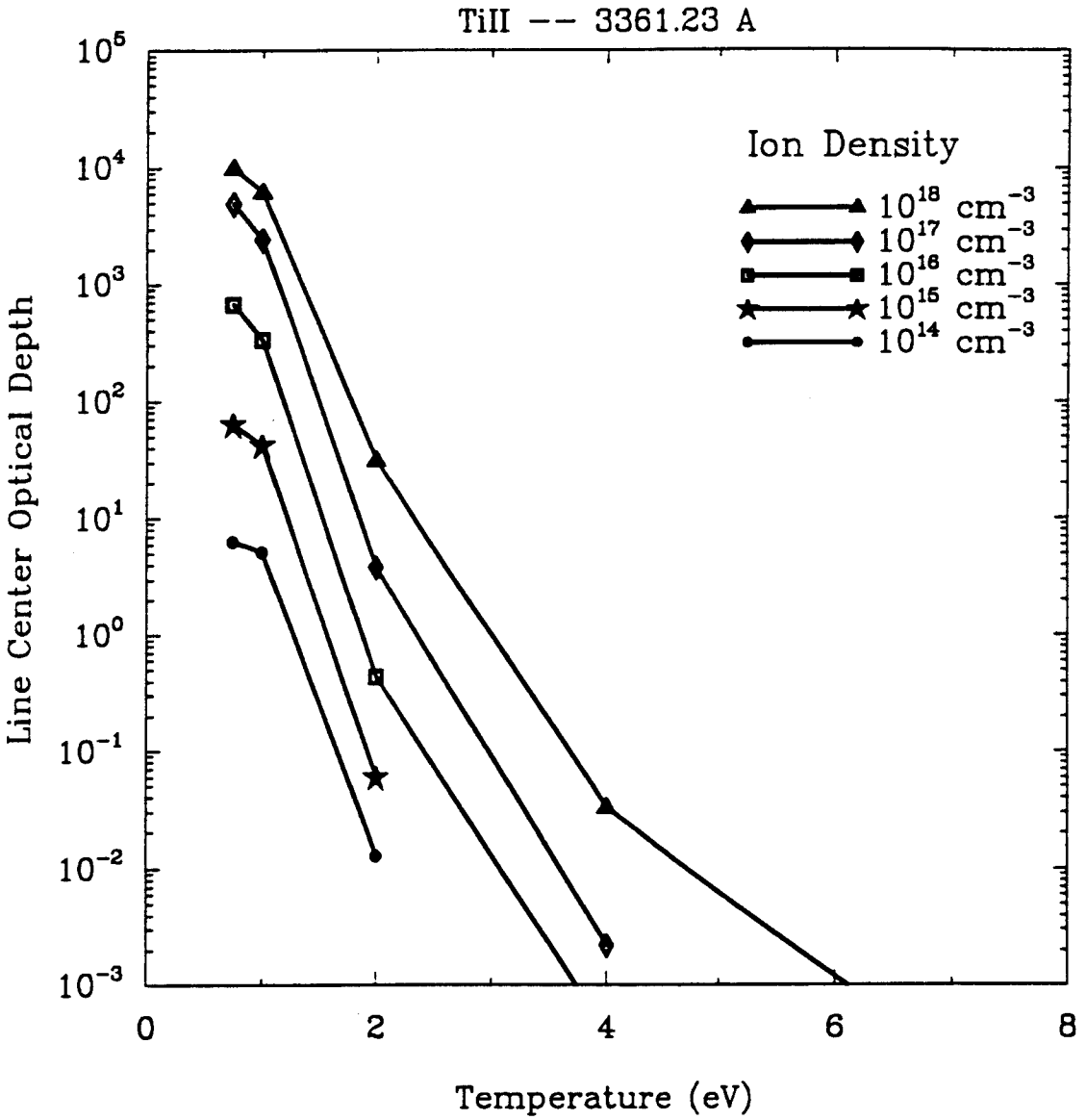

Figure 5.8. Line center optical depth of Ti II line at λ = 3361.23 Å as a function of temperature and carbon number density. The optical depths correspond to a line-of-sight distance of 7 cm.

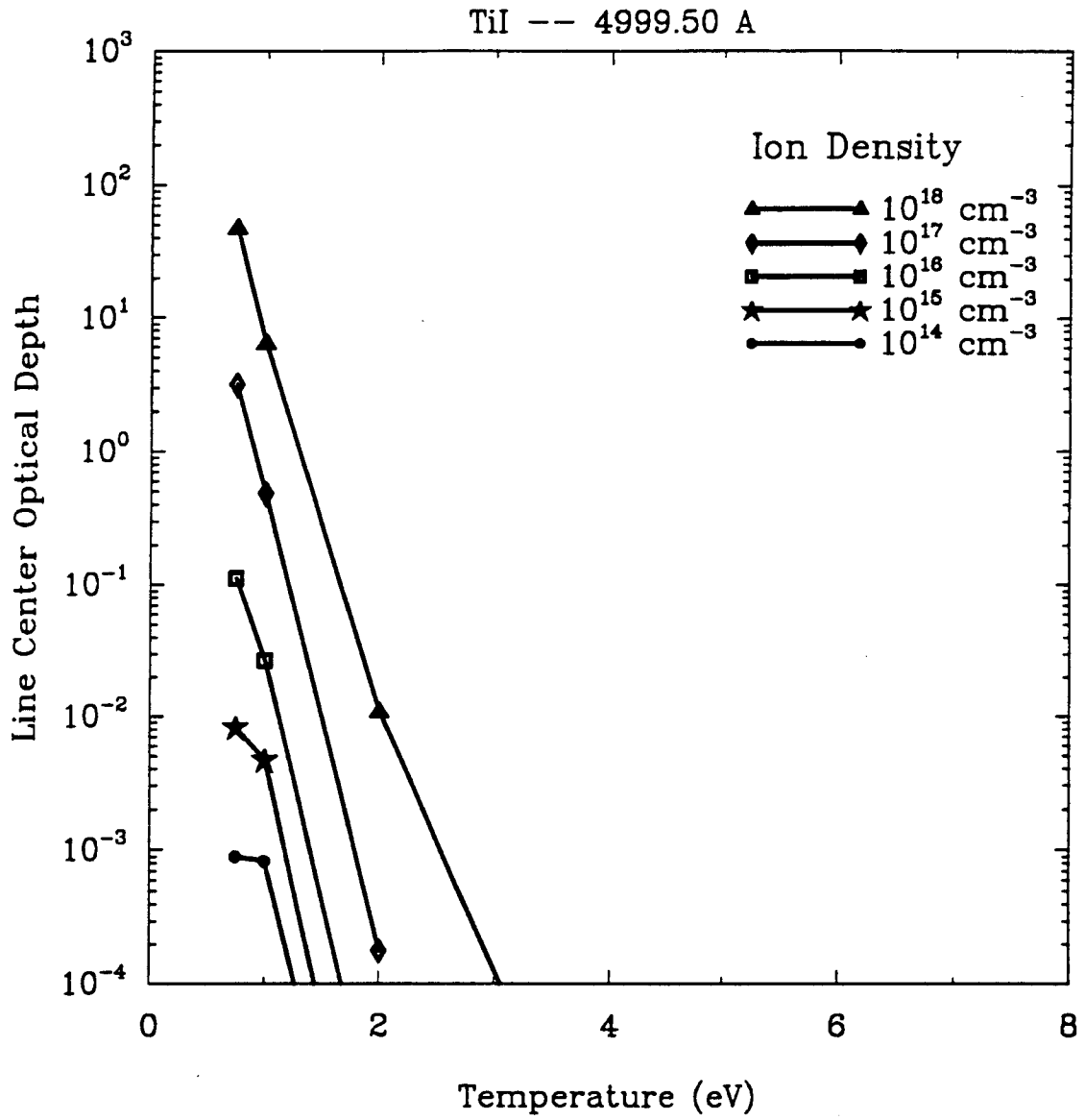

Figure 5.9. Line center optical depth of Ti I line at λ = 4999.50 Å as a function of temperature and carbon number density. The optical depths correspond to a line-of-sight distance of 7 cm.

3361.23 Å) the peak optical depth at $T = 0.75$ eV and $n = 10^{18}$ cm^{-3} is 10^4! However, at temperatures $\gtrsim 4$ eV all of the Ti I and Ti II lines become optically thin because of the shift to higher ionization stages.

6. A Hot Plasma Stopping Power Experiment with Diagnostics for Beam Energy and Target Temperature

In this section, we propose what we feel is an interesting target design for a KALIF experiment. We emphasize that this is as preliminary conceptual design. No calculations have yet been performed to make any quantitative predictions. The purpose of the experiment is to investigate proton beam energy deposition in a hot plasma. This would be accomplished by measuring the beam energy, stopping range, and plasma temperature as a function of time and penetration depth.

The basic design is illustrated in Fig. 6.1. A central feature of the design is a wedge-shaped stopping medium (shown as CH_2 in Fig. 6.1). A thin ($\Delta L \sim 1$ μm) Au layer could be placed at the front of the target to measure the incident beam energy via Rutherford scattering. A two-material diagnostic layer is placed at an angle ($\sim 45°$) to the incident beam and CH_2 boundary, with the range to the midpoint roughly equal to the stopping range in hot material. The diagnostic region consists of thin layers of Ag and Al (each with $\Delta L \sim 0.1 - 1\,\mu$m). The purpose of the Al is to provide a temperature diagnostic from spectroscopic measurements of the K_α satellite lines. The Ag is used to provide a measurement of the beam energy from PIN XRD measurements of the L/K band ratios. Ag is chosen in order to avoid contamination of the band intensities by opacity effects (see Sec. 4.3). Alternatively, a very thin layer of Au ($\Delta L \sim 10^2 - 10^3$ Å) could be used, in which case the M/L band ratio would be measured. Finally, some additional CH_2 would be placed behind the diagnostic layers as a tamper. This layer should be thin enough so that it does not attenuate the x-rays from the diagnostic layer excessively.

Because the diagnostic layer is at an angle to the stopping medium boundary the characteristics of the x-ray emission from the diagnostic layer will exhibit a spatial

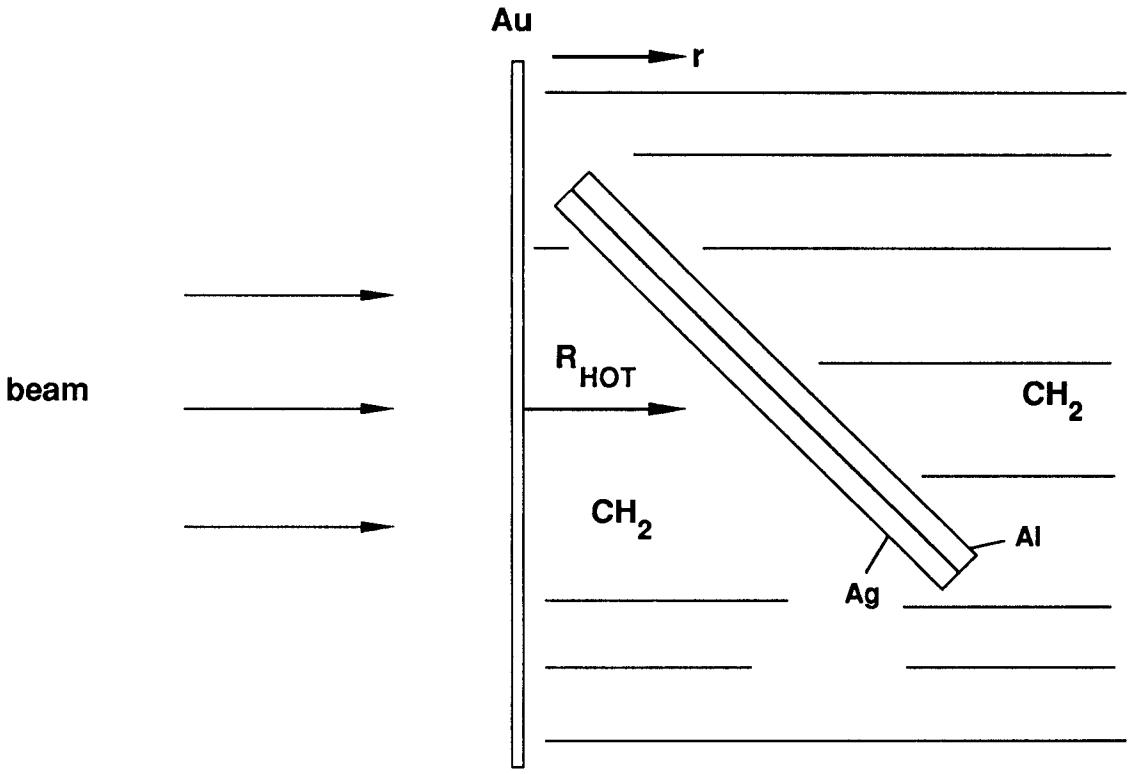

Figure 6.1. Schematic illustration of target proposed for a KALIF beam/plasma interaction experiment. Note the range a proton must penetrate to the diagnostic layer varies in the vertical direction.

dependence as well as time dependence. At early times, the material is cold and the stopping range is relatively high. In this case, the entire Ag layer might emit x-rays. The L/K band ratios should exhibit a spatial dependence because the protons travel through different amounts of the stopping medium. (See Figs. 3.11–3.13 for insights on the evolution of target and beam stopping properties.) At later times, the stopping range decreases as the material becomes hotter. The range is eventually reduced until only a portion of the diagnostic layers are struck by the beam. At this time, x-rays will only be emitted from the beam-irradiated portion. Thus, even if it were possible to measure only a time- and space-dependent x-ray signal (with no spectral information), significant information on the stopping physics could be gained. Additional constraints come from the Al K_α diagnostic for the temperature, the Ag band ratio diagnostic for the beam energy within the target, and the Au Rutherford diagnostic for the incident beam energy. (Space- and time-resolved measurements of the Al K_α lines could be obtained using a spectrometer similar to that to be used in upcoming PBFA-II experiments at Sandia.)

We again emphasize that this analysis is very preliminary. The purpose in describing it here is to illustrate the *concept.* It is entirely possible that other combinations of target and diagnostic materials will be more suitable for KALIF experiments.

7. Status of KATACO/NLTERT Coupling

7.1. Implementation of KATACO onto a DEC 5000/200 Workstation

In this section we briefly describe our ongoing efforts to implement the KATACO hydrodynamics code onto a workstation. The motivation for the implementation of KATACO onto a workstation is to facilitate the future coupling of the non-LTE radiative transfer code NLTERT with the KATACO code. The coupling of the NLTERT code into KATACO will enhance the hydrodynamic and radiative transfer simulation capabilities of KATACO. This will enable KATACO to be used as a diagnostics tool in support of future KALIF beam-plasma experiments by providing improved spectral surface emission distributions. The temperatures and densities within the plasma region can be deduced from a comparison of the simulated and experimentally measured spectral distributions.

Initial work on the implementation of KATACO onto the DEC 5000/200 workstation was begun in August. The code package received contained the source code, two test problems and an information file containing information regarding replacement of the IMSL Error Function and Exponential Integral routines. The version of the KATACO code provided for the implementation was a single precision, IBM version of the code. The Error Function routine was obtained from Numerical Recipes (Press et al. 1986) and the Exponential Integral routine from NETLIB. After implementation of these routines a single precision version of KATACO was compiled. An attempt was made to execute test problems 1 and 2. Test problem 1 did not execute to completion and test problem 2 never proceeded beyond the initialization phase. We then compiled KATACO in double precision to avoid roundoff error as the DEC 5000/200 workstation is a 32 bit machine. A brief list of variables, routines, and declaration changes which are considered the standard modifications are given below;

a) single precision declaration changes such as real*4 must be changed to real*8 or implicit double precision declaration must be used;

b) implicitly typed real number variables such as 2.0, 0.0, etc. must be appended with d0 (i.e. 2.0 $\rightarrow$ 2.0d0).

c) single precision intrinsic routines ALOG, AMAX, AMIN, FLOAT, etc. must be changed to their double precision counterparts.

Another problem encountered was common block misalignments in double precision. The current DEC RISC and Sun Fortran compilers are quite sensitive to the ordering of real and integer variables in common blocks. The compilers prefer having all real variables listed first followed by integer variables. Hence mixed argument lists where integer variables are mixed among real variables will cause misalignment. In this sense the current RISC compilers are not very forgiving. Since mixed argument lists are used throughout the KATACO code, the subject of using the "include" statement to simplify the modifications and to replace repeated usage of various common blocks in multiple subroutines was discussed. It was decided that the "include" statement should be used to insert the appropriate common block(s) into their respective subroutines. Other problems encountered during compilation were conflicting integer and double precision variable declarations in subroutine argument lists. These problems were discussed with Herr Küfner via email.

At the September 23-24, 1991 review meeting at KFK several of the problems encountered with the conversion to double precision were discussed. During the discussion it was bought to our attention that the KATACO version sent to us for implementation was an old version of KATACO and that a newer, updated version of the code should be made available for implementation onto our workstation. This version should preferably

be a double precision version. A double precision version of KATACO was forwarded to our group by Herr Küfner. This version of KATACO was provided to KfK by Herr R. Rusch from EPFL, Lausanne. Output listings for the previous two test problems were forwarded to our group at a later date. This version of KATACO was compiled using a new version of the DEC Fortran RISC compiler. Compilation of the code proceeded without major problems. The compiler merely printed a warning about common block misalignments and gave a few errors regarding Herr Rusch's modifications for namelist input in subroutine DATA. It was also noted that no use had been made of the "include" statement to simplify the insertions of common blocks into subroutines. Implementation of the "include" statement will be made when the code is modified to eliminate the misalignment warnings. These modifications are currently ongoing.

7.2. Outline for Coupling NLTERT with KATACO

The plasma energy equation for each spatial zone can be written as:

$$De/Dt = -D(u^2/2)/Dt + \rho^{-1}\nabla \cdot (pu) - J + A + S \tag{7.1}$$

where e is the plasma specific internal energy, u is the fluid velocity, p is the pressure, ρ is the density, A and J are the radiation absorption and emission terms, and S is a source term (e.g., ion beam energy deposition). Thus, the internal energy at time t_{n+1} is given by:

$$e(t_{n+1}) = e(t_n) + (t_{n+1} - t_n)De/Dt\,. \tag{7.2}$$

The various contributions to De/Dt are evaluated using the plasma conditions at t_n. This form of time stepping is first order accurate in time. This approach has been applied successfully by others in a wide variety of studies (Clark and Apruzese, 1991).

Given the plasma internal energy at time t_n, one computes the atomic level populations, temperatures, and electron densities for each zone using the non-LTE radiative

transfer/CRE model. Two iteration loops are used: (1) an inner loop in which, for a given temperature distribution, the atomic levels are solved self-consistently with the radiation field; and (2) an outer loop in which the temperature distribution is found using the internal energy constraint.

Once $T(r), n_e(r)$, and the atomic level populations are known, the radiation emission and absorption rates are easily computed from the zone-to-zone coupling coefficients, Q^{ea}. The emission rate in zone d due to all bound-bound transitions can be written as:

$$J_d = \sum_{u>\ell} \Delta E_{u\ell}\, A_{u\ell}\, n_u^d \tag{7.3}$$

where $A_{u\ell}$ is the spontaneous emissison rate for the transition $u \rightarrow \ell$, $\Delta E_{u\ell}$ is the transition energy, and n_u^d is the number density of atoms in the upper state of the transition in zone d. To determine the absorption rate for zone d, we add the contribution of photons emitted in each zone:

$$A^d = (\Delta V^d)^{-1} \sum_{u>\ell} \Delta E_{u\ell}\, A_{u\ell} \sum_e n_u^e\, \Delta V^e\, Q^{ed} \tag{7.4}$$

where ΔV^d is the volume of zone d.

One can also easily compute the radiant energy flux escaping at the plasma boundary at each time step by subtracting the absorption rate for all zones from the emission rate summed over zones:

$$F_{surface} = (Area)^{-1} \sum_{u>\ell} \Delta E_{u\ell}\, A_{u\ell} \sum_e n_u^e\, \Delta V^e\, (1 - \sum_a Q^{ea})\,. \tag{7.5}$$

The bound-free contribution to J^d, A^d, and $F_{surface}$ are similar to Eqs. (7.3) to (7.5), but with $A_{u\ell}$ replaced by $n_e\, \alpha_{rr}$ (the electron density times the radiative recombination rate coefficient).

The free-free (Bremsstrahlung) contribution should be computed using a multigroup radiation diffusion model, such as that developed by W. Hobel at KfK. Multigroup

opacities can be computed directly by the non-LTE code. The computational time required for this is likely to be small compared to the bound-bound calculations. In this case, no multigroup opacity tables need to be set up prior to the radiation-hydrodynamics runs.

8. Summary

During the past year, we have made significant improvements to our non-LTE radiation transport model and performed several sets of calculations in support of KALIF experiments. In regards to model improvements, we have developed a multiangle, multifrequency radiative transfer (MFRT) model and installed it in the same CRE code which contains the escape probability radiative transfer (EPRT) model. This gives the user the option of choosing transport models. The advantage of the multifrequency model is its superior accuracy, while the escape probability model has the advantage of requiring less computer time.

We performed a series of benchmark calculations in which both multifrequency and escape probability results were compared with previously published results. In addition, a kernel model was developed to test the accuracy of the angle-averaging approximation in the EPRT model. It was found that the main source of error in the EPRT model results not from the angle-averaging method, but from the coarseness of the spatial zoning. This problem is much less significant in the MFRT model because it solves the transfer equation with a higher order of accuracy. In 2-level atom calculations for plasmas with either a spatial gradient in the line width or with a background continuum, we find that large errors can occur (up to an order of magnitude in the level populations) due to the frequency-averaging method in the EPRT model. We have also assessed the influence of these effects in multilevel atom calculations for typical laboratory plasma conditions.

The self-consistent solution of the atomic rate equations and the radiation field is a critical feature of our non-LTE radiation transport model. The atomic level populations are obtained by an iterative method in which the statistical equilibrium and radiative transfer equations are solved alternately. In the past year we have implemented a technique recently developed by astrophysicists which can significantly reduce the computa-

tional time and core memory requirements for a problem. In this approach the statistical equilibrium equations are solved independently for each spatial zone instead of using the complete zone-to-zone coupling approach of Apruzese. Instead of solving a single matrix of size $(N_L N_D) \times (N_L N_D)$, one solves N_D matrices of size $N_L \times N_L$ (N_L = number of atomic levels; N_D = number of spatial zones). Details of this work have been reported elsewhere (MacFarlane 1992).

Three series of calculations were performed to support present and future experiments at KfK. First, we continued our investigation of using K_α line radiation as a temperature diagnostic for Al targets. Using the results from KATACO hydrodynamic simulations we computed time-dependent and time-integrated K_α spectra for expanding Al plasmas. Among other things, we find a significant difference in the K_α spectra emitted from the front (beam-irradiated) side and the rear side of the target. When the beam is stopped midway through the target, the rear section of the plasma cannot emit K_α radiation because no high energy protons are available to create K-shell vacancies in the target. However, because that part of the plasma can be hot, it can *absorb* K_α radiation emitted from the beam-irradiated side. Also, we have obtained good agreement with the PBFA-II K_α spectrum reported by Bailey et al. (1990). We now understand the reason for the relatively large flux from the Al I–Al IV lines, and have shown that the excited states of an ion can produce lines at wavelengths near those of the next higher ionization stage. Benchmarking our results with experimental data of course allows us to improve and gain confidence in our theoretical models, as well as provides insights that can be used to plan future experiments.

Beam-induced, inner-shell x-ray lines can also be used to diagnose beam conditions. To study this, we have investigated the characteristics of K-, L-, and M-shell line radiation from Au foils. Since Au is a high-Z material, it was necessary for us to acquire

the capability to perform multiconfiguration Dirac-Fock calculations. X-ray production cross sections, line ratios, and band ratios were computed to predict their dependence on beam energy. We find this method holds promise for providing an independent check on the beam energy. However, some complications arise for micron-sized gold foils when they are heated to temperatures above roughly 15 – 20 eV because resonant self-absorption becomes important. To avoid such opacity problems one could examine possibilities for using thinner foils, different (lower-Z) materials, or spectrometers.

To provide theoretical support for analyzing diode plasma spectra, we performed CRE calculations to estimate the optical depths of H, Ti, and C lines. We find that the selected Ti I and Ti II lines tend to have relatively large optical depths because they involve transitions between low-lying energy levels. The hydrogen Balmer lines were found to be optically thick for the higher range of densities investigated, while the selected C II lines were generally optically thin over the entire range of plasma conditions studied.

Finally, we have begun the task of coupling the non-LTE radiative transfer code with MEDUSA/KATACO. This work is presently in a preliminary phase and will continue during the next year.

Acknowledgements

The authors gratefully acknowledge support from Kernforschungszentrum Karlsruhe through Fusion Power Associates. We also thank Balbir Goel for kindly providing hydrodynamics results for Al targets.

References

Abramowitz, M., and Stegun, I.A., Handbook of Mathematical Functions, Dover, New York (1972).

Apruzese, J.P., *J.Q.S.R.T.* **34**, 447 (1981).

Apruzese, J.P., Davis, J., Duston, D., and Whitney, K.G., *J.Q.S.R.T.* **23**, 479 (1980).

Athay, G., Radiation Transport in Spectral Lines (Reidel, Dordrecht, 1972).

Avrett, E.H., and Hummer, D.G., *Mon. Not. R. Astr. Soc.* **130**, 295 (1965).

Bailey, J., Carlson, A.L., Chandler, G., Derzon, M.S., Dukart, R.J., Hummel, B.A., Johnson, D.J., Lockner, T.R., Maenchen, J., McGuire, E.J., Melhorn, T.A., Nelson, W.E., Ruggles, L.E., Stygar, W.A., and Wenger, D.F., *Lasers and Particle Beams* **8**, 555 (1990).

Clark, R.W., and Apruzese, J.P., personal communication (1991).

Cowan, R.D., Theory of Atomic Structure and Spectra, Univ. of California Press, Berkeley, 1981.

Datz, S., et al., *Phys. Rev. A* **9**, 192 (1974).

Derzon, M.S., et al., in preparation, 1992.

Fischer, C.F., *Comput. Phys. Commun.* **14**, 145 (1978).

Grant, I.P., McKenzie, B.J., Norrington, P.H., Mayers, P.H., and Pyper, N.C., *Comput. Phys. Commun.* **21**, 207 (1980).

Herzberg, G., Atomic Spectra and Atomic Structure, Dover, New York (1944).

Hummer, D.G., *Mon. Not. R. Astr. Soc.* **138**, 73 (1968).

Hummer, D.G., and Mihalas, D., *Astrophys. J.* **331**, 794 (1988).

Kahn, J.M., Potter, D.L., and Worley, R.D., *Phys. Rev. A* **13**, 1735 (1965).

Kunasz, P.B., and Hummer, D.G., *Mon. Not. R. Astr. Soc.* **166**, 19 (1974).

MacFarlane, J.J., Wang, P., and Moses, G.A., A Model for Computing Radiation Transport in Moderate Density Plasmas, Report FPA-90-1, Fusion Power Associates, Madison, WI (1990).

MacFarlane, J.J., Wang, P., and Henderson, D.L., Numerical Simulation of Non-LTE Radiative Transfer and Atomic Physics Effects in Plasmas Created by Intense Proton Beams, Report FPA-91-1, Fusion Power Associates, Madison, WI (1991).

MacFarlane, J.J., *Astron. Astrophys.*, in press (1992).

McKenzie, B.J., Grant, I.P., and Norrington, P.H., *Comput. Phys. Commun.* **21**, 233 (1980).

Mehta, R., et al., *Phys. Rev. A* **26**, 1883 (1982).

Mihalas, D., Stellar Atmospheres, Second Edition, Freeman, New York (1978).

Mihalas, D., Kunasz, P.B., and Hummer, D.G., *Astrophys. J.* **202**, 465 (1975).

Mihalas, D., Hummer, D.G., Mihalas, B.W., and Dappen, W., *Astrophys. J.* **350**, 300 (1990).

Moore, C.E., "Selected Tables of Atomic Spectra," National Bureau of Standards, U.S. Dept. of Commerce, Washington, D.C. (1965).

Paul, H., and Muhr, J., *Phys. Rep.* **135**, 47 (1986).

Press, W.H., Flannery, B.P., Teukolsky, S.A., and Vetterling, W.T., Numerical Recipes, Cambridge University Press, Cambridge (1986).

Rutledge, C.H., and Watson, R.L., *Atomic Data Nucl. Data Tables* **12**, 195 (1973).

Rybicki, G.B., and Hummer, D.G., *Astron. Astrophys.* **245**, 171 (1991).

Scofield, J.H., *Phys. Rev.* **179**, 9 (1969).

Sera, K., et al., *Phys. Rev. A* **22**, 2536 (1980).

Weise, W.L., and Musgrove, A., "Spectroscopic Data for Titanium, Chromium, and Nickel," Oak Ridge National Laboratory Report ORNL-6551/V1 (1989).